

Power System Current Measurement Using Sensor Array
Techniques

by

Pengfei Gao

A thesis submitted in partial fulfillment of the requirements for the degree of

Doctor of Philosophy

in

Power Engineering and Power Electronics

Department of Electrical & Computer Engineering
University of Alberta

© Pengfei Gao, 2018

Abstract

Measuring current flow is an essential task for power systems. Although offering high-quality measurement results, traditional current sensing techniques share a common problem: the need for direct access to each individual conductor. The lack of an effective approach for measuring the currents in a group of bundled, enclosed or inaccessible conductors has resulted in the needs for new current measurement techniques.

This thesis proposes methods to address three multi-conductor current measurement problems utilizing the sensor-array-based techniques. The first technique, including two main components, is designed specifically for measuring the currents entering the North America homes. One component is a sensor array deployed near the conductors of interest to measure the magnetic fields produced by the currents. The other component is a sensor calibrator, connecting to the conductors at a location downstream the sensor array. The relationship between the sensor outputs and the conductor currents is derived by an active calibration scheme, making it feasible to determine the currents through the sensor measurements non-intrusively.

For the inaccessible conductors that are difficult to apply the active calibration scheme, this thesis proposes to use a magnetic sensor array to solve the conductor positions and their currents mathematically. The sensor parameters are made

known to the measurement system model through an off-line calibration method. A prototype device has been developed to measure different types of industrial cables.

Measuring the Zero-sequence current of overhead power conductors has been a challenging problem but is important to many power quality studies. This thesis presents a technique that can measure the overhead line zero-sequence current remotely, regardless the existence of the neutral conductor. The proposed technique is adaptive to different overhead line configurations and does not require any input of the line parameters. The promising results from actual field tests indicate that the proposed zero-sequence current sensor array has a potential to become a powerful tool for the electric power industry.

Preface

This thesis is an original work by Pengfei Gao. Chapter 2-4 of this thesis have been published as scholarly articles, in which Prof. Wilsun Xu is the supervisory author and has contributed to technical deviations and manuscript composition, Prof. Shunfu Lin is the co-author and has contributed to the discussion of the prototype fabrication, Dr. Lichan Meng is the co-author and has contributed to the manuscript composition, Dr. Moosa M. Haji is the co-author and has assisted in the mathematical simulations.

Part of Chapter 2 of this thesis has been published as

- P. Gao, S. Lin and W. Xu, “A Novel Current Sensor for Home Energy Use Monitoring,” *IEEE Trans. Smart Grid*, vol.5, no.4, pp.2021-2028, July 2014

Part of Chapter 3 of this thesis has been published as

- L. Meng, P. Gao, M. M. Haji and W. Xu, “Magnetic Sensor Arrays-based AC Current Measurement for Multi-Conductor Cables using Evolutionary Computation Method”, *IEEE Trans. Instrum. Meas.*, vol.64, no. 10, pp. 2747-2758, Oct. 2015

Part of Chapter 4 of this thesis has been published as

- S. Lin, P. Gao and W. Xu, “Zero sequence power line current measurement by using magnetic field sensor array,” *Int. Trans. Electr. Energ. Syst.*, Vol.25, Issue 9, pp. 1685–1696, Sept. 2015

Acknowledgements

I would like to extend my sincere appreciation to many people, who are so generous to me all the way along my Ph. D. studies. It would not have been possible to complete this thesis without the support and guidance that I received from my supervisor, my committee members, my colleagues, my friends and my family.

I would like firstly to express my gratitude to my supervisor, Professor Wilsun Xu, for all the effort, and support he gave me these years. I began my study like a toddler hobbling ahead, without Dr. Xu's patience and encouragement, there is no chance for me to grow and become a researcher who is able to think independently.

My special thanks go to Dr. Jing Yong from Chongqing University, China and Dr. Walmir Freitas from University of Campinas, Brazil. Their insightful comments and invaluable inspirations are highly appreciated. My academic collaborators, Dr. Shunfu Lin, Dr. Yi Dong, Dr. Lichan Meng, Dr. Ahda P. Grilo and Dr. Kun-Long Chen are also appreciated for their discussions and suggestions on the results we have developed. It was my great honor to work with these talented and enthusiastic researchers all over the world.

I feel lucky to work with my colleagues in the PDS-LAB, for allowing me to conduct my research in a warm and enjoyable environment. I would never forget the days we cheered up each other and fought for our goals, the help from Dr. Xun Long, Dr. Alex Nassif, Dr. Yunfei Wang, Dr. Ming Dong, Dr. Yanbo Xue, Moosa Moghimi Haji, Yu Zhao, and Xin Li are appreciated.

I acknowledge the financial support received towards my research from the

Natural Sciences and Engineering Research Council of Canada, the Alberta Technology Innovates, and the NSERC Smart Microgrid Network.

I would like also to acknowledge ATCO Electric and FortisAlberta Inc., for providing the experiment validation opportunity for this research.

As the only child in my family, I owe my parents so much. I always feel confident and fearless since I know they trust me, understand me and always stand behind of me. Words cannot express how grateful I am to my parents for all of the sacrifices they have ever made. Their best wishes to me are what sustained me to the present.

I dedicate this thesis to my beloved wife, Yu Zhou, who planned to pursue advanced education abroad with me, came to Canada together with me, and has been by my side throughout my program. Undertaking this Ph. D. is truly a life-changing experience to me, I would not have had the courage to embark on this journey and step forward this far without her.

Table of Contents

Chapter 1 Introduction	1
1.1 Overview of Existing Current Measurement Techniques	1
1.1.1 Current-Sensing Techniques for Single Conductors	2
1.1.2 Sensor Array Techniques for Multiple Conductors.....	6
1.2 Challenges of Multi-Conductor Current Measurement	10
1.3 Thesis Scope and Outline.....	13
Chapter 2 Multi-Conductor Current Measurement Using Active Calibration Method	15
2.1 Introduction.....	16
2.2 Problem Formulation and the Proposed Scheme	19
2.3 Sensor Array Calibration.....	24
2.3.1 Calibration Pattern Generation.....	25
2.3.2 Characteristics of Calibration Current	28
2.3.3 Calibration Pattern Extraction.....	31
2.4 Application for Residential Home Current Monitoring.....	33
2.4.1 Simplified Two-phase Calibration	35
2.4.2 The Calibrator Prototype.....	40
2.4.3 The Sensor Array Prototype	41
2.5 Lab and Field Test Validations	42
2.5.1 Lab Test Results	43
2.5.2 Filed Test Results in Real Homes	44
2.6 Summary	47
Chapter 3 Multi-Conductor Current Measurement with Known Sensor Parameters	49

3.1	Introduction.....	50
3.2	Problem Formulation	51
3.2.1	Modeling of Single-Conductor and Single-Sensor System	52
3.2.2	Modeling of Three-Conductor and Sensor Array System.....	56
3.3	Proposed Current Measurement Scheme	59
3.3.1	Determining the Sensor Parameters.....	59
3.3.2	Determining the Conductor Positions.....	67
3.3.3	Real-time Conductor Current Measurement.....	71
3.4	Experiment Validations and Discussions	72
3.4.1	Experiment Bench Setup.....	72
3.4.2	Sensor Array Calibration Results.....	74
3.4.3	Conductor Position Computation Results.....	75
3.4.4	Conductor Current Measurement Results.....	77
3.5	Summary.....	82
Chapter 4 Zero-Sequence Current Measurement for Overhead Power Lines		83
4.1	Introduction.....	84
4.2	Review of ZSC Measurement Techniques.....	85
4.3	Problem Formulation	89
4.3.1	Proposed Scheme for Three-Phase-Three-Wire System.....	94
4.3.2	Proposed Scheme for Three-Phase-Four-Wire System.....	99
4.4	Simulation Verifications.....	103
4.5	Challenges of Implementation and the Prototype Device.....	106
4.5.1	Practical Challenges of Implementation	107
4.5.2	Prototype Measurement System.....	109
4.6	Lab and Field Test Validations.....	114
4.6.1	Lab Experiment Setup and Results.....	114
4.6.2	Field Test Description and Results.....	119
4.7	Summary.....	126
Chapter 5 Conclusions and Future Works.....		128

5.1	Thesis Conclusions	128
5.2	Recommendations for Future Work	129
	Bibliography	132
	Appendix.....	142

List of Tables

Table 2.1: Current measurement accuracy categorized in Ampere groups	47
Table 3.1: Sensor information obtained from computation	65
Table 4.1: Data recording equipment and its connection.....	87
Table 4.2: The parameters of one typical three-phase-four-wire overhead system	91

List of Figures

Figure 1.1: One example current transformer.	3
Figure 1.2: Basic configuration of a Rogowski coil.	3
Figure 1.3: MEMS piezoelectric AC current sensor	5
Figure 1.4: One example commercial fiber-optic-current-sensors	6
Figure 1.5: Enclosed conductor examples.	10
Figure 1.6: Non-split conductor examples.....	11
Figure 1.7: Sensor array system to estimate overhead distribution feeder currents.	12
Figure 2.1: Configuration of the magnetic sensor array for enclosed conductor current estimation.....	16
Figure 2.2: Proposed sensor array system for enclosed conductor current measurement.	20
Figure 2.3: The case of one conductor not perpendicular to the sensing plane. ...	22
Figure 2.4: The magnetic sensor array deployed around a conduit.	24
Figure 2.5: Magnetic sensor array with an automated calibrator.....	25
Figure 2.6: The system configuration of the sensor array with the calibrator.	26
Figure 2.7: Circuit analysis when calibration is performed on phase A-N.....	28
Figure 2.8: Thyristor voltage and current waveform for resistive connection.....	29
Figure 2.9: System voltage and conductor current during A-N calibration.	30
Figure 2.10: The three sensor outputs during one calibration.....	32
Figure 2.11: Extracted sensor outputs that are due to the calibration current.	33
Figure 2.12: Magnetic sensor array installed at residential homes.	34
Figure 2.13: Magnetic sensor-array-based current measurement technique.....	35
Figure 2.14: different socket types for phase A-B connection.....	36
Figure 2.15: Two-phase calibration scheme for the actual implementation.	37
Figure 2.16: Two-phase calibration in reference to the home electrical panel labels.	38

Figure 2.17: Flow chart of a complete calibration process.	40
Figure 2.18: The prototype of the sensor calibrator.	41
Figure 2.19: Circuit diagram of the magnetic sensor array.	42
Figure 2.20: Lab experimental bench with sensor array installed.	43
Figure 2.21: Lab experiment results showing fundamental component performance.	44
Figure 2.22: Lab experiment results showing third order harmonic performance.	44
Figure 2.23: Field test installations in two pilot residential houses.	45
Figure 2.24: One day of real life measurement in test house #1.	45
Figure 2.25: One day of real life measurement in test house #2.	46
Figure 2.26: The error band definition.	47
Figure 3.1: Modeling of the one sensor and single conductor configuration.	53
Figure 3.2: Sensor array deployment.	61
Figure 3.3: Layout of magnetic sensor array in the experiments.	62
Figure 3.4: Conductors energizing sequence.	63
Figure 3.5: Sensor position difference from the computation and the reference. .	66
Figure 3.6: Flowchart for the conductor position computation algorithm.	69
Figure 3.7: Flowchart of the process how to compute the conductor positions. ..	70
Figure 3.8: Diagram of experimental bench setup.	73
Figure 3.9: Photograph of experimental bench setup.	73
Figure 3.10: Pictures of the sensor array system.	74
Figure 3.11: Sensor S_1 parameters calibration result evaluation.	75
Figure 3.12: Basic cable configurations.	76
Figure 3.13: Experimental result for the conductor position computation.	76
Figure 3.14: The measurement results for the three-phase balanced currents.	77
Figure 3.15: The measurement results for the three-phase unbalanced currents. .	78
Figure 3.16: Varied current magnitude waveform.	79
Figure 3.17: Error analysis for three phase current magnitudes.	80
Figure 3.18: Error analysis for three phase current phase angles.	81
Figure 4.1: Examples of the overhead power lines that the conductors are concentrated seeing at the ground level.	84

Figure 4.2: Current meter at the hot stick end for line current measurement.	88
Figure 4.3: Improved wireless hot stick current meter.....	89
Figure 4.4: A typical three-phase-four-wire overhead power line configuration..	91
Figure 4.5: Problem formulation using superposition theory.	93
Figure 4.6: Geometry of the three-wire power lines with two magnetic sensors.	94
Figure 4.7: Geometry of the four-wire power lines with four magnetic sensors for ZSC measurement.	99
Figure 4.8: The relationship between B_z , B_y and l_1 for balanced three-phase current.	104
Figure 4.9: The relationship between B_y , B_z and l_1 for unbalanced three-phase current.	104
Figure 4.10: Comparison result between the estimated and actual ZSC under different l_1	105
Figure 4.11: Comparison result between the estimated and actual ZSC under different d	105
Figure 4.12: Computation errors for the three-wire system for 50 random simulation cases.	106
Figure 4.13: Sensor deviations from the ideal positions.....	108
Figure 4.14: Measurement error caused by sensor deviation uncertainty.....	109
Figure 4.15: A possible design of the preferred sensor array.	110
Figure 4.16: A targeting structure to overcome the uncertainty 1.....	111
Figure 4.17: The sensor array aided by the gradiometer to mitigate uncertainty 2 and 3.....	111
Figure 4.18: The use of two-axis magnetic field sensor.	113
Figure 4.19: Photograph of the proposed sensor array prototype.	113
Figure 4.20: Schematic diagram and dimensions of the experiment set-up in lab.	114
Figure 4.21: Photograph of the test bed.	115
Figure 4.22: The signal flow chart of the proposed ZSC measurement system. .	116
Figure 4.23: Waveforms of the measured ZSC and the sensor signals.....	117
Figure 4.24: ZSC results comparison between the computation and ZSCT	

measurement.	118
Figure 4.25: First distribution system measurement set-up.	120
Figure 4.26: PQPro measurement for the first distribution line at the line regulator location.	121
Figure 4.27: First overhead line ZSC measurement by the propose sensor array.	122
Figure 4.28: Second overhead line ZSC measurement by propose sensor array.	122
Figure 4.29: Feeder current and ZSC computation results at the first location. .	123
Figure 4.30: Feeder current and ZSC computation results at the second location.	125

List of Abbreviations

AC	Alternating Current
ADC	Analog-to-Digital Convertor
CT	Current Transformer
DAQ	Digital Acquisition
DC	Direct Current
DE	Differential Evolution
DSP	Digital Signal Processing
EMF	Electrical Magnetic Field
FFT	Fast Fourier Transform
LPF	Low Pass Filter
MCU	Micro Control Unit
MGN	Multiple Grounded Neutral
PT	Potential Transformer
RMS	Root Mean Square
SCR	Silicon Controlled Rectifier
SWER	Single Wire Earth Return
PCB	Printed Circuit Board

Chapter 1

Introduction

The information regarding the current flow is important for modern power systems and many industrial, commercial, and residential practices. Measuring the power conductor current accurately and easily is always a challenging task in the electric power industry [1]-[3]. The fast growth of smart grid technology requires remarkable transforming of the electrical power grid [4], [5]. Accurate and reliable current-sensing techniques are more needed than ever to monitor the line conditions in real time in order to enable appropriate and predictable system margin optimization to provide more power capacity for the existing power system assets [6]. The increased current data will help the utilities to understand the in-depth load behaviors and their system operation characteristics, and also will improve their asset management and power quality regulations. The electrical engineers will be more confident about performing power system planning, expansion and alteration.

However, measuring the currents of a group of power conductors can be difficult. The existing current measurement techniques, as surveyed in Section 1.1, have difficulty solving multiple conductor current measurement problems when the conductors cannot be accessed individually. This thesis presents our continuous research to address the multiple conductor current measurement challenges in power systems. Three common challenges are explained in Section 1.2. The research objectives and the thesis outline are presented at the end of this chapter.

1.1 Overview of Existing Current Measurement Techniques

This section provides a review of the commonly adopted current measurement techniques in power systems. The state-of-the-art current-sensing techniques exploit a broad range of

developments from modern physics, material science and micro-fabrication techniques. Assorted current sensors have been developed to measure a single conductor's current, and the sensor array technology is being widely adopted to measure the currents in a group of conductors.

1.1.1 Current-Sensing Techniques for Single Conductors

Traditional current-sensing techniques for measuring a single power conductor's current can be summarized into the following categories.

- Current sensing with a shunt resistor

The use of shunt resistor is a popular method of high-current-sensing in power systems by utilizing Ohm's Law [7]. This method converts the problem to the measurement of the voltage across the shunt. It is easy to implement and capable of measuring both AC and DC current. Its intrusive nature requires pre-installation at the circuit-construction stage or interrupt the circuit to insert the shunt.

- Current sensing with a current transformer

The traditional instrumental current transformer (CT) is widely used in transmission systems and substations for the bus currents measurement [8]. There are two isolated windings named the primary winding and the secondary winding. A typical CT as shown in Figure 1.1 is made of one single turn primary, multiple turns secondary, and a magnetic core made with high-permeability material. When the CT's primary side connects to the high-current circuit, the induced current flowing through the secondary coil is stepped-down to a lower value proportional to the primary current. This method is also intrusive because the CT needs to be connected in the circuit during the system construction stage.

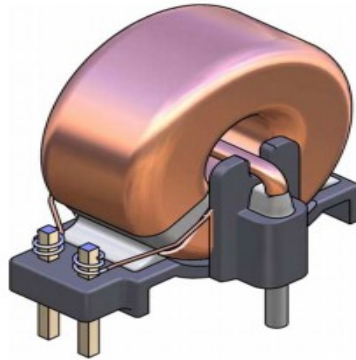


Figure 1.1: One example current transformer [1].

- Current sensing with a Rogowski coil

A Rogowski coil is designed based on the principle of Faraday's law of electromagnetic induction and is thus capable of measuring only AC current [9]. This current-sensing apparatus is basically considered as one kind of special current transformer in which the conductive wires are wound on a nonmagnetic core, leaving both wire terminals open for the output. The output voltage of this winding is linearly proportional to the time derivative of the current flow in the current passing through the core. Generally, an integrator circuit is attached at the end of the coil terminals to get an output voltage proportional to the primary current as shown in Figure 1.2.

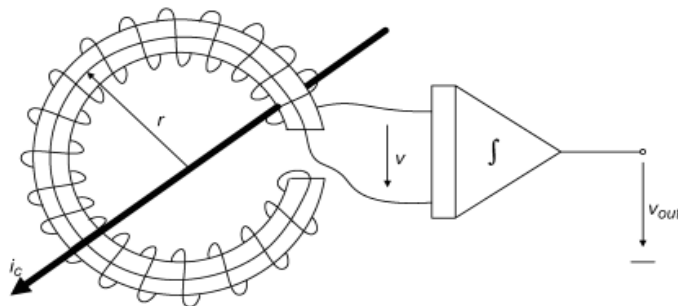


Figure 1.2: Basic configuration of a Rogowski coil [1].

The non-magnetic core makes the Rogowski coil a more attractive current-sensing technique than the CT method for many portable high current measurement applications because of the core saturation. It is a convenient and flexible way for invasive current

measurement. Current-sensing instrument utilizing this method is usually a clamp-on current probe wrapped around the conductor of interest.

- Current sensing with magnetic field measurement

Numerous research studies have explored the effectiveness of using the magnetic field transducers for power conductor current measurement in a contactless way. In addition to offering a significant saving on the equipment investment due to the reduced insulation requirement for the current transducers, the advantageous use of the magnetic field sensors also creates a non-intrusive, open-loop and linearly correlated measurement system, making the current measurement non-invasively without influencing the normal operation.

Many novel magnetic transducers with different material and fabrication processes are used to infer the power conductor current [10]-[13]. The pick-up coil sensor used for AC current measurement based on Faraday's law of induction magnetic field induction has been known for many years [14]. In this thesis, the coil sensor is preferred as the sensing element due to its operation and design simplicity, wide frequency bandwidth and large dynamics [15], [16]. Regardless of the type of the magnetic transducers, they measure the conductor current indirectly; i.e., they cannot infer the current without knowing the geometric information related to the sensing spot and the conductor position. A sensor calibration process is usually required beforehand to establish the relationship between the sensor output and the current.

Theoretically, the simplest way to measure the current is to place a single magnetic sensor near the current under measurement, but the crosstalk fields may limit the accuracy of a single magnetic sensor [17]. The magnetic fields generated by the currents under measurement must be distinguished from the external interference. A single sensor cannot distinguish the field generated by the current under measurement must be distinguished from other external fields. According to Ampere's Law, the current flowing in a conductor is proportional to the sum of the sensor outputs located around the conductor, so the second

step is to locate as many sensors as possible to calculate the current. Doing so enables another way to sense the current: placing a sensor array consisting high number of magnetic sensors near the current, processing the data from the magnetic sensor array, and then employing a proper algorithm to compute the current indirectly [18].

One example employing circular magnetic sensors to reduce the crosstalk effect according to Ampere’s Law is introduced in [19]. Ampere’s Law is achieved by the sensor array theoretically by deploying as many circular sensors as possible in [19]. Unavoidably, complex and computationally expensive algorithms like the spiral Fourier analysis and optimization are used to process the measurement data from the magnetic sensor array.

Other approaches have been introduced to avoid the long-time computer computation to ensure the measurement can be completed in a MCU level. K. Chen et al. developed an apparatus for measuring the conductor current by using four sensors symmetrically attached to the cable [20]. By averaging the sum of the outputs, the ambient magnetic field inferences were eliminated.

Moreover, the state-of-the-art Nano-fabrication technology enables a new research direction of fabricating the current sensor on a Micro-electromechanical system (MEMS). As discussed in [21], a piezoelectric cantilever is mounted on a permanent magnet at the free end. The magnetic field coupling caused by any nearby AC current can be detected through the forms of mechanical oscillations. This device features contactless measurement with self-power possibility. An open problem for this technique is the sensor calibration.

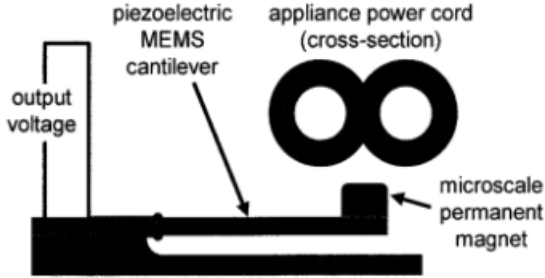


Figure 1.3: MEMS piezoelectric AC current sensor [21].

- Current sensing with optical current transducer

The piezoelectric optical fiber current sensor represents the state-of-the-art current-sensing technique. It is designed based on the Faraday Effect, where the linear polarized light wave propagates in proportion to the integral of the magnetic field at the sensor [22]. One commercial fiber-optic-current-sensor capable of measuring several hundred kA for DC current is manufactured by ABB Inc (as presented in Figure 1.4). Its excellent electrical isolation for both AC and DC allows high current measurement ability for even several hundred kilo-Amperes. An actual project utilizing the fiber optic current sensor to measure 500 kA DC at 0.1% accuracy has been completed [22].

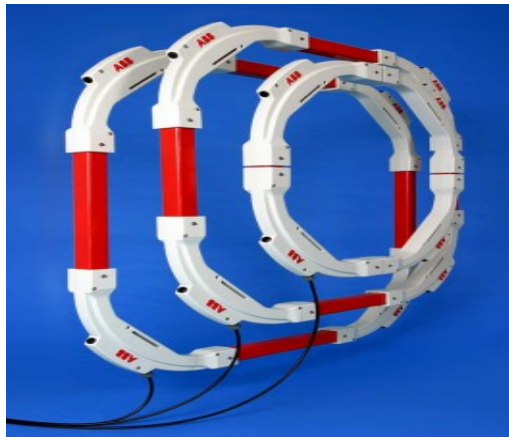


Figure 1.4: One example commercial fiber-optic-current-sensors [1].

1.1.2 Sensor Array Techniques for Multiple Conductors

Measuring the currents in a group of bundled or difficult-to-separate conductors is always a challenging problem. Although the existing current measurement techniques in Section 1.1.1 provide accurate single conductor current measurement results with good linearity, acceptable frequency response and simple implementation, they most of the time require individual access to every individual conductor. It is difficult to apply these techniques to measure multiple conductor currents directly; especially when these conductors are difficult or even impossible to split. However, the need for accessing an individual conductor in a conductor group in power systems are not uncommon: the power supply conductors for

residential houses, farms, camping sites, etc. are usually enclosed inside conduit housing, and many industrial power transfer cables are bundled together. Furthermore, when measuring the overhead distribution feeders, the common method is to install expensive clamp-on current probes rated with a high voltage operation grade. The installation requires either de-energizing the line or working in the hazardous vicinity. Even with such instruments, hooking up the conductors for long-time monitoring is not feasible.

Many innovative research studies have attempted to measure multi-conductor currents at the same time without accessing each conductor individually. Many of these, if not all, exploit the sensor array technique.

A sensor array is a group of sensors deployed on the pre-defined sensing spots in either a random or a special geometric pattern [24]. The sensors in the sensor array system measure signals directly related to the parameters of interest. Usually, more than one parameter are under determining, disables the possibility of solving the problem using one single sensor. Meanwhile, the advantage of using a sensor array is that an array configuration adds new dimensions to the observation, increasing the opportunities to estimate the unknown parameters with certain sensor placement [25]. The trade-off of the sensor array over a single sensor is the increased complexity of processing the collected signals from each sensor. Therefore, modern signal-processing algorithms and cost-expensive computation processes such as the optimization algorithms are also important chains in the sensor array techniques [26].

The sensor array technique has been widely used in assorted areas such as image processing, acoustic signal identification, and indoor and outdoor positioning [27]-[30]. In this thesis, we deploy a magnetic field sensor array as the sensing element to quantify the electromagnetic field produced by the power conductor currents. The sensor array can be placed near the conductor group of interest to measure the magnetic field flux densities linearly correlated to the currents. These measurements are used to compute the currents

inversely. The sensor deployment locations are either random to facilitate the installation or specially-defined to help the later stage current computation. If the independent sensor quantity equals or exceeds the unknown conductor parameters, one may be able to compute the conductor currents from sufficient sensor measurements. The spatial differences and the magnetic field measurement redundancy among the sensors are adequately used to achieve better computation performance.

To date, the research utilizing the sensor array technique to measure multiple conductor currents has attracted a great deal of interest and achieved many promising results. Different types of current transducers are being utilized to establish open-loop and contactless sensing. Most of these techniques involve the use of magnetic-field-sensing elements placed in close proximity to the conductors of interest. The linear response of many magnetic sensors to magnetic fields allows the currents to be computed by using the constant linear relationship consisting the sensors' and the conductors' positions. The literature review carried out for this thesis categorizes three types of magnetic field sensor array techniques that have been proposed and/ or developed as follows.

The first type requires every sensor position and all conductor positions to be completely known. References [31]-[39] proposed several comprehensive measurement systems with different magnetic field sensors; reference [31] proposed the use of multiple hall sensors to provide circulated sensing architecture. The follow-up study [19] proposed a finite element calculation method to process the magnetic sensor array data and infer the conductor current more precisely.

Unfortunately, the current measurement accuracy of this type of research is dependent on the accuracy of the known system geometric parameters, i.e., on the positions and angular orientations of the sensors in relation to the conductors. This requirement increases the technical difficulty of deploying the array sensors, as the geometric quantities need to be measured precisely when the sensors are installed. The computation algorithm is subject to

inaccuracy or diverges when the sensors or conductors deviate from the specific, known position. More importantly, for the situation described in Section 1.2, the conductor positions are normally difficult to obtain.

The second type as reported in [40] and [41] is based on the known sensor positions and assumed conductor positions. This type of method assumes that the multiple conductors are evenly placed in a triangle shape or placed in a straight line, corresponding to the center of the polar coordinate plane, i.e., the measurement plane. The conductor configuration is selected by the user, allowing the device to use an assumed relative cable-sensor geometric layout to compute the currents. The relative polar angle and polar radius for each sensor is treated as known and can be maintained constant by the enclosure.

This improved method is more feasible in practical life than the first type, especially for the multiple-conductor cable current measurement (e.g. Romex cable current measurement) since the cable is usually manufactured according to certain standard (CSA, NEMA, UL, CE etc.) [42]. However, a significant measurement error occurs when the cable conductors deviate from the pre-assumed positions. Also, this method is able to measure only a limited cable configuration and does not suit for the enclosed conductor problems discussed in Section 1.2, where the conductors are placed in an arbitrary format.

The third type of techniques utilizes extra magnetic sensors to create an over-determined linear system. Theoretically, if there are N conductors, N or more than N magnetic sensors are required to solve the currents. This type of method formulates the measurement system as an optimization problem. A far greater quantity of sensors, for example, M sensors ($M \gg N$), are used in an array configuration, in an attempt to compute the currents. Assorted numerical optimization algorithms are used in the time-consuming iterations to determine the currents by minimizing the differences between the calculated values and measured values from the sensors, as reported in a patent [43] and the research articles [44], [45].

However, some feasibility studies revealed that a satisfactory initial boundary condition can be difficult to find, as the optimization algorithms rarely converge to the correct results, in addition to requiring a very long computing time.

1.2 Challenges of Multi-Conductor Current Measurement

Multi-conductor current measurement is a common task in modern power systems, ranging from residential, industrial to utility practices. In contrast, how to measure currents in the conductor group of interest without accessing every individual conductor has been a challenging problem but with many practical needs. This section demonstrates three typical example challenges as below.

- Enclosed conductors

Enclosed conductors are widely used in power distribution systems. In North America, the service conductors entering a residential home or a commercial facility from the utility side are normally enclosed in a conduit, as shown in Figure 1.5. Although the conduit provides good insulation, its presence makes the current measurement difficult to conduct by using the traditional current-sensing techniques, which usually require every single conductor to be isolated and completely encircled by the clamp-on current probe.

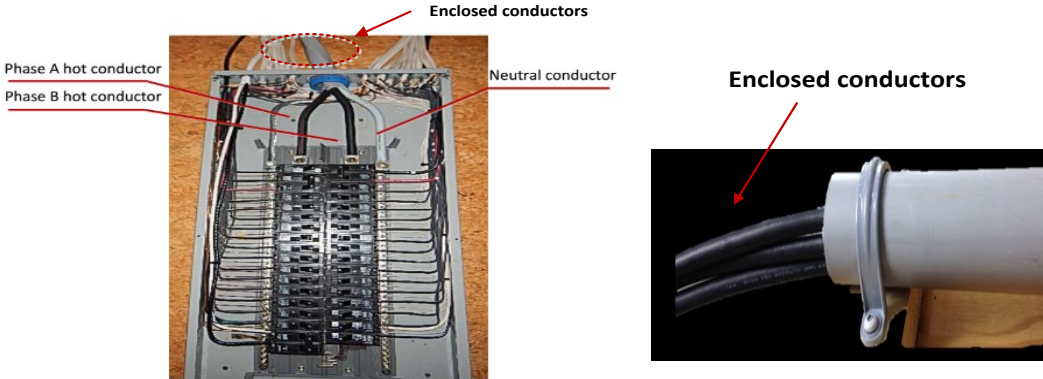


Figure 1.5: Enclosed conductor examples: Left - residential service conductors fed into the home panel, Right - the three service conductors enclosed in the conduit.

- Non-split conductor bundle

Similarly, technical challenges are also encountered when dealing with multi-core power cables. The current information flowing through certain conductors in a cable (such as the phase current or the neutral current) is essential in order to identify the loading status. However, the bundled conductors in a cable are wrapped up by an insulation sheath, as shown in Figure 1.6. Splitting the conductors without rupturing the sheath layer is generally not feasible. In other words, the traditional current measurement methods that require current sensing setup on each single conductor are again ineffective.



Figure 1.6: Non-split conductor examples.

The problems with non-split conductors are even more difficult to solve than those with enclosed conductors, as non-split conductors are usually confined in a small exposure region. The flexibility to install the current sensor and other additional devices to facilitate the measurement is reduced for the inaccessible conductor systems.

- Overhead conductors

The current-sensing capacity for the distribution lines is still very limited. The distributed fault recorders have RMS values at only low resolution. The harmonic current spectrum and phases are hardly stored. Synchronized current waveform information is not applicable for the distribution lines during their normal operation.

The current measurement infrastructure for the distribution systems will not satisfy the

power quality research and troubleshooting, as not enough data are available to analyze to understand the system characteristics. The common method of quantifying the overhead feeder currents is to install expensive clamp-on current probes rated with high insulation grade. However, such installation requires physical contact with high-voltage overhead lines, which is extremely dangerous to personnel safety. More, such devices cannot be deployed for continuous monitoring permanently or during a long period of time. The situation has severely restricted the ability of utility companies to diagnose the distribution systems and troubleshoot power quality issues.

A portable, easy-to-use current-sensing technique for the power industry to estimate the overhead conductor current will be very useful. The measurement system is preferable to be a mobile sensing device lying on the ground surface (as demonstrated in Figure 1.7) and collecting information at the ground level, such as the magnetic fields generated by the overhead line currents. These captured information is used to infer the currents in the overhead conductors. This problem is similar to that introduced in Section 1.2.2, but has its own unique characteristics. The geometric placement for the system is not easy to obtain because of the practical uncertainties, like the uneven ground surface and the different line configurations. As well, the neutral current is not linearly correlated to the phase current combination due to the existence of a multi-grounded network (MGN). The magnetic fields in the practical environment are usually weak and noisy. These challenges need to be studied carefully.

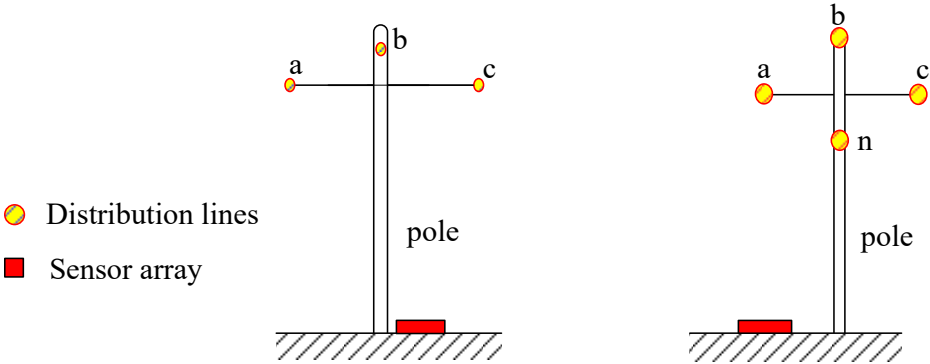


Figure 1.7: Sensor array system to estimate overhead distribution feeder currents.

1.3 Thesis Scope and Outline

This thesis aims to establish solutions for solving different types of current measurement problems involving multiple conductors. The common problems demonstrated in Section 1.2 are explored and investigated. The following tasks are accomplished in this research:

- The distinct natures of three different multi-conductor current measurement problems are studied and formulated accordingly.
- Measurement schemes are proposed to address the special challenges associated with each problem. Detailed design factors such as the sensor selection and arrangement, the relationship between the sensed quantities and the conductor currents, and the least information required to derive the currents are determined via theoretical analysis and simulations.
- The prototype sensor array devices to achieve the proposed schemes are designed.
- The proposed schemes are validated in laboratory tests and actual field conditions.
- The performance (accuracy, stability, and long-time reliability, etc.) of the proposed measurement scheme is evaluated through the test results.
- The improvements for optimizing the proposed schemes are recommended, and their extensions in potential applications are identified.

The remainder of this thesis is organized as follows:

Chapter 2 presents a magnetic field sensor-array-based technique for measuring a group of enclosed conductor currents by using an active sensor calibration scheme. This technique is designed specifically for North American residential systems where three conductors are enclosed in an electric conduit. The proposed technique is formulated in two stages: the calibration stage and the normal current ‘measurement’ stage. The direct application of the

proposed sensor array technique by using the active calibration method is for measuring the currents entering typical North America homes. The prototype measurement system consists of a magnetic sensor array sitting on the home electric conduit, and a calibration device also used for power line communication. Extensive lab and field test results are presented at the end of this chapter.

Chapter 3 presents another solution for the multiple conductor current measurement problem where the conductors are inaccessible. The integration of this technique, combined with the technique introduced in Chapter 2 (which is restricted to the situations where calibration signal injection is difficult), will create a seamless magnetic field sensor array package to address different types of the conductor configurations. Chapter 3 proposes an analytical open-loop sensor array technique, establishing a mathematical system model in order to compute the conductor currents. The preliminary results are presented at the end of this chapter.

Chapter 4 presents a magnetic sensor array technique for measuring the zero-sequence current (ZSC) of the overhead power lines. The proposed scheme uses an array of magnetic field sensors located on the ground level, vertically beneath the overhead lines to compute its ZSC from the magnetic field readings. The proposed scheme can be used to measure the overhead line ZSC regardless of the presence of a neutral conductor. The actual implementation and test results of the proposed overhead power line ZSC measurement technique are also shown in Chapter 4. A prototype measurement system is developed to evaluate the real-world performance of the proposed scheme. Designs to maintain the validity of the theoretical assumptions are integrated to ensure the measurement accuracy. The results from field tests carried out in two actual distribution systems including a three-wire and a four-wire configuration confirmed the validity of the proposed technique.

Chapter 5 summarizes the main conclusions of this study and makes recommendations for future research.

Chapter 2

Multi-Conductor Current Measurement Using Active Calibration Method

This chapter presents a magnetic sensor-array-based technique for measuring currents in a group of bundled or enclosed conductors. The main contributions of this research consist of three ideas:

The first idea is to deploy contactless magnetic field sensors adjacent to the conductors of interest to sense the magnetic field flux densities produced by the conductor currents. For a group of conductors, multiple sensors are used in an array configuration.

With the magnetic field measurements obtained from the sensor array, the problem is reformatted to: how to derive the conductor currents inversely from the measured magnetic fields. It is difficult to compute the currents without knowing the relationship between the sensor outputs and the conductor currents. The second idea is therefore proposed to apply an active calibration scheme to determine this relationship in an automatic manner.

Once the calibration process is completed, the problem becomes solvable. The number of the unknown currents requires at least the same quantity of sensors. More sensors provide the redundancy and a possibility for computing the individual conductor current with higher accuracy. The data processing algorithms form the third idea in this research.

2.1 Introduction

According to electromagnetic theory, an AC current carrying conductor will produce a magnetic field in its surroundings. The strength of the magnetic field at a point in space, i.e., the sensing point, has a relationship with the currents flowing in the conductor. As a result, magnetic sensors which can quantify the magnetic field strength at corresponding locations will provide information regarding the conductor current. If we can determine this relationship, it is mathematically feasible to derive the associated conductor currents.

This field-current relationship is a function of the geometrical arrangement of the conductors and the sensors. If only one single conductor exists, the relationship will be a scalar function. Since there are multiple conductors, an array of sensors, as illustrated in Figure 2.1, is required to derive this relationship.

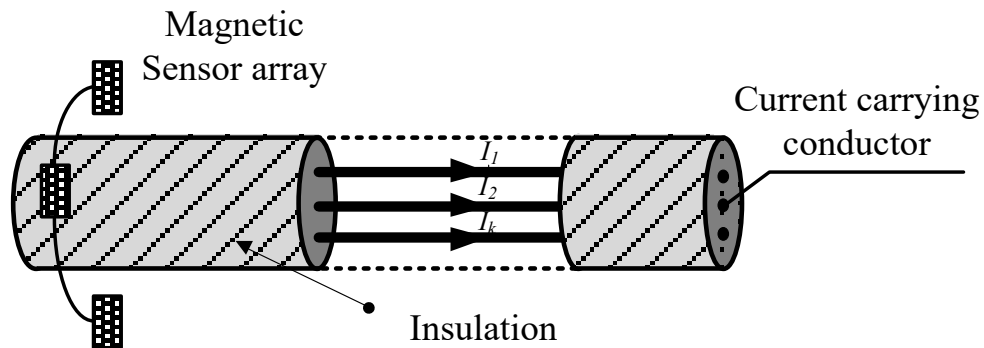


Figure 2.1: Configuration of the magnetic sensor array for enclosed conductor current estimation.

A straightforward way to obtain the relationship is to measure the geometric placement. Unfortunately, the layout of conductors is difficult or even impossible to measure and it is also easily to vary under the enclosed situation. Therefore, geometrical calculation based solutions are not feasible to practice. The key to solve the enclosed conductor current estimation problem is to find a scheme that can establish the relationship between individual conductor current and the sensor array outputs automatically.

This research proposes an active calibration scheme to determine the relationship between the individual conductor current and the multiple sensor array outputs with an automated manner. The proposed magnetic sensor array in conjunction with the active sensor calibration scheme can be a sound solution to accomplish the multiple conductor current measurement tasks.

The direct application of this research is to measure the currents entering typical North America homes. In recent years, the increasing awareness on energy conservation and the development of smart grid have created a great need to monitor the energy use, and to perform better energy management strategy [46], [49], [50]. End uses from the commercial or industrial facilities and the residential homes show strong interests to understand their electricity consumption details.

The residential customers are not satisfied with the total bill indicating the overall electricity consumption. They would like to disaggregate the total power costs into a variety of high demand loads for heating, cooking, refrigeration, and air conditioning, etc., or even to the individual appliances level [51], [52]. Such information will enable residential customers to make informed decisions on the energy conservation and to participate in the demand response programs. Some abnormal electrical activities such as a malfunction of the laundry machine, shutting down of the furnace, etc. can also be noticed timely to prevent unexpected incident. The utility companies, on the other hand, will also be able to gain in-depth understanding on the characteristics of the residential loads and improve their demand response programs.

The research and development of innovative techniques for the home energy use monitoring have, therefore, attracted a lot of interests. One proposed direction is to monitor major household appliances using a sensor network [53], [54]. A competing direction is to measure only the total power consumption of a home and then decompose the power data into individual appliance level through intelligent algorithms [55]-[57]. Regardless which

direction is followed, there is a need to monitor the total currents entering a home.

Literature survey showed that three types of techniques have been proposed or developed to accomplish the task of tracking the total power consumption of a home, as follows:

The first type is to use an optical reader to read the power indicator of a utility revenue meter, thereby infer the power consumption of a home. The reader is typically mounted on the cover of the meter [58], [59]. This technique has several disadvantages. One of them is that the data collected do not have sufficient resolution and contain inadequate information for the load monitoring algorithms. For example, reactive power and harmonic information cannot be collected using this technique.

The second type is to access the data collected by the smart meters (if they are available) [60]. Unfortunately, the majority of smart meters installed so far have low data refreshing rate, such as one sample per 15 minutes, due to the communication constraints. More importantly, there are ownership and legal challenges for a home owner to access the data in real-time, at least for the foreseeable future. Reference [61] is an example product that utilizes the smart meter data to facilitate the home monitoring, i.e., all the data are from the electrical service provider. Customers need authorized activation from the utility to access their home status. The future smart meters could stream the power data wirelessly to homes. However, this will not happen soon since the installed smart meters cannot be replaced just in a few years.

The third type involves installing traditional current and voltage probes inside a customer's electrical panel [50], [62]. Reference [63] presents a monitoring system measure total power usage transitional clamped-on current probes. The retrieved data can be uploaded to the remote server for viewing by the customers. However, it is not practical for many home owners since the home owner need to open the main electrical panel and install the measuring probes, which normally requires to be completed by the licensed professionals.

It is thus not convenient and safe for most of the customers even though the manufacturers instruct them with detailed material such as the product manual and the example installation videos, etc.

2.2 Problem Formulation and the Proposed Scheme

To address the problem discussed in Section 2.1, a magnetic sensor array methodology and its embodiments that can measure currents in a group of enclosed conductors are introduced. It includes two components reside at the upstream and downstream locations of the current flow, depicted in Figure 2.2.

According to the electromagnetic theory, the magnetic field generated by the AC current carrying conductor at a point in space, i.e., the sensing point, is proportional to the current and is inversely proportional to the distance between that point and the conductor. Since many different types of sensors can be used to measure the magnetic field strength, we define the sensor output as the vector $[\mathbf{S}]$. For this linear system, the following relationship will hold:

$$\vec{S}_j = \sum_{m=1}^n k_{jm} \vec{I}_m \quad (1.1)$$

where k_{jm} represents the linear coefficient between the sensor j output (\vec{S}_j) and the conductor currents ($\vec{I}_1, \vec{I}_2, \dots, \vec{I}_m$). This relationship can be obtained both in time domain and frequency domain, enabling a valid vector summation calculation on both the current phasors side, and the sensor responses side.

Rewrite Equation (2.1) to the matrix form we have

$$[\mathbf{S}]_{n \times 1} = [\mathbf{K}]_{n \times n} [\mathbf{I}]_{n \times 1} \quad (1.2)$$

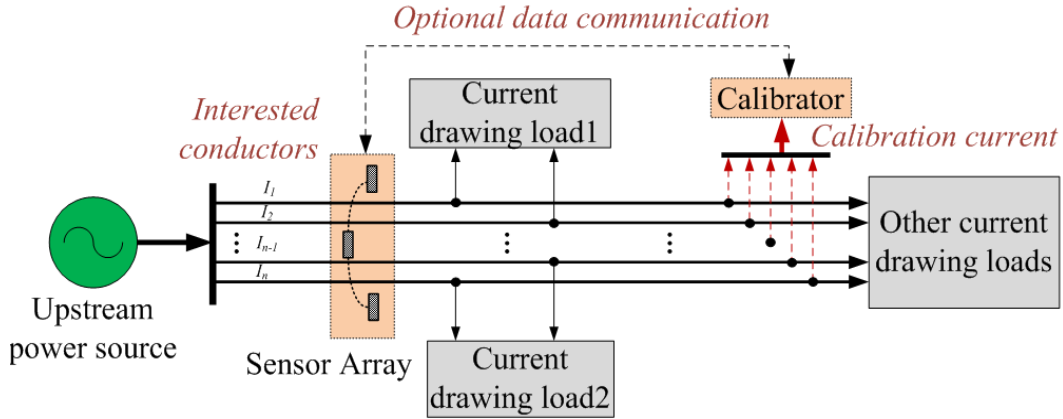


Figure 2.2: Proposed sensor array system for enclosed conductor current measurement.

For a certain measurement, the positions of the sensors and conductors are fixed; meaning the coefficient matrices $[K]_{n \times n}$ are constant. To solve the n dependent conductor currents either in time domain or frequency domain, n magnetic sensors are required to provide necessary array information. If the matrices are known, the conductor currents can be computed according to:

$$[\mathbf{I}]_{n \times 1} = [\mathbf{K}]_{n \times n}^{-1} [\mathbf{S}]_{n \times 1} \quad (1.3)$$

It can be seen that establishing the relationship between the sensor outputs and the conductor currents holds the key for measuring the conductor currents. A commonly known method to determine $[K]$ is to obtain the geometric information of the conductors and sensors [31]–[39]. However, this approach is not applicable for home monitoring since such required information is not attainable. References [43] and [44] utilize redundant magnetic sensors to create an over-determined linear system, optimization algorithms are used to determine the currents by minimizing the differences between the calculated and measured $[\mathbf{S}]$. Extensive case studies revealed that this approach is not applicable to home monitoring either, as the optimization algorithms rarely converge to the correct results, in addition to requiring very long computing time.

This research proposes a calibration scheme to determine $[K]$. A calibrator, which is the

second key component of the proposed technology, is connected to the conductors at a location downstream of the sensor array (also refer to Figure 2.2). The calibrator draws specific currents, named the calibration current, from the conductors for a short period in an automated manner. The characteristics of the calibration currents such as the magnitude and frequency are known to the sensor array through communications. The sensor array uses these known currents to establish the relationship between the conductor currents and its sensed quantities, which is called the calibration process.

The conductor currents sensed by the magnetic sensor array consist of the currents drawn by the calibrator and the currents from other electrical devices also connected to the circuits as follows:

$$[\mathbf{I}]_{n \times 1} = [\mathbf{I}_{calibrator}]_{n \times 1} + [\mathbf{I}_{others}]_{n \times 1} \quad (1.4)$$

Normally, the calibrator is not functioning meaning $[\mathbf{I}_{calibrator}] = 0$, resulting in $[\mathbf{I}] = [\mathbf{I}_{others}]$. Once the calibration is performing on any one of or several of the conductors, the calibrator creates a sudden change on the conductor currents by temporarily drawing certain known currents or current patterns through them.

There is one assumption that the currents flowing to other devices remain the same during the calibration process, i.e., $[\mathbf{I}_{others}] = 0$ is guaranteed during the calibration. As a result, the change of the total circuit current is $[\Delta \mathbf{I}] = [\mathbf{I}_{calibrator}]$. Meanwhile, the sudden change of the conductor currents caused by the calibration currents will also reflect on the sensor outputs as $[\Delta \mathbf{S}]_{n \times 1}$ as

$$[\Delta \mathbf{S}]_{n \times 1} = [\mathbf{K}]_{n \times n} [\Delta \mathbf{I}]_{n \times 1} \quad (1.5)$$

If the calibrator is able to draw n different current patterns from various conductors that all the patterns are not linearly correlated, the sensors will accordingly provide n different outputs, resulting in

$$[\Delta \mathbf{S}_{p1}, \Delta \mathbf{S}_{p2}, \dots, \Delta \mathbf{S}_{pn}] = [\mathbf{K}]_{n \times n} [\Delta \mathbf{I}_{p1}, \Delta \mathbf{I}_{p2}, \dots, \Delta \mathbf{I}_{pn}] \quad (1.6)$$

where p_1, p_2, \dots, p_n represent n calibration events. Utilizing the information for $[\Delta \mathbf{I}]_{n \times n}$ and $[\Delta \mathbf{S}]_{n \times n}$, the coefficient matrix can be finally solved as follows.

$$[\mathbf{K}]_{n \times n} = [\Delta \mathbf{S}_{p_1}, \Delta \mathbf{S}_{p_2}, \dots, \Delta \mathbf{S}_{p_n}] [\Delta \mathbf{I}_{p_1}, \Delta \mathbf{I}_{p_2}, \dots, \Delta \mathbf{I}_{p_n}]^{-1} \quad (1.7)$$

With this arrangement, the sensor array becomes capable of estimating currents in any unknown conductor configuration and arbitrary sensor layout.

It worth mentioning here that we assume the interested conductors are ideal, i.e., the conductors are straight and long enough with the negligible cross section areas. This is normally true for the residential system current measurement situations. However, the conductors may not be always perpendicular to the sensing plane. It is also not surprising that the sensing direction of the sensor is not aligned with the magnetic field direction produced by the conductor currents. Both these two non-ideal situations lead to the conductor-to-sensing-plane angle less than $\pi/2$ as shown in Figure 2.3. On the sensing plane, a sensor is located at the origin and we establish a coordinate system at the sensing point (refer to Figure 2.3). The sensor measurement direction is represented as $\vec{\nu}_s$. One current \vec{i} is decomposed into three orthogonal components in this 3-D: \vec{i}_x , \vec{i}_y and \vec{i}_z respectively.

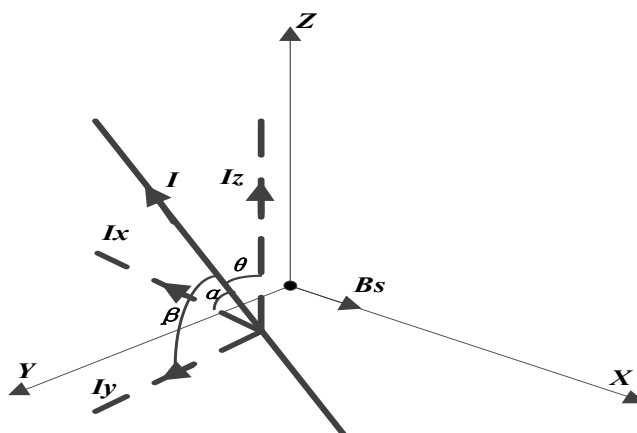


Figure 2.3: The case of one conductor not perpendicular to the sensing plane.

Since the sensor is only able to quantify the magnetic field produced on x -axis direction,

only the M-filed generated by one of the components, i.e., \vec{i}_z will be detected, where

$$\vec{i}_z = \vec{i} \cdot \cos \theta \cdot \sin \alpha \quad (1.8)$$

Hence, the sensor at the origin is only able to sensor the magnetic field projection on its sensing direction as \vec{i}_z , a partial component of the current \vec{i} . However, it can be seen from Equation (2.8) that the relationship between the interested conductor current \vec{i} is still linearly correlated to the sensor measurement.

On the other hand, the angle displacement caused by the two factors introduced above will be taken account into the coefficient matrix $[K]$ and will be calibrated automatic by the proposed active calibration method. The details of this calibration scheme will be explained in the next section.

In summary, the relationship needed to infer the conductor current can still be obtained and the orientations of the conductors in respect to the sensors will be bring any complexity or challenge to the proposed method, which is usually not possible to be solved by the traditional sensor-array-based current measurement methods (they usually assume the conductors are ideally placed perpendicular to the sensing plane, or treat the angle displacement from the conductor orientations to the sensing plane as an negligible error).

One typical case of the proposed technique is to measure three enclosed conductors in the electric conduit, where $n=3$ in the descriptions above. A real-world example of this set-up is the power feed of North America residential home, where three conductors A, B and N are energized under the setting that A is with +120V while B is with -120V, N is the neutral. Three magnetic sensors, S_1 , S_2 and S_3 are therefore deployed attaching to the conduit based on the proposed scheme. Still, the strength of the magnetic field at a point in space, i.e., the sensing point, is proportional to the current and is inversely proportional to the distance between that point and the conductor (Figure 2.4).

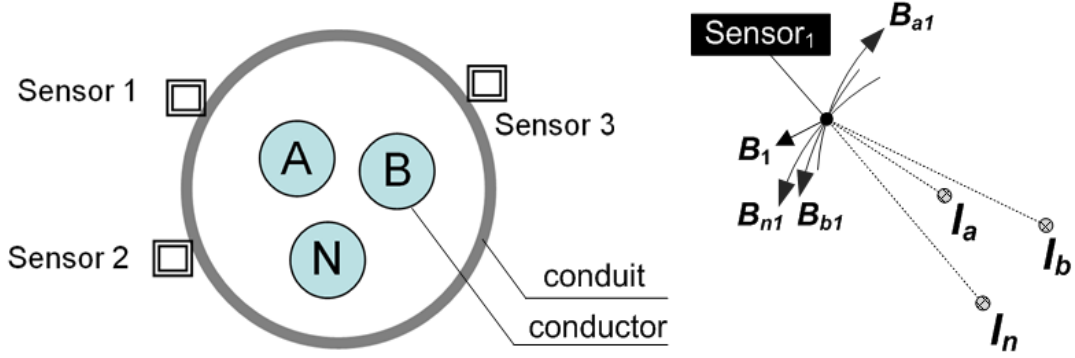


Figure 2.4: The magnetic sensor array deployed around a conduit.

For this three-conductor-three-sensor system, the following relationship described in both time domain and frequency domain will hold:

$$\begin{bmatrix} S_1(t) \\ S_2(t) \\ S_3(t) \end{bmatrix} = \begin{bmatrix} k_{1a} & k_{1b} & k_{1n} \\ k_{2a} & k_{2b} & k_{2n} \\ k_{3a} & k_{3b} & k_{3n} \end{bmatrix} \begin{bmatrix} i_a(t) \\ i_b(t) \\ i_n(t) \end{bmatrix} \quad (1.9)$$

$$\begin{bmatrix} S_1(\omega) \\ S_2(\omega) \\ S_3(\omega) \end{bmatrix} = \begin{bmatrix} k_{1a}(\omega) & k_{1b}(\omega) & k_{1n}(\omega) \\ k_{2a}(\omega) & k_{2b}(\omega) & k_{2n}(\omega) \\ k_{3a}(\omega) & k_{3b}(\omega) & k_{3n}(\omega) \end{bmatrix} \begin{bmatrix} i_a(\omega) \\ i_b(\omega) \\ i_n(\omega) \end{bmatrix} \quad (1.10)$$

where S_1 , S_2 and S_3 denote the output of sensors 1, 2 and 3; i_a , i_b and i_n represent the AC current flowing through the conductors. Equation (2.9) states the relationship in time-domain while Equation (2.10) indicates the frequency-domain relationship.

2.3 Sensor Array Calibration

This research proposes a calibration scheme to determine $[K]$. A calibrator, which is the second key component of the proposed technology, is connected to the conductors downstream of the sensor array. To help understanding, we still use the three-conductor-three-sensor system shown in Figure 2.5 as an example to introduce the proposed scheme. However, it should be noticed that the proposed scheme is versatile for any n conductor

systems.

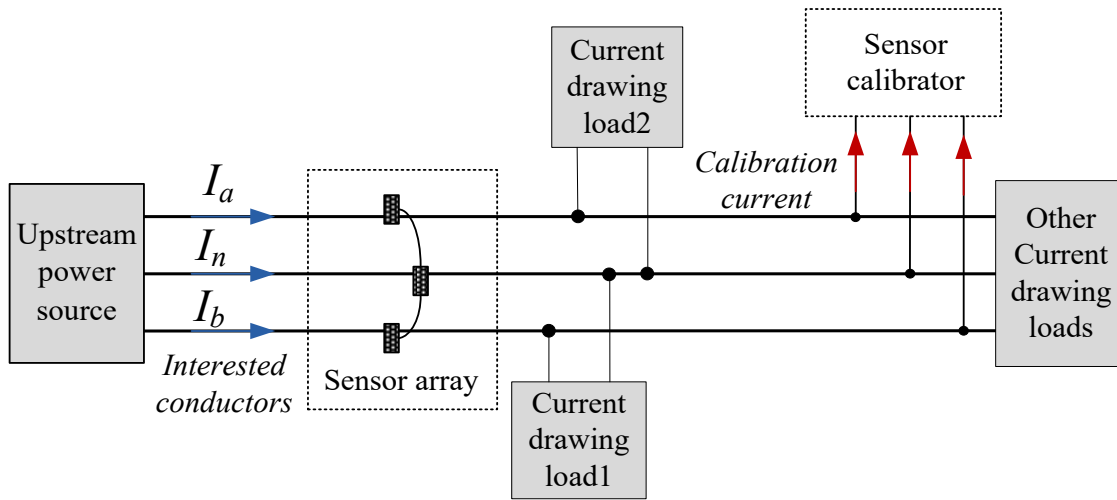


Figure 2.5: Magnetic sensor array with an automated calibrator.

Using the power electronic switching, the calibrator draws specific currents and current patterns for a short period in an automated manner. As a response, the sensor array will detect and extract such patterns that are reflecting on the sensor outputs. If the sensor array is able to know the calibration current information, it can use the patterns from the calibrator and the sensor extractions to establish the matrix $[K]$. Once this relationship is established, the sensor array can start to “measure” the conductor currents by calculating them using that relationship and the sensed magnetic fields.

2.3.1 Calibration Pattern Generation

The calibrator is expected to create three distinct momentary current patterns. The scheme to achieve this goal is shown in Figure 2.6. In this scheme, simple thyristor switches are only fired in one cycle and remain un-triggered in the following consecutive cycle, generating a series of current pulses every other cycle. These current pulses are used to create the calibration current.

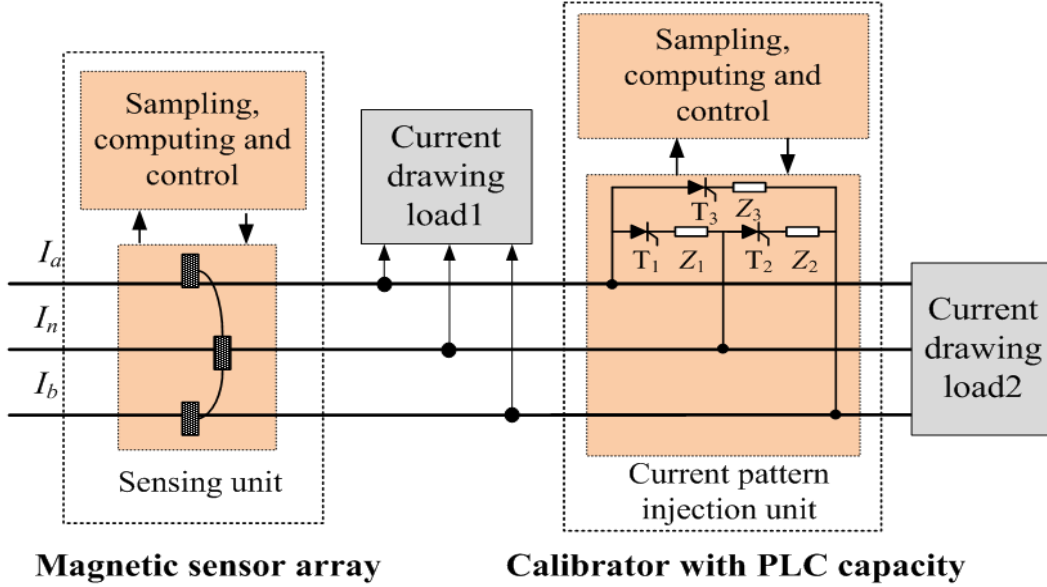


Figure 2.6: The system configuration of the sensor array with the calibrator.

The principle of the calibration scheme is demonstrated as the follows. During a single calibration event, the conductor currents consist of the currents drawn by the calibrator and the currents from other electrical loads also connected in the circuit, as follows:

$$[\mathbf{I}]_{3 \times 1} = [\mathbf{I}_{calibrator}]_{3 \times 1} + [\mathbf{I}_{others}]_{3 \times 1} \quad (1.11)$$

The corresponding sensor output is represented as $[\mathbf{S}]_{3 \times 1}$. After the waveforms of $[\mathbf{S}]_{3 \times 1}$ are acquired, their $(n+1)^{\text{th}}$ cycle data is subtracted by the n^{th} cycle data ($n=1,3,5,\dots,11$), creating a new set of data denoted as $[\Delta\mathbf{S}]_{3 \times 1}$. If the cycle-by-cycle subtraction is performed on the current $[\mathbf{I}]_{3 \times 1}$, one will get $[\Delta\mathbf{I}]_{3 \times 1}$ similarly.

Since the calibration current pattern only exists in either the n^{th} cycle or the $(n+1)^{\text{th}}$ cycle, the cycle-by-cycle subtraction performed to determine $[\Delta\mathbf{S}]_{3 \times 1}$ and $[\Delta\mathbf{I}]_{3 \times 1}$ will filter out the quantity only related to the calibration current whatever the current side or the sensor array side. Usually, the loads draw the same current every cycle during this short calibration period, the equation $[\Delta\mathbf{I}]_{3 \times 1} = [\mathbf{I}_{calibrator}]_{3 \times 1}$ holds, which leads to:

$$[\Delta\mathbf{S}]_{3 \times 1} = [\mathbf{K}]_{3 \times 3} [\mathbf{I}_{calibrator}]_{3 \times 1} \quad (1.12)$$

The proposition of this easy-to-use, reliable calibration scheme is the most important innovations in this research. Its main innovative design is that the calibration current contains a special pattern: it is created every other cycle. The difference of the currents between two consecutive cycles is the calibration current. As a result, this scheme is immune from background waveform distortions and the impact of currents from other loads can be eliminated.

The second advantage of drawing current every other cycle is that the peak instant of the calibration current (current pulse caused by the thyristor switching, will explain more specifically in the next section) can be detected at the sensor side. This instant is used to synchronize the phasor $[\mathbf{S}]$ with the phasor $[\mathbf{I}]$. Note that to solve for $[\mathbf{K}]$, both phasors must be synchronized to the same time instant.

After the calibration current generation, to determine the matrix $[\mathbf{K}]$, the sensor array requires the information of the calibration current $[\mathbf{I}_{calibrator}]$. $[\mathbf{I}_{calibrator}]$ is transmitted to the sensor location also by the calibrator in the same manner with the current pulses. In other words, the calibrator is also a power line communication device. The integration with a so called Power Line Signaling scheme [47] into the calibrator creates a self-contained system, which is the third innovation of the proposed technique. As a result, the sensor system does not require other additional communication methods. How to achieve such communication between the calibrator and the sensor array will be explained in Section 2.5.

In general, the calibrator is designed to draw three distinct current patterns from various conductor combinations. Three calibration events will result in:

$$[\Delta\mathbf{S}_{p1}, \Delta\mathbf{S}_{p2}, \Delta\mathbf{S}_{p3}] = [\mathbf{K}]_{3 \times 3} [\Delta\mathbf{I}_{p1}, \Delta\mathbf{I}_{p2}, \Delta\mathbf{I}_{p3}] \quad (1.13)$$

where $p1$, $p2$ and $p3$ represent three different current patterns.

For the above equation, both $[\Delta\mathbf{S}]_{3 \times 3}$ and $[\Delta\mathbf{I}]_{3 \times 3}$ are known. It is therefore not difficult to

derive the matrix $[K]_{3 \times 3}$ as the follows:

$$[K]_{3 \times 3} = [\Delta S_{p1}, \Delta S_{p2}, \Delta S_{p3}] [\Delta I_{p1}, \Delta I_{p2}, \Delta I_{p3}]^{-1} \quad (1.14)$$

2.3.2 Characteristics of Calibration Current

To analyze the characteristics of the calibration current pattern, the case of calibration made between conductor A and N is utilized as an example (refer to Figure 2.7). The simplified equivalent circuit along the calibration route is shown in Figure 2.7 (a). In this circuit, Z_{sys} represents the system impedance upstream of the calibrator. There is an impedance Z_{SCR} in series with the thyristor. Its purpose is to limit the calibration current. Extensive studies conclude that a resistor is the best option from a number of perspectives, such as the size and the cost.

The simplified equivalent circuit is shown in Figure 2.7 (b). The load is neglected in the equivalent circuit as its impact on the calibration current is small, which is similar to the short-circuit analysis where the loads can be neglected.

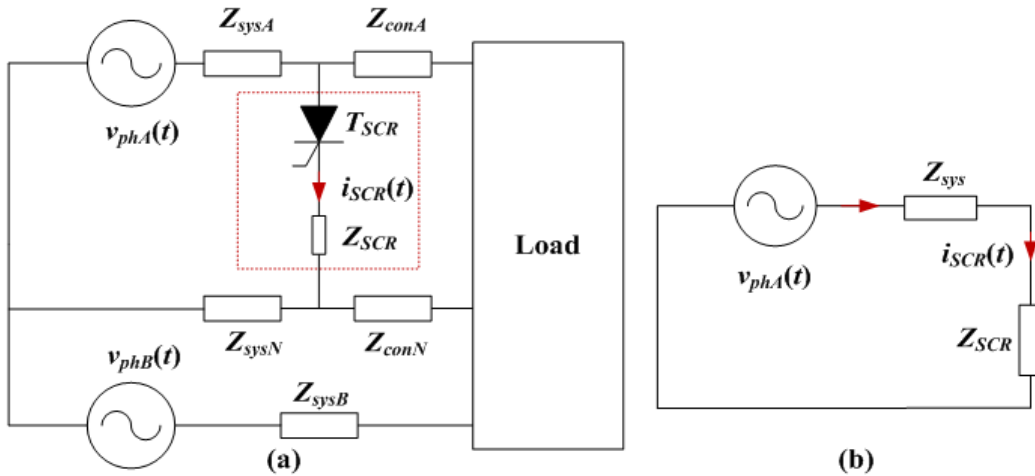


Figure 2.7: Circuit analysis when calibration is performed on phase A-N. (a) the representing circuit for the residential system; (b) the equivalent circuit for the calibration current flowing loop.

The steady-state phase A-N voltage is expressed as

$$v_{phA}(t) = \sqrt{2}U_{ph} \sin \omega t \quad (1.15)$$

If the thyristor firing angle is selected as δ_1 , the corresponding waveforms of the thyristor current, i.e., the calibration current is:

$$i_{SCR}(t) = \frac{\sqrt{2}U_{ph}}{R_{sys} + \omega L_{sys} + R_{SCR}} \sin \omega t, \omega t \in [\pi - \delta_1, \pi] \quad (1.16)$$

Figure 2.8 shows the calibration current as well as the thyristor voltage waveform before and after the thyristor conduction.

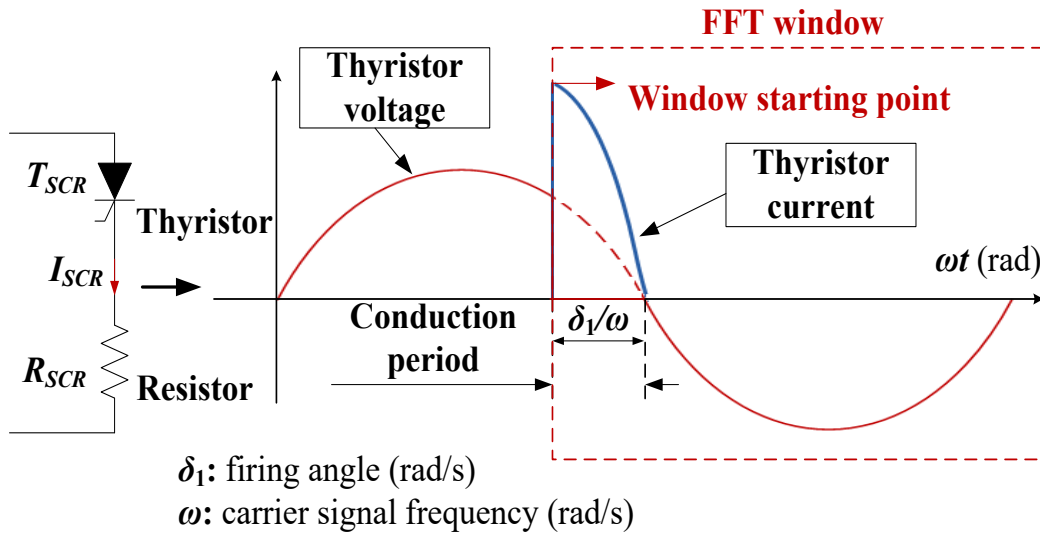


Figure 2.8: Thyristor voltage and current waveform for resistive connection.

In the actual implementation, the calibration current is processed by the Fast Fourier Transform (FFT). The FFT window starts at the current peak as shown in Figure 2.8. This window position must be detected and used at the sensor location so that $[\Delta S]_{3 \times 1}$ and $[\Delta I]_{3 \times 1}$ are synchronized.

Figure 2.9 illustrates one set of waveforms during the calibration process. The firing angle is set to 90° after the rising edge of carrier voltage V_{AN} .

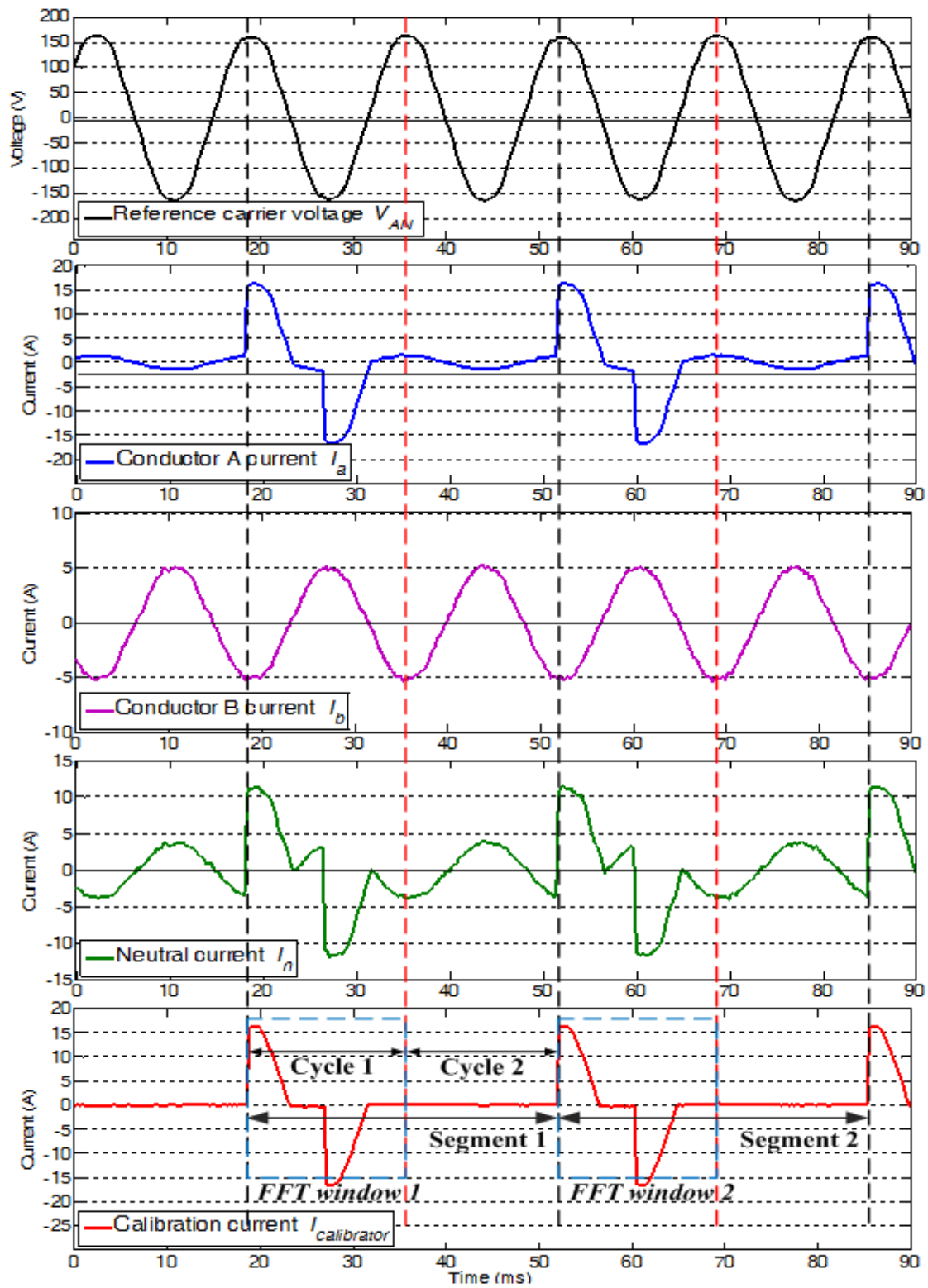


Figure 2.9: System voltage and conductor current during A-N calibration.

In Figure 2.9, each calibration pattern in one segment consists of two cycles, the first cycle of Segment 1 contains the calibration signal and the second cycle does not. During the calibration, a current pulse is suddenly injected into the conductor combination A-N. Meanwhile, conductor B current is not involved and the current flowing through phase B remains almost unchanged.

The calibration current that the sensor array used to generate the matrix $[K]$ is sampled at the calibrator location. A good consistency of the calibration current at the two different locations is important to ensure the $[K]$ matrix can be computed accurately. Two consecutive cycles of the conductor current during the calibration event are subtracted by each other. The results should be equal to the current drawn by the calibrator.

The waveforms presented in Figure 2.9 have proved that satisfactory agreement is achieved at the two locations.

2.3.3 Calibration Pattern Extraction

The sensor array always detects and records the states of the system. Once the sensor array is notified the starting of the calibration state. The entire process on the sensor outputs involving the calibration patterns will be collected. Figure 2.10 shows the sensor output during this state.

The first cycle of segment 1 contains the calibration current. It shows up in the voltage output of the sensor circuits. Due to the existence of the background current drawn by other loads, three sensor outputs on the cycle 2 are not zero.

To obtain the sensor output related to the calibration current only, a signal extraction algorithm subtracts the void cycle (cycle 2) from the signal containing cycle (cycle 1) on each of the sensor output waveform respectively.

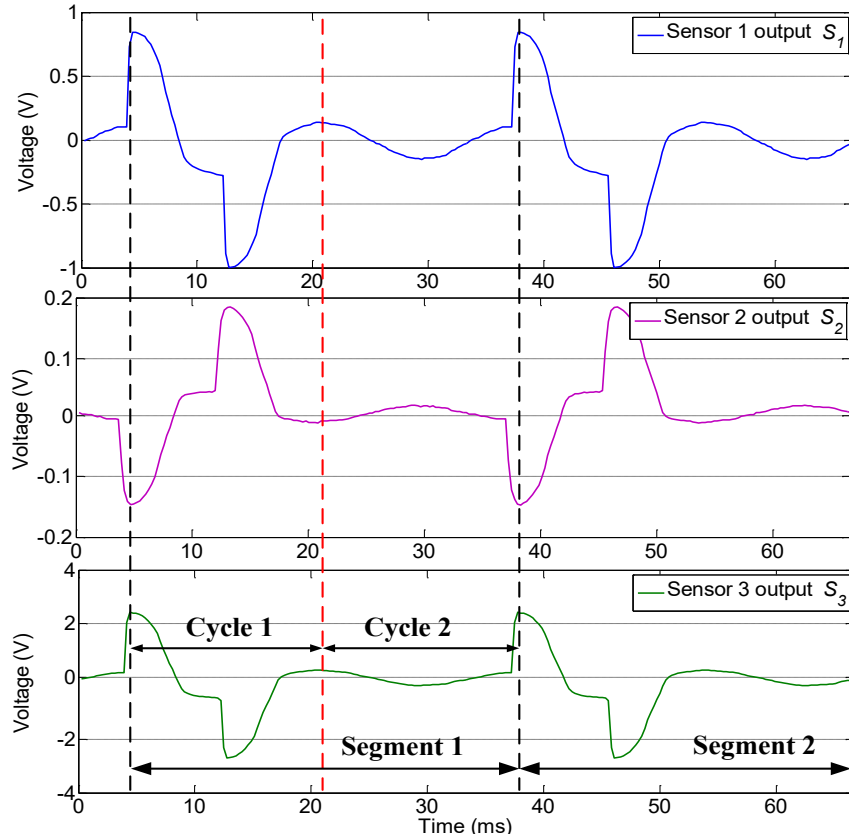


Figure 2.10: The three sensor outputs during one calibration.

The post-subtraction waveforms for the three sensors, i.e., ΔS_1 , ΔS_2 and ΔS_3 , are depicted in Figure 2.11. The FFT window is selected starting from the top peak of the $[\Delta S]_{3 \times 1}$ waveforms. This window is similarly used in Figure 2.10 for the calibration current so the synchronization for $[I_{\text{calibrator}}]_{3 \times 1}$ and $[\Delta S]_{3 \times 1}$ is guaranteed.

Based on the FFT results of $[I_{\text{calibrator}}]_{3 \times 1}$ and $[\Delta S]_{3 \times 1}$, the coefficient matrices at both the fundamental (60 Hz) and 3rd harmonic (180 Hz) frequencies are computed and stored in the sensor circuit memory unit.

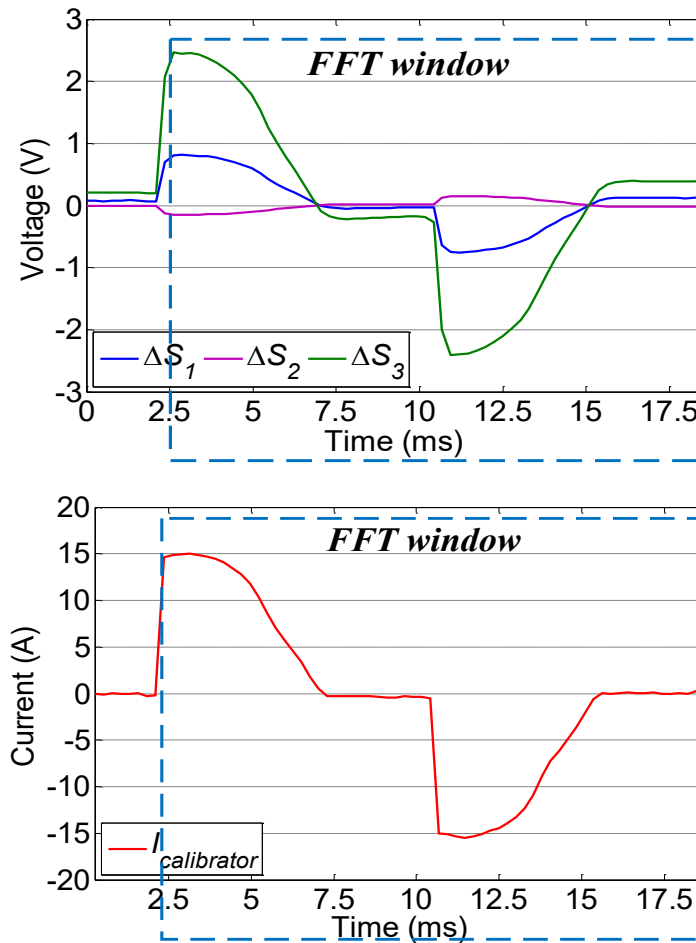


Figure 2.11: Extracted sensor outputs that are due to the calibration current.

2.4 Application for Residential Home Current Monitoring

The direct application of this research is to measure the currents entering typical North America homes. This section presents the measurement scheme and a set of prototype device. Its hardware and software construction has been illustrated in this section.

One typical North America home is presented in Figure 2.12. Such residential home is supplied by the three-power cable from the electrical utility. Three conductors A, B and N, come inside the home through an electric conduit. The two hot conductors (supply the

phase A and phase B) and the third one as the neutral are enclosed in the conduit until entering the electric panel.

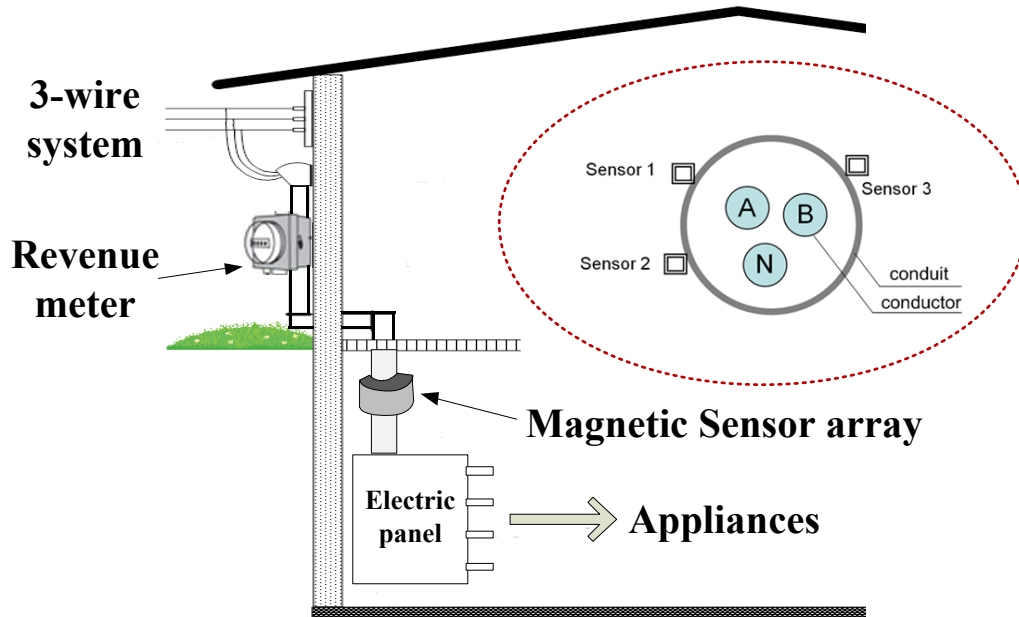


Figure 2.12: Magnetic sensor array installed at residential homes.

The voltage between the phase A to neutral is at the same magnitude but reversed phase as the voltage between the phase B to neutral. In the following context, we assume the conductor A is energized with +120V and B with -120V, creating a +120V system voltage between phase and neutral, and +240V between phase A and B. N is the neutral. All of the household appliances downstream the electric panel are supplied by these voltages and are connected on certain phases among these three combinations.

The proposed home current measuring device, as shown in Figure 2.13, is clamped on the conduit feeding into the electric panel. It is composed by an array of magnetic field sensors. Based on the surrounding magnetic fields sensed by the magnetic sensors, conductor currents inside the conduit are determined computationally.

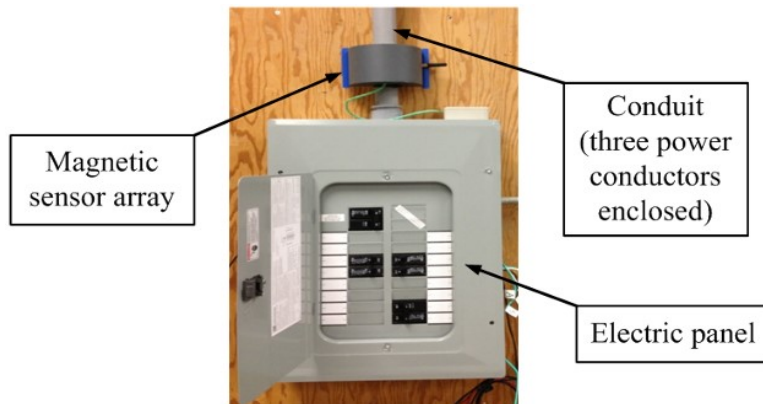


Figure 2.13: Magnetic sensor-array-based current measurement technique.

As the real-time power consumption information can be collected by the proposed sensor array after a successful calibration, it is interesting to present the power monitoring results. There can be many different display options for the information outputted by the proposed system. In the simplest of cases, the total power consumption (both real-time and historical power consumption) can be displayed on a fixed screen or through a website, an end-user interface or an app. on the mobile display. In any of these cases, the power consumption data would be broadcast to a display device capable of receiving the transmission.

The most obvious advantage of the proposed technique is its easiness for installation. There is no electrical contact to the conductors, so a home owner can install it by himself/herself. Additionally, the sensor can deliver data with a resolution of 1 sample per second or higher. Currents in both hot conductors are available and the 3rd harmonic currents are also available. Therefore, it is an ideal fit for the home monitoring strategy. The proposed technique has been evaluated through extensive tests in multiple residential houses. Satisfactory measurement performances have been achieved.

2.4.1 Simplified Two-phase Calibration

Section 2.3.1 introduces a sensor array calibration scheme that the calibrator draws 3

different current patterns from the three conductors in the residential conduit. By adjusting the firing angle of the thyristors and utilizing power resistors with different resistance, distinct calibration signal patterns can be created. However, in the practical experiment to implement this scheme in the real home, we found the third calibration pattern i.e., the calibration pattern on phase A-B is not easy to complete:

- Users can find outlets connected on phase A-N or phase B-N, with the instruction on the electric panel labeling, or just simply try different floors and rooms. However, the outlets connected on phase A-B are usually available only at locations where major appliances are placed, such as the laundry machine and the electric range, etc. These appliances can barricade the outlets and make the calibrator difficult to access the phase A-B.
- Moreover, the NEMA (National Electrical Manufacturers Association) four-prong electrical sockets used in North America can be different in the prong configuration depending on their voltage rating, current capacity, and grounding requirement. Example sockets connected on phase A-B are demonstrated in Figure 2.14. Different sockets configuration will further increase the uncertainty for the calibrator to plug into phase A-B.

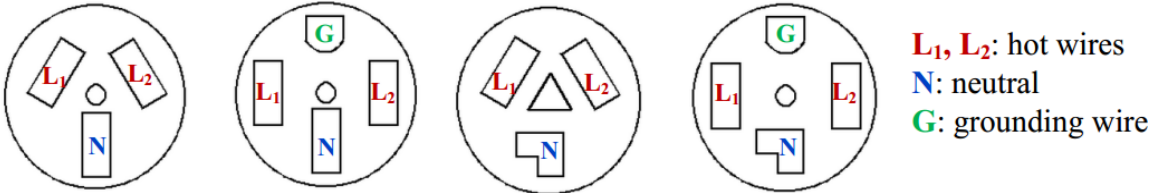


Figure 2.14: different socket types for phase A-B connection.

The scenario explained above reduces the feasibility of proposed conductor current estimation scheme and makes the proposed sensor calibration scheme not easy to apply. For the actual implementation, the calibrator is a portable device that draws the current from

two home outlets only (A-N and B-N). This is shown in Figure 2.15. This simplification has two advantages: Firstly, it simplifies the calibrator and reduces its cost. Secondly, it avoids the use of four-prong outlets which are difficult to access in some homes. Note that the currents flowing through A and B conductors will return through the neutral N.

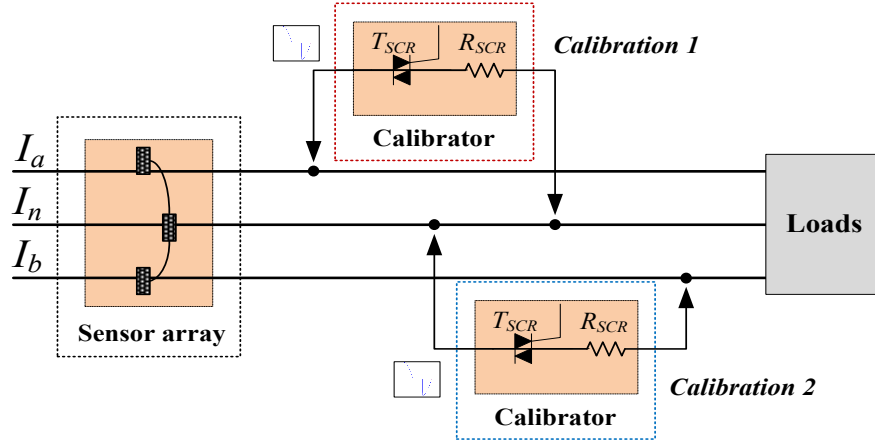


Figure 2.15: Two-phase calibration scheme for the actual implementation.

A detailed circuit analysis will show that the neutral current is related to the phase currents linearly as follows [64], [65]:

$$\Delta I_n = K_a \Delta I_a + K_b \Delta I_b \quad (1.17)$$

The values of k_a and k_b are dependent on the impedance parameters of the residential system [64], [65]. By considering such practical current returning characteristic in the actual home, the calibration current this time becomes:

$$[\mathbf{I}_{calibrator}]_{3 \times 1} = \begin{bmatrix} 1 & 0 \\ 0 & 1 \\ k_a & k_b \end{bmatrix} \begin{bmatrix} \Delta I_a \\ \Delta I_b \end{bmatrix} = [\mathbf{K}']_{3 \times 2} [\mathbf{I}'_{calibrator}]_{2 \times 1} \quad (1.18)$$

Substitute Equation (2.18) to Equation (2.12) results in:

$$[\Delta \mathbf{S}]_{3 \times 1} = [\mathbf{K}]_{3 \times 3} [\mathbf{K}']_{3 \times 2} [\mathbf{I}'_{calibrator}]_{2 \times 1} = [\mathbf{M}]_{3 \times 2} [\mathbf{I}'_{calibrator}]_{2 \times 1} \quad (1.19)$$

where $[\mathbf{M}]_{3 \times 2} = [\mathbf{K}]_{3 \times 3} [\mathbf{K}']_{3 \times 2}$ is the modified coefficient matrix, which is determined

through the simplified calibration process.

Finally, phase A and phase B conductor currents in residential system can be computed as follows:

$$[\mathbf{I}]_{2 \times 1} = ([\mathbf{M}]_{3 \times 2}^T [\mathbf{M}]_{3 \times 2})^{-1} [\mathbf{M}]_{3 \times 2}^T [\mathbf{S}]_{3 \times 1} \quad (1.20)$$

Where the coefficient matrix $[\mathbf{M}]_{3 \times 2}^T$ is the transpose matrix of $[\mathbf{M}]_{3 \times 2}$.

The above equation reveals that this matrix can be determined by drawing calibration current at phase A first and then at phase B. Many electrical panels will have labels to indicate the phase connections for certain outlets or the specific room. Figure 2.16 shows one typical home panel in a pilot test house that all rooms are distinguished and labelled to suggest the corresponding two-phase distributions. The home owner will easily complete the two calibrations following these labels, to conductor the calibration at two locations where they attributed to two different phases according to the panel labels.

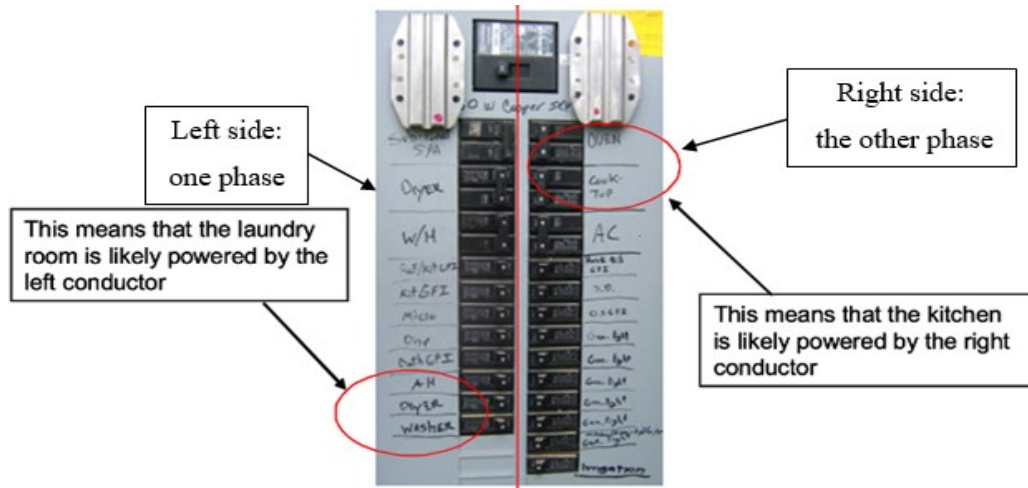


Figure 2.16: Two-phase calibration in reference to the home electrical panel labels.

In other cases that the labels are not available, or the home owners do not consult with the labels, the home owner can simply try multiple outlet locations to complete the sensor array

calibration. An exclusively designed phase identification algorithm is integrated in the proposed device to ensure the completion of the two-phase calibrations. The home owner conducts the calibration through the following steps:

1) The first calibration

After installing the sensor array, the home owner can plug the calibrator into any outlet to activate the first calibration on one of the phases. Assuming it is performed between phase A-N, the calibration current pattern is $[\mathbf{I}'_{calibrator}]_{p1} = [\Delta I_a \quad 0]^T$.

2) The second trial calibration

The sensor array stored the information from the first calibration and waits for the calibration signal on the other phase. Like the first step, the user can perform the second trial calibration on another arbitrary outlet. However, it is possible that the 2nd outlet is in the same phase as the 1st outlet. The sensor can detect this case by comparing the $[M]_{3 \times 2}$ matrices.

If the two calibrations are on the same phase, one column of $[M]_{3 \times 2}$ will be linearly correlated. Since all the elements in $[M]_{3 \times 2}$ are phasors, the correlation extent of the two columns can be evaluated by the vector distances as:

$$d_M = \sqrt{\sum_{i=1}^3 |\bar{M}_{ia} - \bar{M}_{ib}|^2} / \sqrt{\sum_{i=1}^3 |\bar{M}_{ia}|^2} \quad (1.21)$$

where \bar{M}_{ia} is calculated from the data obtained from the first calibration. \bar{M}_{ib} becomes known by the second calibration, $i=1, 2, 3$. d_M represents the similarity of the two columns of $[M]_{3 \times 2}$, only if d_M exceeds a threshold (35% in the actual implementation). It is believed that the second trial calibration is performed on the different phase. Otherwise, the sensor will indicate the user to repeat step 2 at another outlet location. The calibration procedures are further demonstrated as the flow chart shown in Figure 2.17.

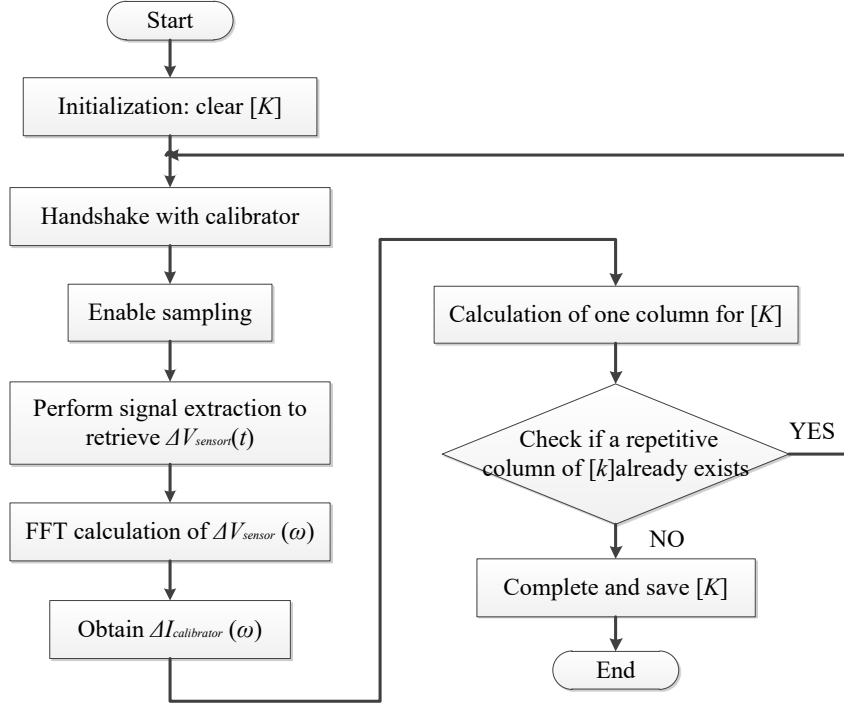


Figure 2.17: Flow chart of a complete calibration process.

2.4.2 The Calibrator Prototype

To validate and evaluate the proposed current-sensing scheme, a series of hardware and software are designed. The entire work presented in this section involved a concept trail and multiple of revisions and improvements. The final prototype devices are able to be operated by the home owners with only little amount of training provided together with the devices in a manual, or the online video instruction, etc.

The hardware implementation of the calibrator is shown in Figure 2.18. The size is slightly larger than a smart phone. The anti-parallel thyristors serve to generate current pulses through the conductors of interest. The $10\Omega/25W$ 1% tolerance power resistors are integrated in series connection with the thyristor pair. The current sensors are embedded on the printed circuit board to measure the calibration current accurately. Initiated by pressing the activation button by the user, the calibration request is made.

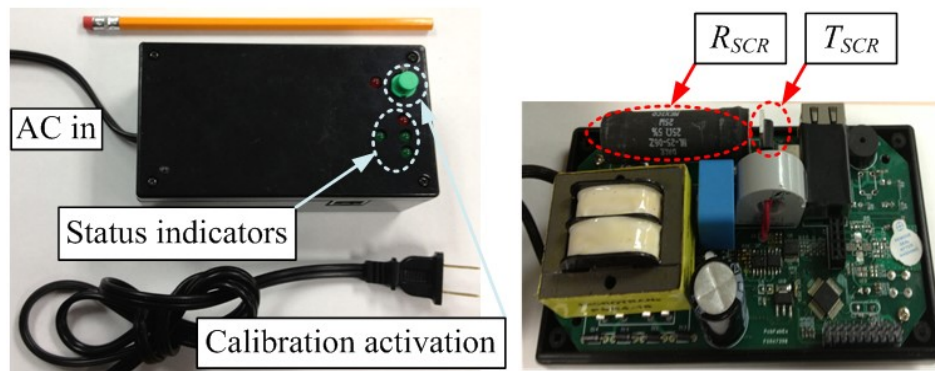


Figure 2.18: The prototype of the sensor calibrator.

The system voltage, say, phase A to neutral (denoted as A-N sequence) or phase B to neutral (denoted as B-N sequence), is applicable to provide the reference carrier waveform in order to control the gating operation. The thyristor is fired several degrees prior to the carrier voltage reaching the zero-crossing point. It remains conducted until the thyristor current pass the zero-crossing point. After this instant, the thyristor is anti-biased and therefore can be turned off automatically. Gating signals to the thyristors from a MCU creates a sequence of signal pulses. An optical coupler acts as the isolation interface between the control end and the high voltage side to achieve safe operation.

2.4.3 The Sensor Array Prototype

A prototype of sensor array system has also been developed to evaluate the performance of the proposed calibration scheme. The final sensor array prototype is already presented in Figure 2.13. Its features a clip-on design that can be installed directly onto the electric conduit above the panel easily.

The sensor array consists of a front-end analog chain to process the sensor signals. The analog front end measures the induced voltage across the pick-up coil sensors. It followed by a low-pass filter that attenuates the high frequency noises. Considering the wide range of conductor current ampere, two stages of amplifiers are selected to improve the resolution

under both small current and large current situations. A final low-pass filter reduces aliasing before sampling the two-stage signals. A MCU for control and post-computation, and some peripherals: a 6-channel 16-bit simultaneous analog-to-digital converter (ADC) and a power supply circuit connected to high voltage side. The block diagram of the sensor array device can be seen in Figure 2.19. A picture of the prototype magnetic sensor array device has already been shown in Figure 2.13.

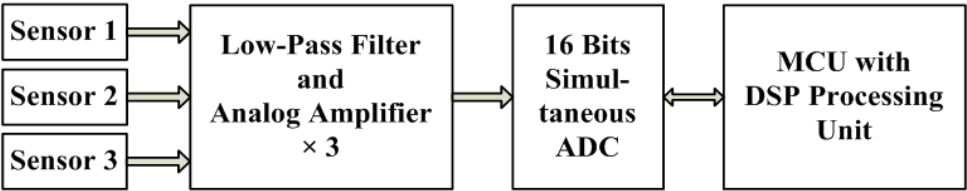


Figure 2.19: Circuit diagram of the magnetic sensor array.

The input of the analog front-end is the sensor output voltage. It followed by a low-pass filter that attenuates the high frequency noises. Considering the wide range of current usage of normal residential homes, two-stage amplifiers are selected to improve the sensitivity under both small current and large current situations. Unless saturated, the second stage output is used to take the input range of ADC sufficiently. A final low-pass filter reduces the aliasing before sampling the two-stage signals. The sampling rate of the ADC is 128 points/cycle (7.68 kHz), which is enough to provide the fundamental and harmonic information.

2.5 Lab and Field Test Validations

Extensive lab and field tests are conducted to evaluate the proposed sensor array devices. The test has demonstrated that the proposed technique can provide adequate current measurements for residential homes.

2.5.1 Lab Test Results

The proposed sensor array system was tested in lab first. An experiment bench as seen in Figure 2.20 mimicked the typical electric panel setup in a residential home. The reference values of the two-phase currents were measured by the current probes. A 16-bit NI-DAQ instrument based data equipment continuously recorded the reference currents, which were compared with the computed currents by the proposed technique.

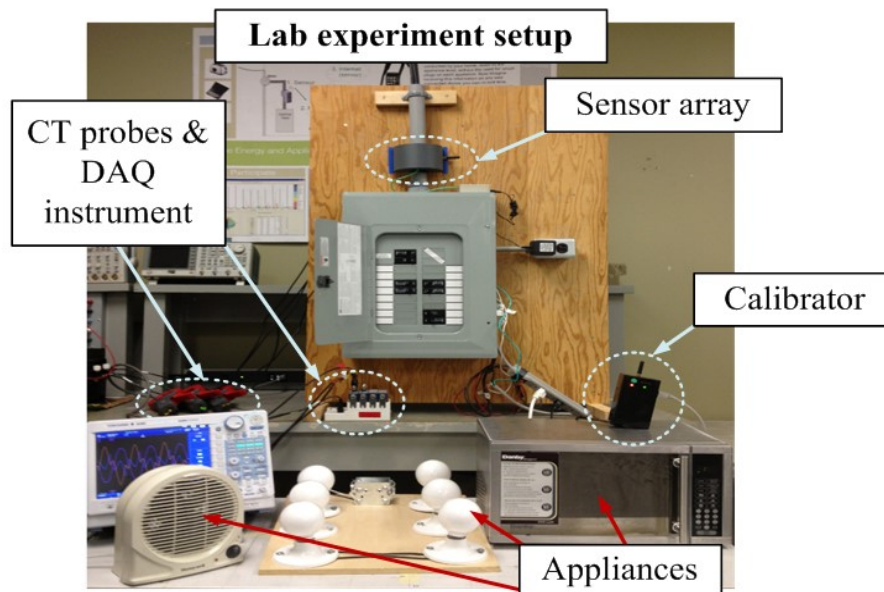


Figure 2.20: Lab experimental bench with sensor array installed.

The variation of the load currents are accomplished by varying different loads supplied by the panel. Figure 2.21 shows the comparison of the calculated currents by the technique (“sensor”) and those measured directly by the current probes (“CT”) at the resolution of 1 point/second. The results show that the sensor array technology can “measure” the conductor currents well, especially the fundamental frequency components.

Figure 2.22 shows the 3rd harmonic currents comparison from the sensor and the CT devices (same resolution at 1 point/second). The third order harmonic currents are generally acceptable when they have higher magnitudes.

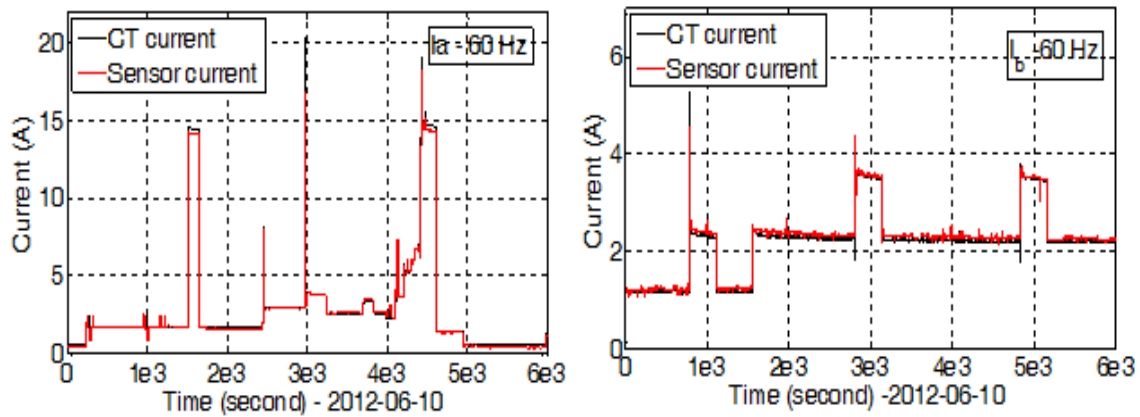


Figure 2.21: Lab experiment results showing fundamental component performance.

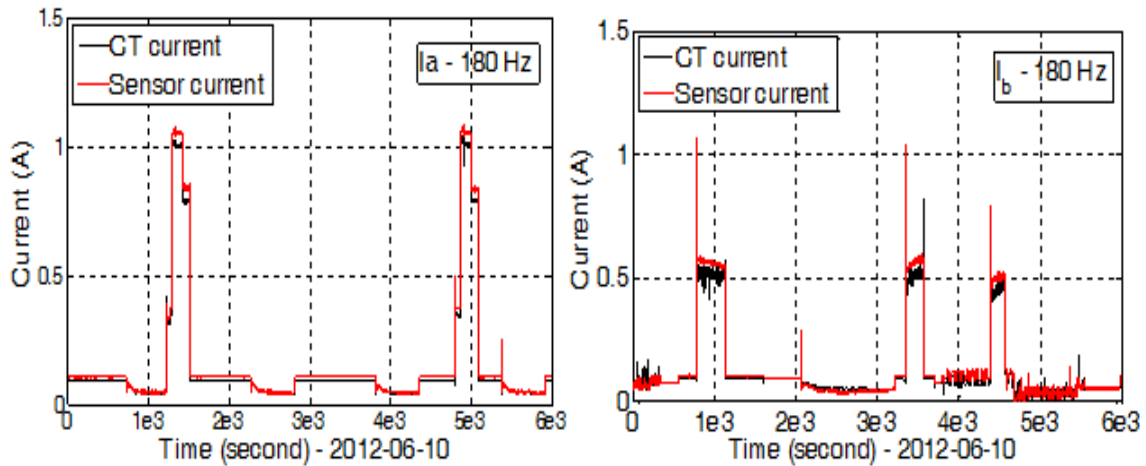


Figure 2.22: Lab experiment results showing third order harmonic performance.

2.5.2 Filed Test Results in Real Homes

Field tests of the technology have been implemented in over 10 residential homes. Each test has been run typically for a few days to weeks. Two representative installations (one indoor and one outdoor) are shown in Figure 2.23. The installations were completed by the house owners without the help from the researchers. According to the users' feedback, the average time for the installation, calibration and internet connection is approximately 15 minutes.

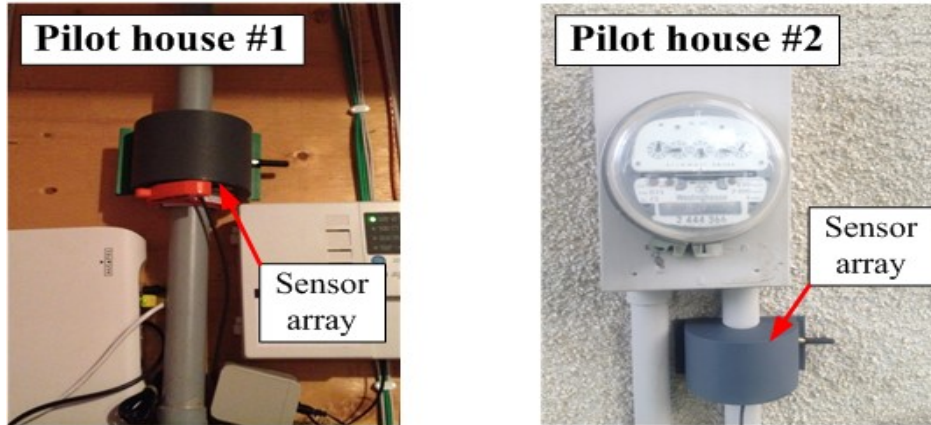


Figure 2.23: Field test installations in two pilot residential houses.

Sample test results of the above two houses are presented in Figure 2.24 and Figure 2.25. They are compared with the CT results. Long-time monitoring reveals that the power error is around 30W~120W, depending on the real-time load level. The energy estimation error is less than 3%.

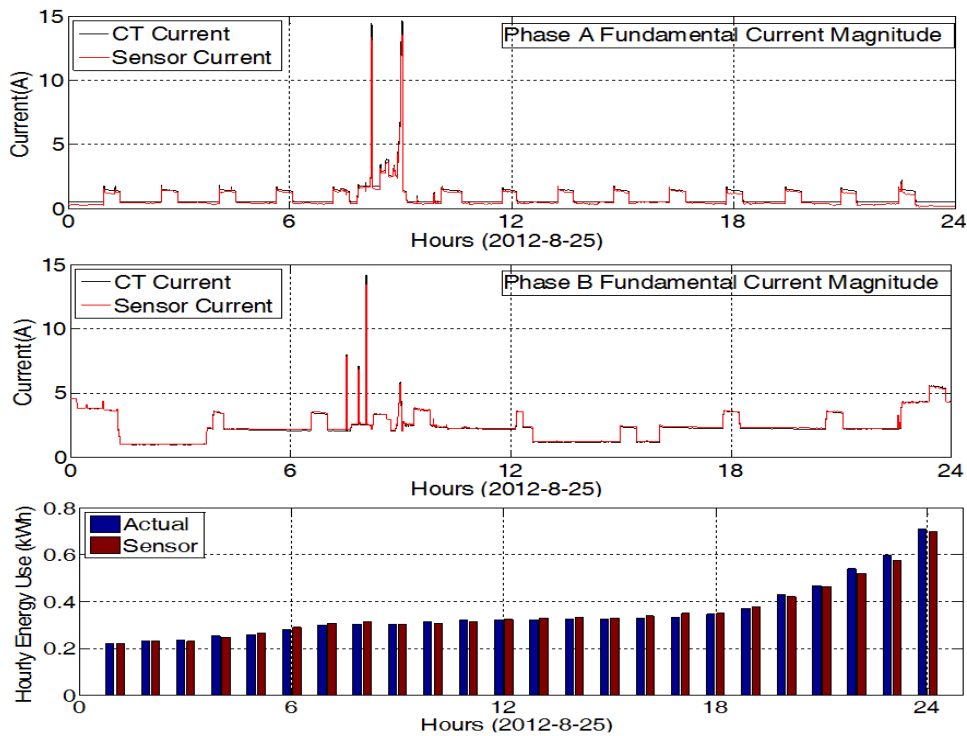


Figure 2.24: One day of real life measurement in test house #1.

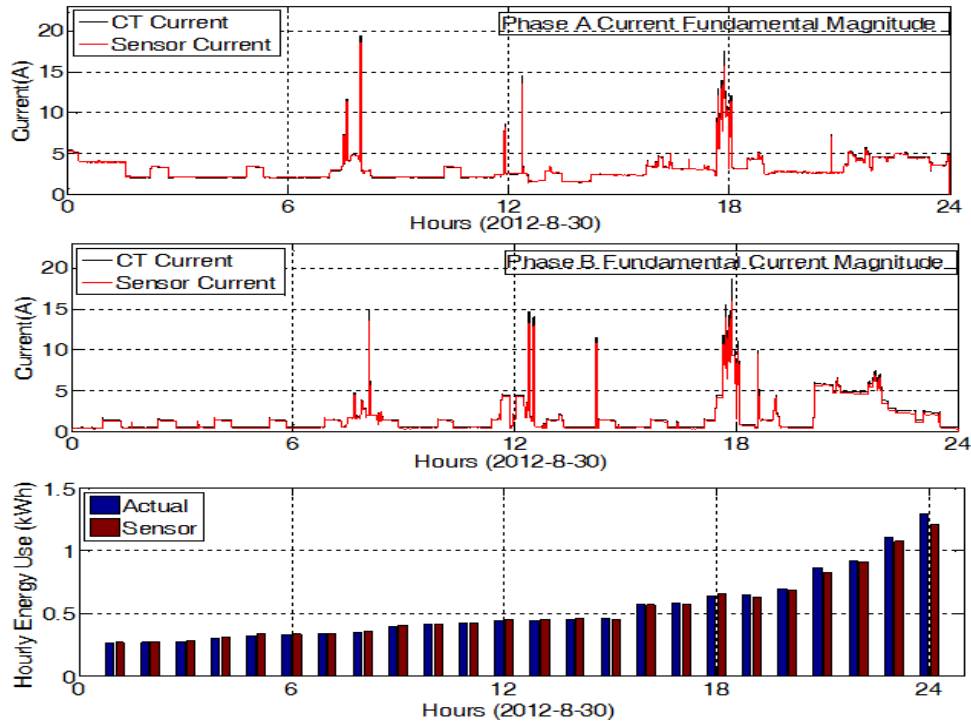


Figure 2.25: One day of real life measurement in test house #2.

To quantify the measurement error of the proposed system, the ‘error band’ characterized by the bias (μ) and standard deviation (σ) are determined (as can be seen in Figure 2.26) [66]. The results for the 60Hz current are reported in Table 2.2. It is observed that the major error of bias (μ) is contributed by the light load situations, i.e., the current level less than 1A. This error is mainly due to the weak magnetic field. Fortunately, the standard deviation (σ) for both phases is independent of the current level and remained at around 50mA for both phase A and phase B. Overall, it is very promising that the fundamental current error is within 5% for the loading above 1A.

It can be seen from the results above that the prototype sensor array technology has a satisfactory performance when measuring currents above 1A, which is sufficient for home energy use tracking (not for billing). The main problem encountered in the field is the magnetic field interference. Research is ongoing to address this issue. Solutions under investigation include shielding and adding more sensors. Additional research or tests are

needed to confirm the long-term performance of the scheme under various temperature conditions.

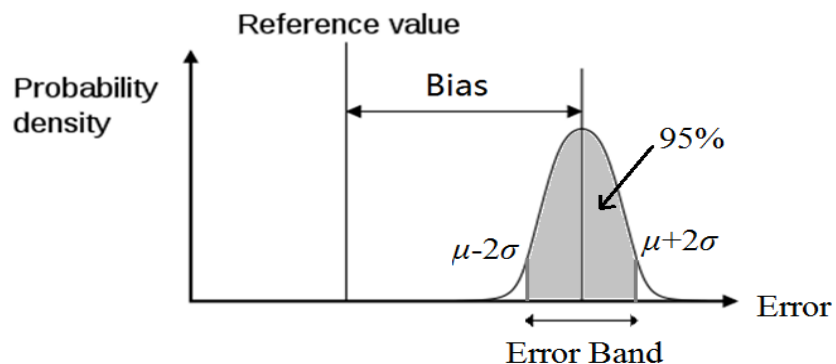


Figure 2.26: The error band definition [66].

Table 2.1: Current measurement accuracy categorized in Ampere groups.

Current Level (A)		μ (A)	σ (A)	$\mu \pm 2\sigma$ (%)
House #1	0 - 1	-0.282	0.062	-51.5 \pm 22.6
	1 - 2.5	-0.264	0.085	-5.9 \pm 2.1
	2.5 - 5	-0.260	0.031	-3.8 \pm 1.9
	5 - 10	-0.276	0.048	-4.3 \pm 1.5
	10 - 30	-0.275	0.051	-1.9 \pm 0.7
House #2	0 - 1	0.033	0.046	17.4 \pm 48.1
	1 - 2.5	0.051	0.057	3.8 \pm 4.6
	2.5 - 5	0.028	0.044	0.9 \pm 2.7
	5 - 10	0.072	0.049	1.0 \pm 1.4
	10 - 30	0.075	0.040	0.5 \pm 0.5

2.6 Summary

This chapter has presented an exclusive and attractive application using the multiple conductor current measurement technique using the active calibration scheme. It is

designed specifically for monitoring the power consumption of homes.

To better address the home energy monitoring nature in the typical North America residential homes, the adoption of the technique utilizes a simplified two-phase calibration scheme. Other contributions in this chapter focus on the development of the prototype devices, the extensive tests to verify the performance of the proposed technology, and the illustration of its application through the actual home monitoring results.

Chapter 3

Multi-Conductor Current Measurement with Known Sensor Parameters

In Chapter 2, we propose a sensor array technique to solve the multiple conductor current problems aided by an active calibration method. This technique is more suitable for the applications where the interested conductors can be accessed to allow the injections of the calibration signals. In an industrial environment where the measurement of cables is needed, it is sometimes difficult to locate the cable and connect the calibrator.

In this chapter, another magnetic sensor-array-based technique is proposed, suits especially for measuring the multi-conductor cables. The currents are computed by employing a set of magnetic sensor array measurements and computational algorithms. The sensor array is pre-calibrated by an off-line sensor calibration scheme, which is the most important idea of this research. Our experiment results using a prototype sensor array device based on the proposed measurement scheme indicate the proposed magnetic sensor array can be a solution for inferring the individual conductor current in an inaccessible bundled conductors group.

3.1 Introduction

As introduced in Chapter 2, magnetic sensor array technique addresses many multiple conductor current measurement problems with the help of the active sensor calibration method. In the actual commercial and industrial practices, we found the limitation of this scheme is that the proposed calibration cannot be conducted in the scenarios where the conductors are inaccessible. Examples shown in the second problem in Section 1.2 are generally not solvable by this technique. Also, for high voltage situation such as the overhead power lines, it is not feasible to connect a calibrator into the system to calibrate the sensors.

Therefore, another sensor-array-based technique without active sensor calibration is proposed in this research. As explained in Section 1.2, the most challenging difficulty for measuring the currents in multiple conductor cable is how to differentiate the individual conductor current from the overall magnetic field measurements. To infer the currents, the below information can be considered helpful:

- 1) The positions of the magnetic field sensors in the sensor array device.
- 2) The positions of the conductors in the cable under measurement.
- 3) The magnetic field measurements from each sensor produced by all currents.

Many existing sensor array methods assume 1) and 2) are both known (or the relative sensor-conductor positions are known). The currents are determined by inverse matrix multiplication from 3). It is obvious that these methods are not feasible to measure cable currents as the conductor positions inside the cable are unknown.

In reference [67], the authors use extensive simulations and experiments to propose a method for measuring cable currents based on the sensor-conductor relative position database. In [67], all the arbitrary but possible conductor position combinations are

simulated. The according relationships between the sensor outputs and the currents are obtained and stored in the sensor array memory unit. By using actual measurements, these relationships are tested and the errors at the sensors are obtained. The minimum error case indicates the sensor and conductor placement can be selected for this case. Thus, the relationship in this case can be used to compute currents in the future. However, this method is not sound due to the complexity of the field environment. The actual cable configurations are various and often are unknown in the field.

Reference [68] proposes a portable device for multiple conductor cable current measurement. It solves the conductor positions using the known sensor positions inversely. The performance for the conductor position reconstruction and the accuracy of the current measurement are not thoroughly examined due to the lack of technical details. The feasibility and reliability of this method are therefore unknown. Furthermore, reference [68] proposes a closed-loop measurement scheme by wrapping around the entire cable to solve the individual current. This is usually difficult to employ considering the practical limitation of the space and the bundled cables.

This chapter presents our research for multiple conductor current measurement based on the magnetic sensor array with known sensor positions. The problem is formulated in 4.2 and the detailed implementation procedures are explained in 4.3. Extensive lab tests as shown in 4.4 are conducted to verify the proposed sensor array technique. The conclusion drawn so far is summarized in 4.5.

3.2 Problem Formulation

To better demonstrate the proposed measurement methodology in this research, we still consider the most common situation involving three conductors. This is commonly seen in three-phased power transferring cables. The three conductors are usually enclosed, or contained in a bundle, with a solid insulation layer. One representing example for three

conductors in the electrical cables. It seems that we can possibly calculate the conductor current by measuring the magnetic field it produced due to the linear relationship between the currents and the magnetic fields. However, for the actual implementation, it should be noticed that there are more practical complexities to formulate this problem:

- 1) Considering the total magnetic field at the sensor location is a vector summation from all conductor current inductions, the field strength surrounding the electrical cable can be very weak. Our experience shows the magnetic field can be approximately from several to several tens milli-Gauss. To still achieve sufficient magnetic field measurement sensitivity, the single measurement axis magnetic field sensors such as the pick-up coil are normally used (two-axis or even three-axis sensors are usually not sensitive enough to be able to measure the magnetic field in this application). As a result, other than the complete field vector, only partial of its projection on the sensor axis is available.
- 2) In addition, the sensor output is typically an induced voltage signal proportional to the field magnitude, and this induced voltage is then amplified by the followed processing circuit to a detectable voltage level to feed to an analog-to-digital converter. In all the signal processing chain, we still need to quantify the total signal gain and the phase shift to infer the magnetic field strength.

3.2.1 Modeling of Single-Conductor and Single-Sensor System

There is usually the fact that most of the magnetic sensor has one specific measurement direction, i.e., the sensors are only capable to quantify the magnetic field vector projection onto this axis. Figure 3.1 shows the model of single conductor and single sensor in a Cartesian coordinate system with its origin at point O .

The magnetic sensors are in a plane where the conductor is in perpendicular to this plane so

as the magnetic field generated by the current has x and y components only. The sensor is located at a sensing point S_l and the conductor's cross section area is neglected and it modeled as an ideal long straight line in perpendicular to the sensing plane with the cross point at A .

We define:

- The sensing point coordinate is (p_l, q_l) .
- The conductor projection on the sensing plane is located at (x_a, y_a) .
- The sensor measurement direction is along the M -axis.
- The tangent direction at the point S_l is along the T -axis.
- The actual magnetic field generated by the conductor current is along the B -axis.
- The angle between the sensor measurement direction (M -axis) and the tangent direction (T -axis) at the point S_l as θ_l .
- The angle between the actual magnetic field direction (B -axis) generated by the current and the sensor measurement direction (M -axis) at the point S_l as θ_a .

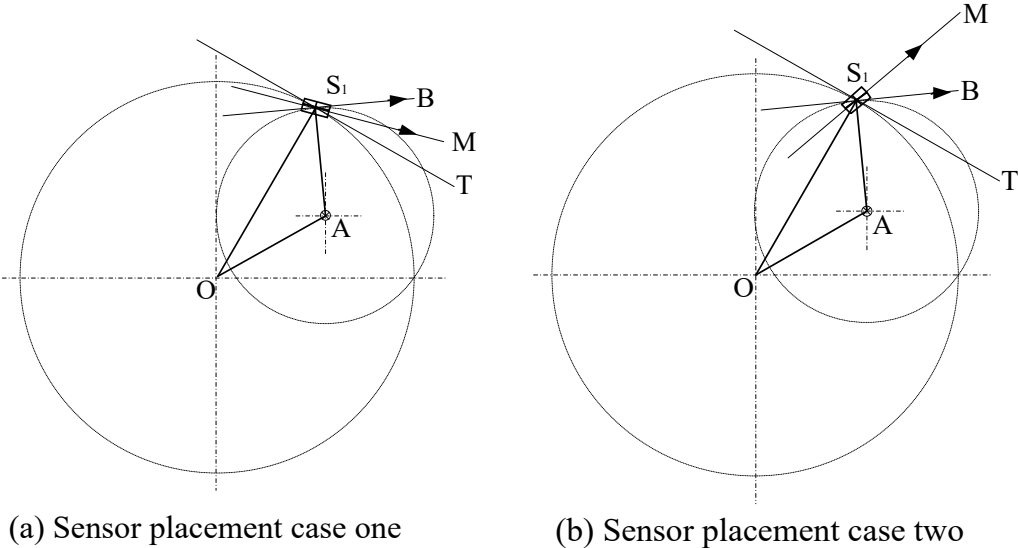


Figure 3.1: Modeling of the one sensor and single conductor configuration.

Figure 3.1 (a) presents one situation that the actual magnetic field direction is at one side of the sensing direction and also the tangent line direction. For this type of sensor/ conductor placement, we have

- $\angle OST = \pi/2$
- $\angle ASB = \pi/2$
- $\angle OSA = \angle TSB = \delta$, and finally
- $\theta_1 + \theta_a = \delta$

Figure 3.1 (b) presents another situation that the actual magnetic field direction is within the sensing direction and the tangent line direction. For this type of sensor/ conductor placement, we again have

- $\angle OST = \pi/2$
- $\angle ASB = \pi/2$
- $\angle OSA = \angle TSB = \delta$, and finally
- $\theta_a = \theta_1 - \delta$

Based on the basic geometry knowledge, we can derive the relationship of these angles as:

$$\cos \theta_a = \cos(\theta_1 - \delta) = \cos \theta_1 \cos \delta + \sin \theta_1 \sin \delta \quad (2.1)$$

where $\sin \delta$ and $\cos \delta$ are shown to help the derivation, and can be expressed according the the Cosine Law from the coordinates as:

$$\sin \delta = \frac{q_1 x_a - p_1 y_a}{\sqrt{p_1^2 + q_1^2} \sqrt{(x_a - p_1)^2 + (y_a - q_1)^2}} \quad (2.2)$$

$$\cos \delta = \frac{p_1^2 + q_1^2 - p_1 x_a - q_1 y_a}{\sqrt{p_1^2 + q_1^2} \sqrt{(x_a - p_1)^2 + (y_a - q_1)^2}} \quad (2.3)$$

Substituting Equation (3.2) and (3.3) into Equation (3.1) yields

$$\cos \theta_a = \frac{(q_1 \sin \theta_1 - p_1 \cos \theta_1)x_a - (q_1 \cos \theta_1 + p_1 \sin \theta_1)y_a + (p_1^2 + q_1^2) \cos \theta_1}{\sqrt{p_1^2 + q_1^2} \sqrt{(x_a - p_1)^2 + (y_a - q_1)^2}} \quad (2.4)$$

The magnetic field \vec{D}_a generated by the conductor current \vec{i}_a is along the B -axis and is represented according the Biot-Savart's Law as

$$\vec{D}_a = \frac{1}{2\pi D_{A-S}} \cdot \vec{i}_a = \frac{1}{2\pi \sqrt{(x_a - p_1)^2 + (y_a - q_1)^2}} \cdot \vec{i}_a \quad (2.5)$$

where D_{A-S} is the distance from point A to point S .

The sensor located at the sensing point S is only capable to measure the magnetic field flux density's projection on it measurement direction, i.e., the projection of \vec{D}_a onto the M -axis is detectable. According Figure 3.1,

$$\vec{D}_s = \vec{D}_a \cdot \cos \sigma_a \quad (2.6)$$

Equation (3.5) and (3.6) indicate that the sensor measurement can be reformatted as

$$\vec{D}_s = \frac{1}{2\pi \sqrt{(x_a - p_1)^2 + (y_a - q_1)^2}} \cdot \cos \sigma_a \cdot \vec{i}_a \quad (2.7)$$

By organizing Equation (3.4) to (3.7) together, the expression of the sensed quantity for the sensor sitting at the point S can be re-written as the follows. It contains only the sensor information from the sensor position and the sensor orientation.

$$\vec{D}_s = \frac{1}{r_1} \cdot \frac{1}{\sqrt{(x_a - p_1)^2 + (y_a - q_1)^2}} \cdot \vec{i}_a \quad (2.8)$$

where the coefficients m_1 , n_1 , and r_1 are defined as the follows.

$$\begin{cases} m_1 = \frac{\mu_0 (q_1 \sin \theta_1 - p_1 \cos \theta_1)}{2\pi} \\ n_1 = \frac{-\mu_0 (q_1 \cos \theta_1 + p_1 \sin \theta_1)}{2\pi} \\ r_1 = \sqrt{p_1^2 + q_1^2} \end{cases}$$

Equation (3.8) indicates the relationship between sensor output and the conductor current. If the sensor positions and orientation (p_1, q_1, θ_1) , and the conductor positions (x_a, y_a) are all known, it is possible to reversely derive the conductor current. This is in fact the basic principle for many sensor array measurement approaches.

However, in many cases, it is difficult to obtain all these parameters. Especially for the conductor as described in Section 1.2, their positions are not available. The conductor current cannot be solved, e.g. one sensor measurement \vec{D}_s is insufficient to solve the single conductor current \vec{i}_a since the unknowns will exceed the equation quantity. Adding more sensors to increase the number of the established equations similar as (3.8) will not help to solve this problem in this case, since more sensors will introduce even more unknown parameters. As a result, to make the multiple conductor current measurement problem solvable, the sensor parameters must be obtained beforehand.

By checking Equation (3.8), to determine the single conductor current, three equations would be necessary to solve the three unknown parameters $x_a, y_a,$ and \vec{i}_a , meaning a magnetic sensor array comprised of three magnetic sensors are required to produce adequate independent equations.

3.2.2 Modeling of Three-Conductor and Sensor Array System

According the superposition theory, a system containing three conductors and multiple magnetic sensors nearby in an array configuration can be derived from the model of the

single-conductor single-sensor system. When it comes to a set of data containing the sensor parameters and measurements, the conductor positions and currents, where the sensor measurements (Magnetic field flux densities) and the currents are instantaneous and simultaneous values (this can be achieved with synchronized waveform recording on the sensor outputs and the currents, and capture one simultaneous snapshot from all channels), it is understood that 9 unknown variables are under determination associated with three conductors: the positions and the currents.

It is possible to solve three conductor currents using a sensor array consisting of 9 independent magnetic sensors. However, it should be noticed that due to the inherent characteristic of quadratic equation, multiple solutions may exist for Equation (3.8). Further adding more extra sensors to create a non-square over-determined equation set is a possible way to overcome this problem.

In this research, 10 magnetic sensors are deployed considering the advantage of adding redundant sensors for filtering out unreasonable solutions without increasing too much data burden. Field test validations have proved that acceptable results are obtained using 10 sensors. More sensors may offer more opportunities to select the data with superior quality. The mathematical formulation of this three-conductor ten-sensor problem is therefore reformatted to how to solve an equation group that is composed of 10 nonlinear equations with 9 unknown variables.

The unknown variables are the three conductor currents, denoted as (x_1, x_2, x_3) , and six conductor coordinates, represented as $(x_4, x_5, x_6, x_7, x_8, x_9)$, where (x_1, x_4, x_5) is associated with one conductor and so on. The computation can be conducted either in time domain to re-construct the current waveform, or in the frequency domain to infer the current phasors.

The computation proposed in this research is fulfilled according the superposition theory and is established as the equation set in (3.9). Note that Equation (3.9) and (3.10) contain

only the instaneous values for demonstration, the actual implementation for a three-phased cable current measurement requires to infer the current magnitude and phase.

$$\begin{cases} F_1(X) = 0 \\ F_2(X) = 0 \\ \dots \\ F_{10}(X) = 0 \end{cases}, X = [x_1 \ x_2 \ x_3 \ x_4 \ x_5 \ x_6 \ x_7 \ x_8 \ x_9] \quad (2.9)$$

where

$$\begin{aligned} F_i(X) = & \\ & x_1 [m_i(x_4 - p_i) + n_i(x_5 - q_i)] [(x_6 - p_i)^2 + (x_7 - q_i)^2] [(x_8 - p_i)^2 + (x_9 - q_i)^2] + \\ & x_2 [m_i(x_6 - p_i) + n_i(x_7 - q_i)] [(x_4 - p_i)^2 + (x_5 - q_i)^2] [(x_8 - p_i)^2 + (x_9 - q_i)^2] + \\ & x_3 [m_i(x_8 - p_i) + n_i(x_9 - q_i)] [(x_4 - p_i)^2 + (x_5 - q_i)^2] [(x_6 - p_i)^2 + (x_7 - q_i)^2] - \\ & B_i r_i [(x_4 - p_i)^2 + (x_5 - q_i)^2] [(x_6 - p_i)^2 + (x_7 - q_i)^2] [(x_8 - p_i)^2 + (x_9 - q_i)^2] \end{aligned} \quad (2.10)$$

and

$$\begin{cases} m_i = \frac{\mu_0 (q_i \sin \theta_i - p_i \cos \theta_i)}{2\pi} \\ n_i = \frac{-\mu_0 (q_i \cos \theta_i + p_i \sin \theta_i)}{2\pi}, i = 1, 2, \dots, 10 \\ r_i = \sqrt{p_i^2 + q_i^2} \end{cases}$$

B_i is the magnetic flux density by the magnetic sensor S_i in response to three conductor currents at certain time, it contains the superposed contributions from current x_1, x_2 and x_3 . (p_i, q_i, θ_i) are the position and the orientation of the sensor S_i , which are the key to compute the conductor side variables. Here m_i, n_i, r_i, p_i, q_i are known as they are all derived by the model of the sensor parameters.

3.3 Proposed Current Measurement Scheme

The proposed current measurement scheme in this research can be decomposed into three stages:

1) Off-line sensor parameters calibration stage

The sensor parameters including each sensor's position coordinates, sensing orientations, output gain and circuit phase shift will be determined by a off-line calibration scheme.

2) Conductor position computation stage.

Once the sensor parameters are obtained from 1), this multiple conductor current computation problem is re-formatted and becomes solvable. One set of solutions contain the currents at that moment and most importantly, the conductor positions that are used to derive the sensor output-current relationship.

3) Real-time current measurement stage.

Numeric algorithms used to determine the conductor positions in stage 2 is generally cost-expensive regarding the time consuming and computation power. Once the stage 1 and 2 are completed, this problem is again simplified and can be further formulated to the model with the known sensor-conductor geometry. The conductor current can be easily computed in real-time from the matrix multiply of the sensor outputs and the geometry coefficients.

3.3.1 Determining the Sensor Parameters

Accurate sensor parameters are essential to solve Equation (3.9). It seems possible to use the ideal design values when the sensor array is constructed. However, such parameters are usually inaccurate as the sensors deviate easily from the ideal position in the manufacturing process, and the sensor signal processing circuits have their tolerance range. Our studies

have revealed that significant measurement errors can be found when simply using the ideal sensor parameters in the computation.

As introduced in Section 3.2, the magnetic field flux density at the sensing point is usually weak and needs to be processed by the analog sensor conditioning circuit, introducing an amplify gain from the amplitude of \vec{B}_s to the final sensor circuit output voltage \vec{V}_s . In addition, unavoidable phase shift coming from the analog circuit due to the noise filtering and the operational amplifier phase shift are expected. These two factors (gain g and phase shift φ) may be estimated from the design, however, due to the tolerance of the passive components (resistor, capacitor, inductor, etc. can have as large as 10% tolerance of their nominal values), they are also considered as the unknowns on the sensor side. We therefore have

$$\vec{V}_s = g_1 \cdot e^{-j\varphi_1} \cdot \vec{B}_s = J(x_a, y_a, p_1, q_1, \theta_1, g_1, \varphi_1, \vec{I}_a) \quad (2.11)$$

Equation (3.11) indicates the relationship between sensor output and the conductor current. If the sensor circuit parameters (g_1, φ_1), sensor positions and orientation (p_1, q_1, θ_1), and the conductor positions (x_a, y_a) are all known, it is possible to reversely derive the conductor current. This is in fact the basic principle for many sensor array measurement approaches.

In this research, the sensor positions, orientations, amplify gains and the phase shifts from their analog processing circuits are made known from an off-line calibration scheme. Specifically, the proposed sensor array calibration scheme will quantify the values of $(p_i, q_i, \theta_i, g_i, \varphi_i)$ for each sensor S_i . This is achieved by comparing a set of synchronized known calibration currents and the sensor outputs in response. The pre-determined calibration currents flow through a set of long straight conductors, e.g. conductor a, b, c, d , which are perpendicular to the sensing plane. The conductor positions in respect to the origin of the sensing plane are as known with high accuracy with a specially design mechanical structure as can be seen in Figure 3.2.

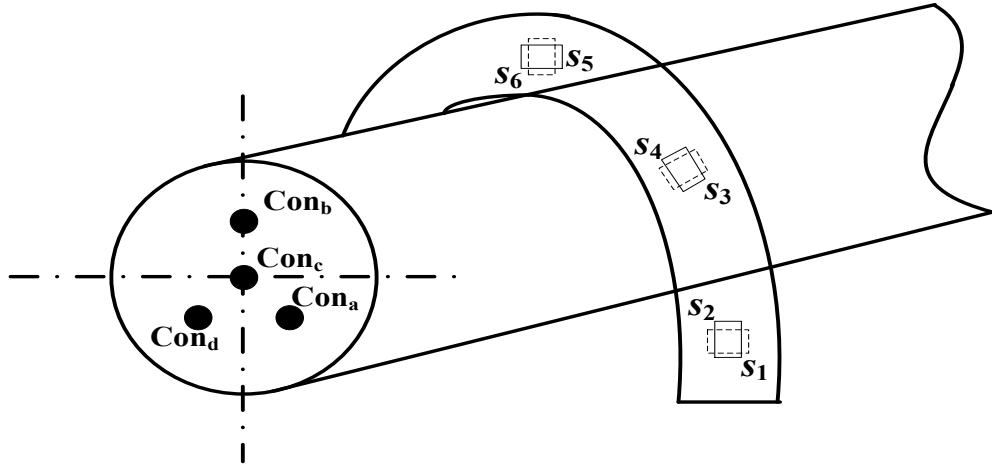


Figure 3.2: Sensor array deployment.

The sensor array is deployed nearby these conductors. By energizing the conductors with a series of specifically known currents, namely the calibration current, simultaneous sensor outputs in response to the calibration currents are recorded as well as the currents. Only one conductor is energized each time, making a single calibration event. As we have mentioned in Section 3.2, since four parameters for each individual sensor (p_i, q_i, θ_i, g_i) are under determining (the phase shift φ can be determined in any event by comparing the current and the sensor output phase angles), the calibration process containing four events will be sufficient to calculate the sensor array parameters.

For the implementation, the sensors are mounted on a measurement plate made of PVC (shown in Figure 3.2). Five PVC sensor holders are screwed on the plate; on each sensor holder two perpendicular holds are drilled to accommodate two sensors (as seen in Figure 3.3), this saves a lot of space for placing sensors, greatly benefits the device miniature. The sensor holder can rotate, allowing the sensor measurement directions to be adjusted. Ten magnetic sensors outputs can be sampled simultaneously and recorded by the data acquisition instrument for analysis.

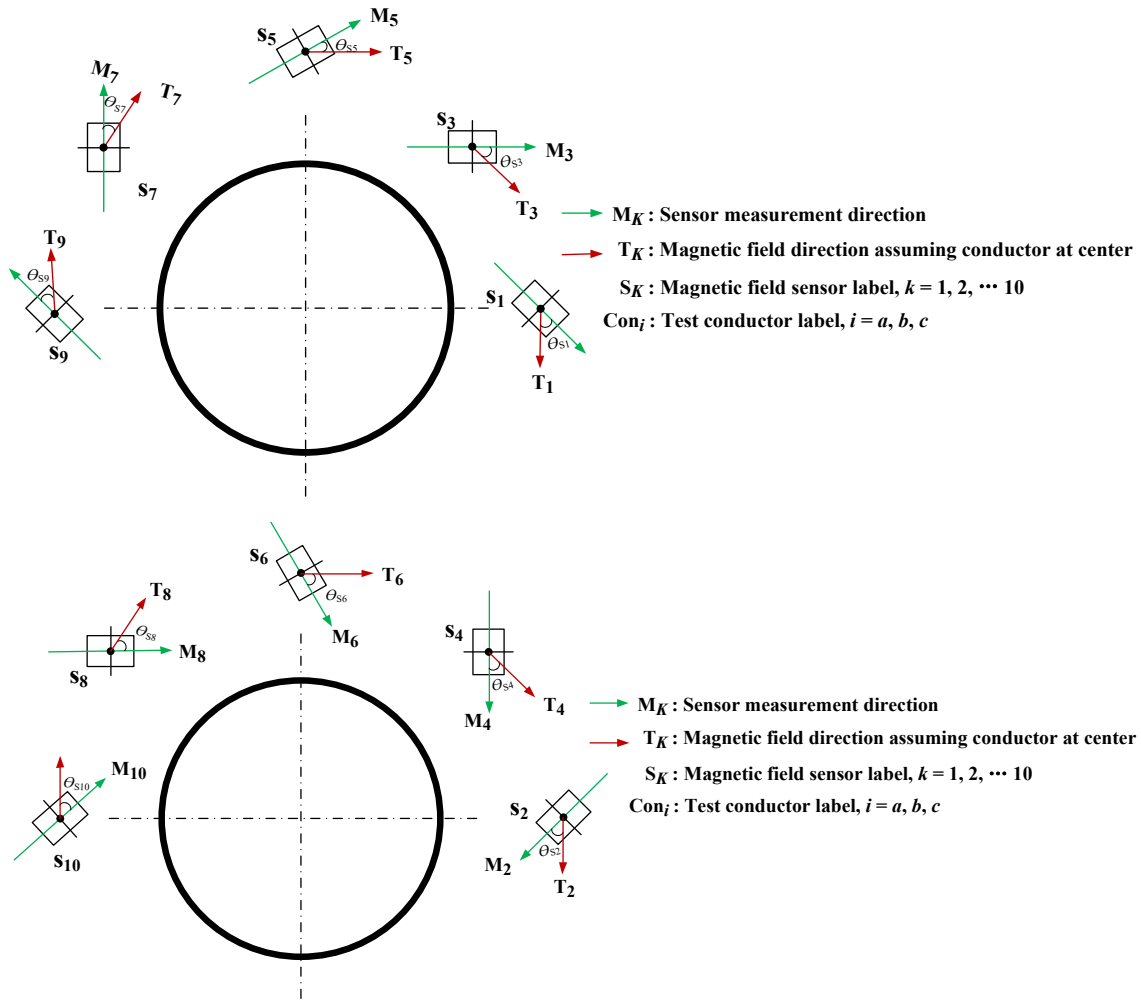


Figure 3.3: Layout of magnetic sensor array in the experiments.

Among these sensors, five of them ($S_1 \sim S_5$) are categorized into one group, the other five ($S_6 \sim S_{10}$) are in the other group. If we again establish a Cartesian coordinate system with the origin at the center of the conduit, the sensor S_i and S_{i+5} , $i=1, 2, \dots, 5$ have almost same coordinates but different measurement directions. When conducting the sensor array calibration, the following assumptions apply:

- Sensors have single measurement axis and can only measure the magnetic field flux line perpendicularly penetrates the sensing plane.

- The sensor size is small enough, so the magnetic flux lines sensed at the sensing plate of the sensor is assumed identical and can be concentrated as a sensing point in space.
- The relative positions between conductors and sensor array are unchanged during the entire calibration.
- There is no external interference AC magnetic field.

These assumptions are generally sound. A preferred conductor energization sequence of *Cona-Conb-Conc-Cond* to calibrate the proposed sensor array is shown in Figure 3.4.

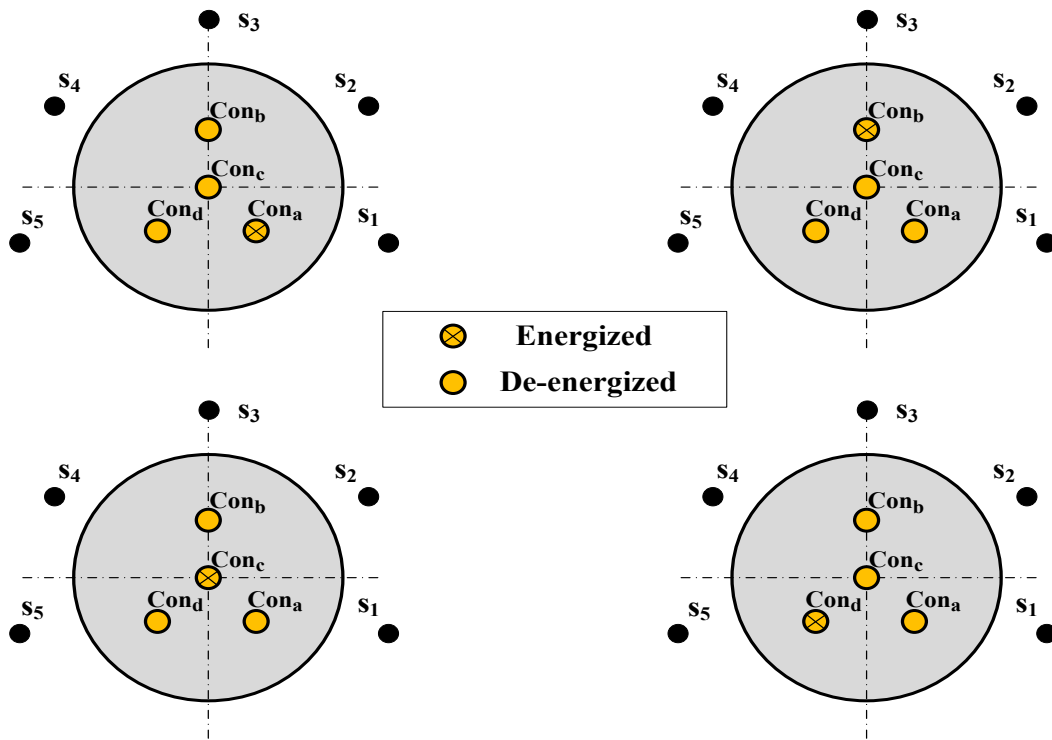


Figure 3.4: Conductors energizing sequence.

The conductor current used for sensor calibration is defined as \vec{i}_a , \vec{i}_b , \vec{i}_c and \vec{i}_d . The output of sensor S_i when only conductor a is energized in response to current \vec{i}_a is defined as $\vec{V}_{i,a}$, where $\vec{V}_{i,a} = \vec{D}_{i,a} \cdot \vec{g}_i \cdot e^{-\dots}$. Define the rest three calibration events following by the

calibration on the conductor a , we will have

$$\begin{cases} G_1(p_i, q_i, \theta_i) = 0 \\ G_2(p_i, q_i, \theta_i) = 0 \\ G_3(p_i, q_i, \theta_i) = 0 \\ G_4(p_i, q_i, \theta_i) = 0 \end{cases} \quad (2.12)$$

where

$$\begin{aligned} G_i(p_i, q_i, \theta_i) = \\ I_j \cdot [u_1(x_j - p_i) + v_1(y_j - q_i)] - B_{i,j} \cdot g_i \cdot r_i [(x_j - p_i)^2 + (y_j - q_i)^2] \end{aligned} \quad (2.13)$$

$i = 1, 2, \dots, 10$ and $j = a, b, c, d$

$$\begin{cases} u_i = \frac{\mu_0 (q_i \sin \theta_i - p_i \cos \theta_i)}{2\pi} \\ v_i = \frac{-\mu_0 (q_i \cos \theta_i + p_i \sin \theta_i)}{2\pi} \\ r_i = \sqrt{p_i^2 + q_i^2} \end{cases}$$

$B_{i,j}$ is the magnetic flux density obtained by the magnetic sensor S_i in response to four calibration currents, one current at one time in one equation. $(p_i, q_i, \theta_i, g_i)$ are the unknown sensor information to be solved of the sensor S_i . Here m_i, n_i, r_i , are also known. The sensor information is in the form of real numbers as they are all derived by the model of the relative conductor-sensor geometry.

Solving Equation (3.12) is much easier than Equation (3.9) due to it is lower dimension and less unknown variables $(p_i, q_i, \theta_i, g_i)$. Actually, by adjusting the phase shift θ_i from the sensor output, the equation set (3.13) consist of only real numbers. Iteration based algorithms, such as the simple Newton-Raphson method, Gradient method and more recently the Levenberg–Marquardt (for the non-square equation set with redundant information, e.g. utilizing more calibration conductor current such as five or more to infer the four unknown sensor variables for each sensor) and the Trust Region method

(preferable for solving the square equation set as formulated above) [69]-[71] are possible to solve this problem.

In this section, the computation running by the Trust Region method is realized in MATLAB. The computation process is simple and consumes only little time, it only runs one computation cycle in solving the equation set described in (3.12) for one sensor. An adaptive converging tolerance is 1‰ of the amplitude of $\vec{v}_{i,j}$ to accelerate the computation and increase the successful chance of the convergence (this is a more meaningful converge judgement threshold since a smaller tolerance, in this practical problem, is even smaller than the ADC resolution). The initial values of $(p_i, q_i, \theta_i, g_i)$ is needed to initialize the first run of the Trust Region method iteration. Fortunately, the initial values are available by utilizing the mechanical design parameters of the sensor array.

Table 3.1: Sensor information obtained from computation

Sensor No.	p_i (mm)		q_i (mm)		θ_i (degree)		g_i	
	<i>Ref.</i>	<i>Cal.</i>	<i>Ref.</i>	<i>Cal.</i>	<i>Ref.</i>	<i>Cal.</i>	<i>Ref.</i>	<i>Cal.</i>
1	35.00	37.78	0.00	-4.05	45.00	35.34	2.168	2.70
2	35.00	36.35	0.00	-0.83	-45.00	-47.84		2.64
3	24.75	25.93	24.75	25.78	45.00	47.88		2.17
4	24.75	23.65	24.75	26.86	-45.00	-36.27		2.39
5	0.00	1.54	35.00	35.04	45.00	48.49		2.10
6	0.00	-0.89	35.00	36.45	-45.00	-38.91		2.30
7	-24.75	-24.54	24.75	24.60	45.00	54.10		2.12
8	-24.75	-23.63	24.75	26.71	-45.00	-47.30		2.51
9	-35.00	-35.02	0.00	-1.46	45.00	55.21		2.66
10	-35.00	-28.64	0.00	1.90	-45.00	-38.76		1.64

Table 3.1 presents the sensor information obtained from the computation, the initial values,

or the ideal parameters from the sensor array design, is denoted as *Ref.* in this table. The computation results, or the actual sensor information, are denoted as *Cal.*

To better demonstrate the results, Figure 3.5 illustrated the comparison between the computed sensor coordinates and the ones retrieved from the design (positions of the sensor holder centers). It is obvious that sensor S_i and S_{i+1} have non-negligible position deviations. Their measurement direction difference between sensor S_i and S_{i+1} are even more obvious, however, the angle between the two sensor axes are either more or less than 90 degrees. Therefore, without the proposed off-line sensor array calibration, significant current measurement errors, if the currents are still able to be computed, are expected.

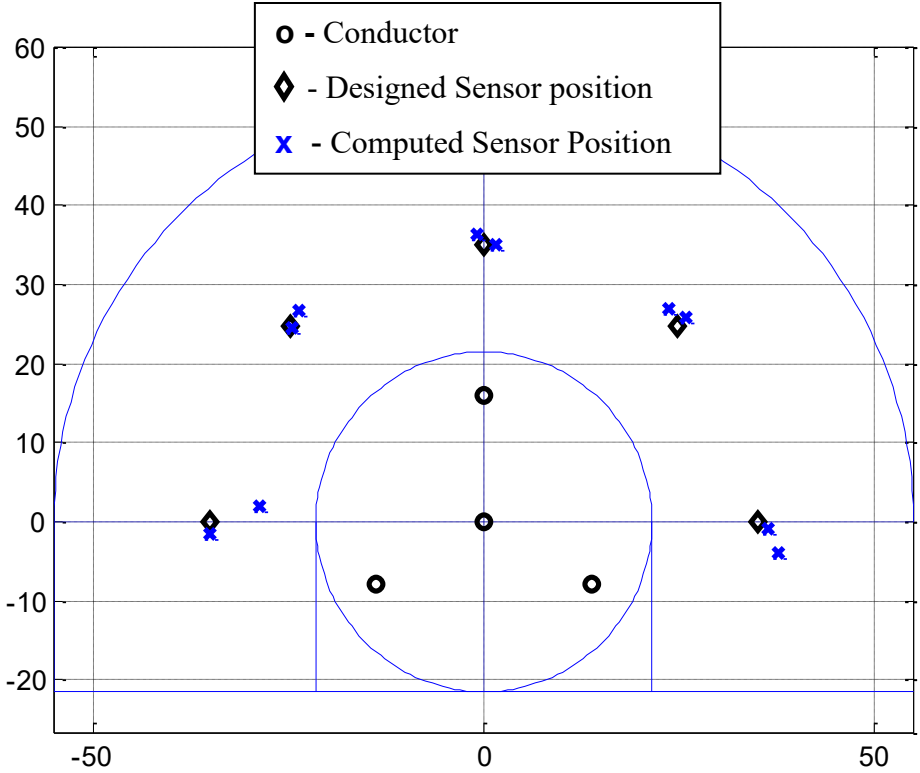


Figure 3.5: Sensor position difference from the computation and the reference.

Once the sensor array is calibrated, the sensor parameters are stored in the device flash memory. Such information is independent to the conductors under measurement and is

constant once the sensor array is constructed. Therefore, the calibration is only needed one time at the manufacturing phase. This is the normal process for typical commercial measurement equipment as the factory calibration is one important step of the Quality Assurance program.

This section establishes a square equation set as described in Equation (3.12) to calibrate the sensor array. In fact, more calibration conductor currents can be placed at different positions to assist the sensor array calibration. An attempt by using five conductors and the Levenberg-Marquardt solver in MATLAB has been tested without receiving obvious calibration accuracy improvement. Oppositely, the trade-off of such revision is the more expensive computational cost.

3.3.2 Determining the Conductor Positions

After determining the ten sensor parameters, the non-linear equation set described in (3.12) becomes solvable. There are many different numerical ways to achieve this task. Many regular iterative algorithms, such as the simple Newton-Raphson method, Gradient method and more recently the Trust Region method [70] are possible to solve this problem. However, the large dimension of this equation set can make the Newton iterations very sensitive to the initial values used to initialize the first round of the numerical computation. The iteration guesses cannot converge to the correct solution if a set of unreasonable values are far away from the real solution.

Due to the enclosed, inaccessible nature of the cable, guessing reasonable conductor initial positions can be difficult. One of our previous researches attempted to predict the possible conductor configuration by observing and comparing the signal strength among the ten-sensor output. However, a larger scale of simulations show this research direction failed to provide reliable initial value guesses, resulting in many wrong or divergent conductor parameter computation results.

Another type of computational algorithms, namely the heuristic evolutionary computation is adopted in this research. Although these algorithms are well-known for their expensive computational consumptions, their excellent performance in solving optimization problems is acknowledged. Extensive simulation evaluations using MATLAB have revealed that the Differential Evolution algorithm [72] outperforms many other peers' due to its superior performance on the converging rate and the highest accuracy [73].

For the actual implementation, the need to measure multi-conductor cable currents is very common in reality. The currents, no matter balanced or unbalanced, are usually in different phases. The currents are represented in phasors form so as the equation set (3.9) needs to be re-written with complex numbers. The three currents contain both real parts and imaginary parts, yielding the solution set in the complex number form as

$$X'_i = [x_{1R}, x_{1I}, x_{2R}, x_{2I}, x_{3R}, x_{3I}, x_4, x_5, \dots, x_9] \quad (2.14)$$

where x_{1R}, x_{2R}, x_{3R} and x_{1I}, x_{2I}, x_{3I} are real parts and imaginary parts of x_1, x_2, x_3 , respectively.

It means that the dimension of the optimization problem equals to 12 due to the increased complexity of the phasor computation. Our purpose to establish this model is to find the cable positions, it is not necessary to compute the currents at this stage. Therefore, a simplified computing procedure neglecting the searching of six currents unknowns (both real parts and imaginary parts) is used to reduce the solution dimension and accelerate the DE algorithm. The main idea herewith is to calculate the values of x_{1R}, x_{2R}, x_{3R} and x_{1I}, x_{2I}, x_{3I} based on the test values of $x_4, x_5, x_6, x_7, x_8, x_9$ at the beginning of each iteration step using any 3 equations out of the 10 equations mentioned in (3.9). (separating the equations into real and imaginary parts). In other words, once the cable positions are assumed, the cable currents can be easily calculated using a matrix multiplication. This simplification greatly improves the computation efficiency by reducing the search space

dimension of the problem from 12 to 6 (only the position of the conductors). The flowchart of the proposed algorithm determining the conductor positions is illustrated in Figure 3.6.

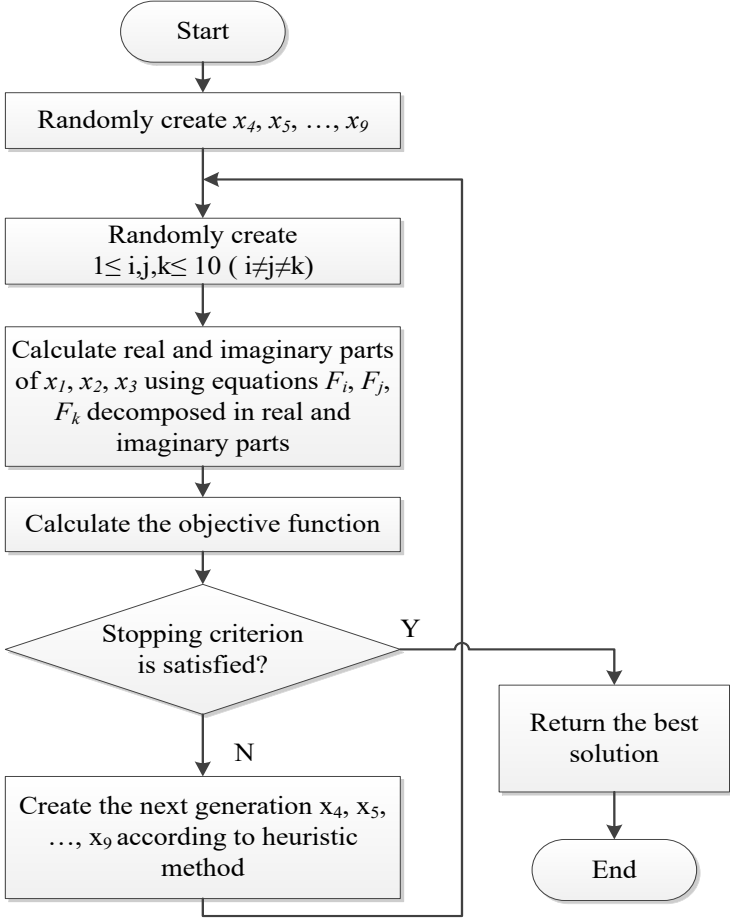


Figure 3.6: Flowchart for the conductor position computation algorithm.

The absolute value of each equation in Equation (3.9) can be considered as an error value that should be as close to zero as possible. Therefore, the objective function associated with the DE computation is introduced as the summation of these errors. The goal of applying the evolutionary algorithms is to minimize the objective function through multiple iterations.

Multiple recorded snapshots from the three phase current waveforms are utilized instead of single sample to reduce the computation errors. Each snapshot represents a set of

instantaneous values from the sensor output waveform and the current waveforms recorded simultaneously. In this way, the conductor position estimation errors of the proposed algorithm can be reduced. Extensive case studies revealed that 5 samples are appropriate to finalize the results. Further increasing of the sample numbers increases the computation time yet achieves significant improvements on the results.

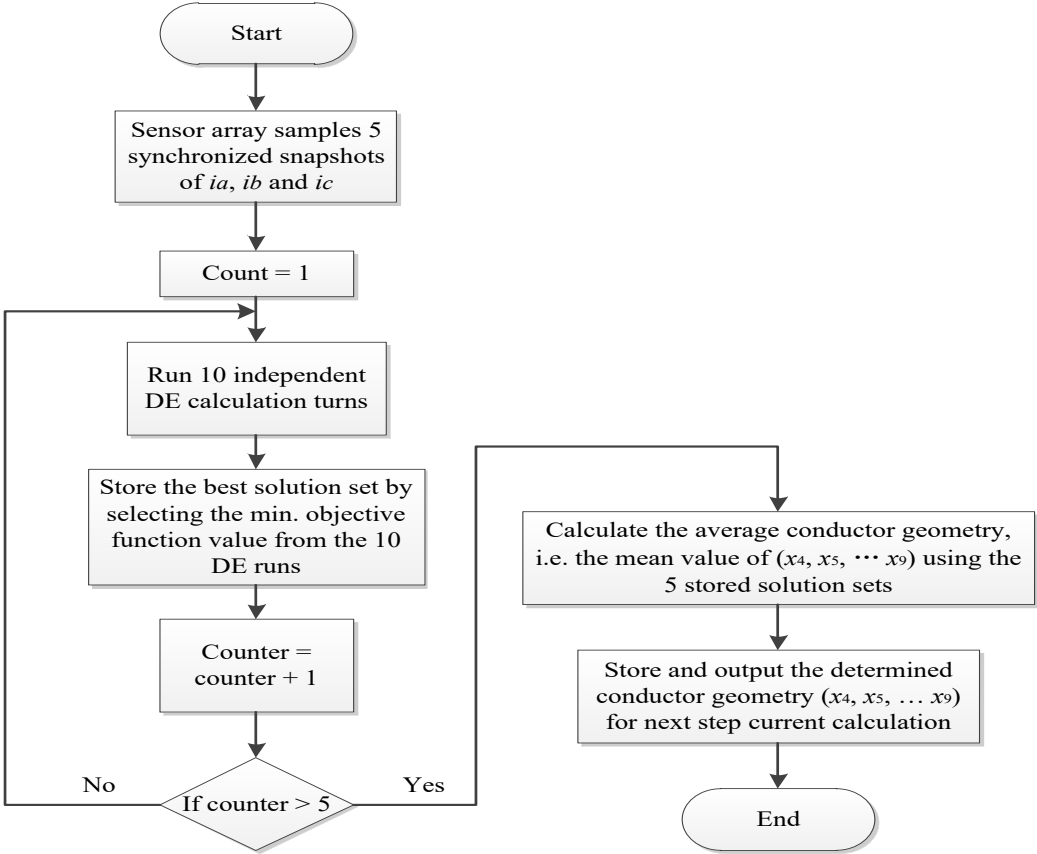


Figure 3.7: Flowchart of the process how to compute the conductor positions.

For each sample, 10 independent runs were performed with the DE algorithm. The result with the minimum objective function is considered as the best position solution for that sample. Five samples result in 5 candidate conductor position estimations. Finally, the average of these 5 candidates is adopted as the final result. The obtained position coordinates (x_4, x_5, \dots, x_9) are stored in the memory and is utilized to generate the sensor/conductor geometry relationship. The coefficient matrix describes such relationship in this

three-conductor-ten-sensor system will directly be utilized to determine the current measurement. The current computation, with the know coefficient matrix, can be achieved in real time with only little computational burden.

In summary, the conductor positions are determined in the process explained above. They are used to derive the coefficient matrix between the conductor currents and the sensor outputs as shown in the flowchart of Figure 3.7.

3.3.3 Real-time Conductor Current Measurement

Actually, for the events used to compute the conductor positions, the conductor currents (x_1, x_2, x_3) are also computed at the same time when solving the conductor positions (x_4, x_5, \dots, x_9). However, the DE algorithm used is time consuming. It is not preferable that we recall this algorithm every time to compute the conductor currents in the normal measurement stage.

One the other hand, it can be seen in Equation (3.12) and (3.13) that when the positions of the three conductors are obtained (x_4, x_5, \dots, x_9 are known), Equation (3.12) becomes a three-variable linear equation. The following equation set can be formed by selecting any three sensors.

$$\begin{cases} K_{1a}I_a + K_{1b}I_b + K_{1c}I_c = B_1 \\ K_{2a}I_a + K_{2b}I_b + K_{2c}I_c = B_2 \\ K_{3a}I_a + K_{3b}I_b + K_{3c}I_c = B_3 \end{cases} \quad (2.15)$$

where I_a, I_b, I_c are the three unknown currents, B_1, B_2, B_3 denote the magnetic flux density sensed by the selected three magnetic sensors, K_{ia}, K_{ib}, K_{ic} ($i=1, 2, 3$) are real numbers and denote the corresponding geometry parameters for the three sensors based on calculation from Equation (3.12) and (3.13). Then the three currents can be determined as

$$[\mathbf{I}]_{3 \times 1} = [\mathbf{K}]_{3 \times 3}^{-1} [\mathbf{B}]_{3 \times 1} \quad (2.16)$$

where $[B]_{3 \times 1}$ denotes the magnetic flux density sensed by the three sensors, $[I]_{3 \times 1}$ represent the AC currents flowing through the conductors, and $[K]_{3 \times 3}$ is the coefficient matrix comprising the I - B relationship.

3.4 Experiment Validations and Discussions

Comprehensive laboratory experiments have been conducted to validate the proposed current measurement method for multi-conductor cables. The practical measurement procedure is carried out in three stages: determining the sensor array parameters, determining the conductor positions and finally, the conductor current calculation. In the first stage, the numerical computation method is employed to attain the sensor array information including the ten sensor positions, orientations, amplify gains and the phase shifts. The exact positions of the conductors in the cable in afterwards computed with Differential Evolution method due to its superior performance explored in the simulation study. When the coefficient matrix is determined, the three-phase AC currents are calculated in real time in the final stage.

3.4.1 Experiment Bench Setup

An experimental bench is set up as illustrated in Figure 3.8. The sensor array is clamped on a plastic conduit that accommodates three power conductors. A three-phase voltage source supplies adjustable three-phase delta-connected resistive loads at the remote end. The values of the three-phase currents were measured by the current probes as the reference. Meanwhile, the outputs of the 10 magnetic sensors are collected by a data-acquisition system consisting of a NI-DAQ instrument and a laptop, which processes the data based on the proposed computation method.

The proposed measurement method does not require the sensor array enclosing the conductors in closed-loop, which indicates that the sensor array can be conveniently

installed. In this research, one-axis pick-up coil sensors are selected due to their low cost, high sensitivity and compact size. The AC magnetic field produced by the conductor currents induces a voltage in the coil sensor, which is processed by the designed signal conditioning circuit. It is noteworthy that other types of magnetic sensors with proper sensitivity would also work for this application. A picture showing the laboratory experiments performed to validate the effectiveness of the proposed approach on a test platform is presented below as Figure 3.9.

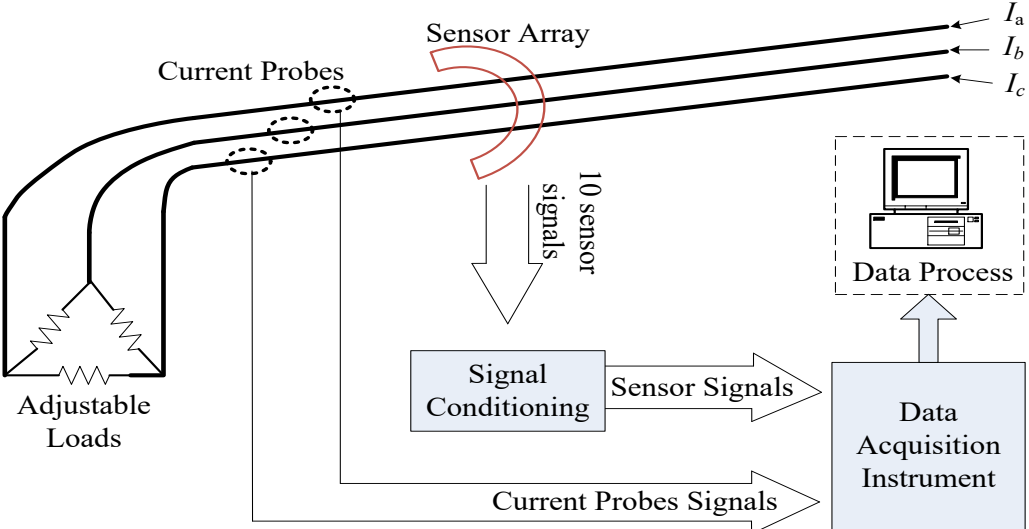


Figure 3.8: Diagram of experimental bench setup.

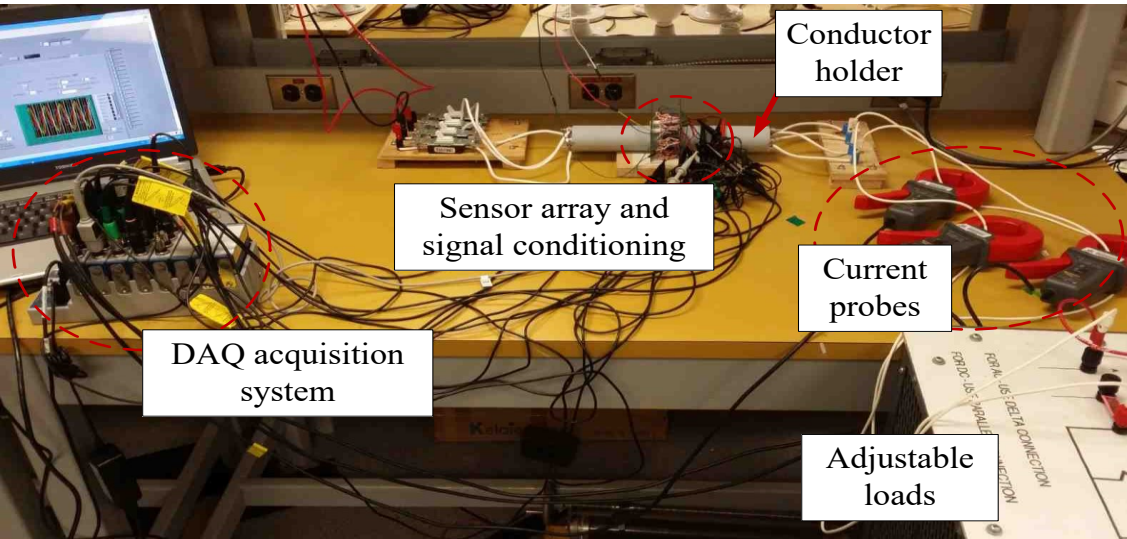


Figure 3.9: Photograph of experimental bench setup.

3.4.2 Sensor Array Calibration Results

The layout of the 10 magnetic sensors in the experiments is depicted in Figure 3.10. All the sensors are located in the same plane which is perpendicular to the axis of the cable. The position of each sensor (p_i, q_i) and its measurement axis direction are calibrated in the manufacturing process of the shown prototype by the off-line calibration scheme explained in Section 3.3.1.

To evaluate the computation results, the ten sensor output waveforms during the calibration event in response to the four conductor currents are recorded (namely the measurement); they are compared to the theoretical sensor waveforms that are plotted using Equation (3.15) by the known sensor information and the calibration currents. Here, the theoretical waveform of each sensor is obtained based on the sensor parameters listed in Table 3.1. In the calibration experiment, a single frequency current source only equipped with 60 Hz component is used to generate the calibration currents.

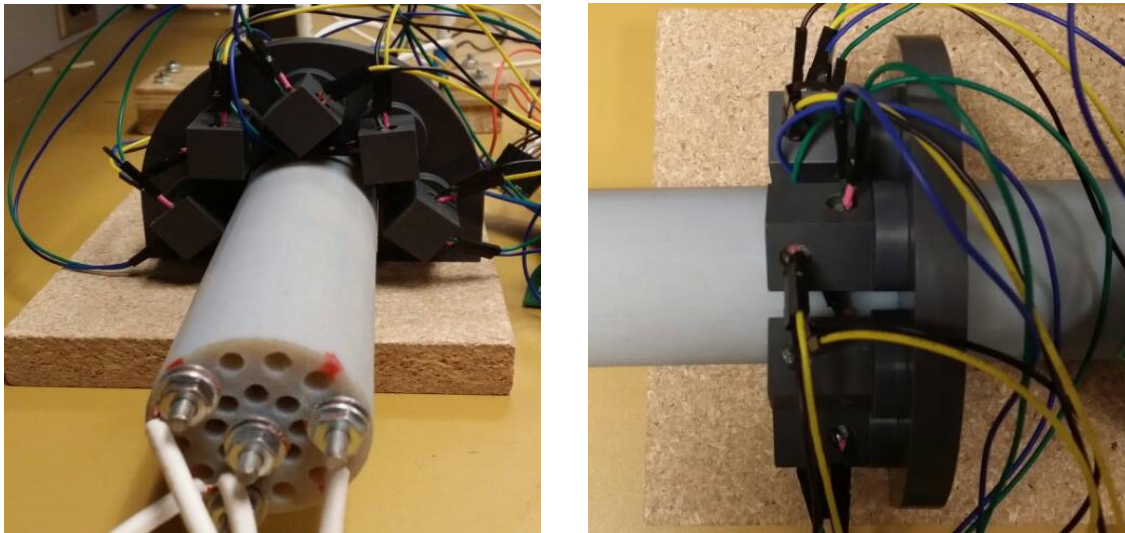


Figure 3.10: Pictures of the sensor array system.

Only the results associated with sensor S_1 are presented below, the results for the rest nine sensors are similar and are demonstrated in Appendix. In Figure 3.11, it can be seen that the

theoretical sensor waveforms (“60 Hz compute”) and the measured sensor waveforms (“60 Hz measure”) match quite well for all four calibration events (“cali 1” for conductor a energization, “cali 2” for conductor b energization, and so on).

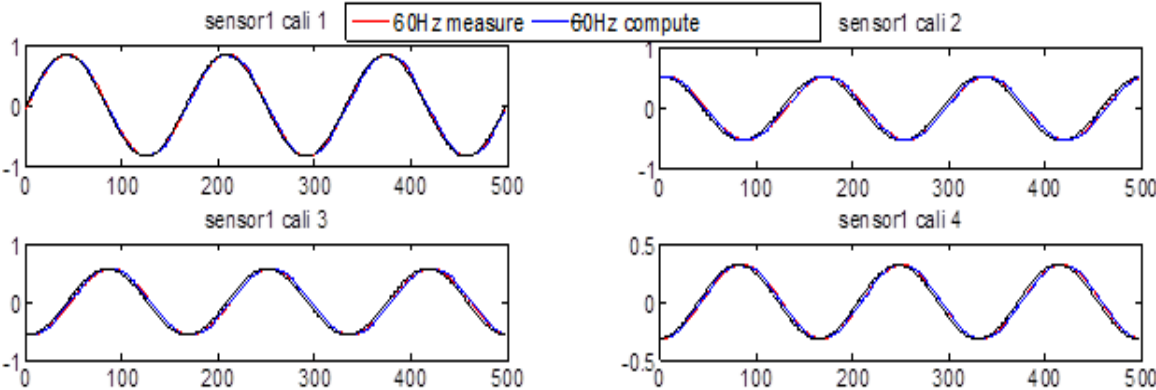


Figure 3.11: Sensor S_1 parameters calibration result evaluation.

For other sensors $S_2 - S_{10}$, consistent results with good overlapping can be found, proving the calibration algorithm is feasible to calibrate the sensor array and provide accurate sensor information for the future computations.

3.4.3 Conductor Position Computation Results

Two cases with unsymmetrical and symmetrical cables configurations as shown in Figure 3.12 are tested if the conductor positions can be identified through the proposed method. In addition, the unsymmetrical case (Figure 3.12 (a)) is rotated by 120 degrees clockwise and counterclockwise to form two additional conductor layouts. Figure 3.13 presents the actual cable positions versus the estimated results for the four cases. The computation results are found to be highly close to the actual conductor positions in the cable.

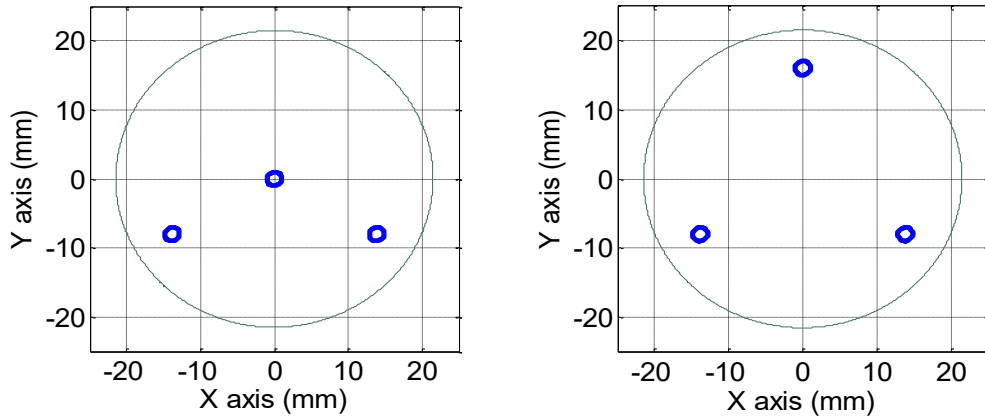


Figure 3.12: Basic cable configurations: Left - unsymmetrical, Right - symmetrical.

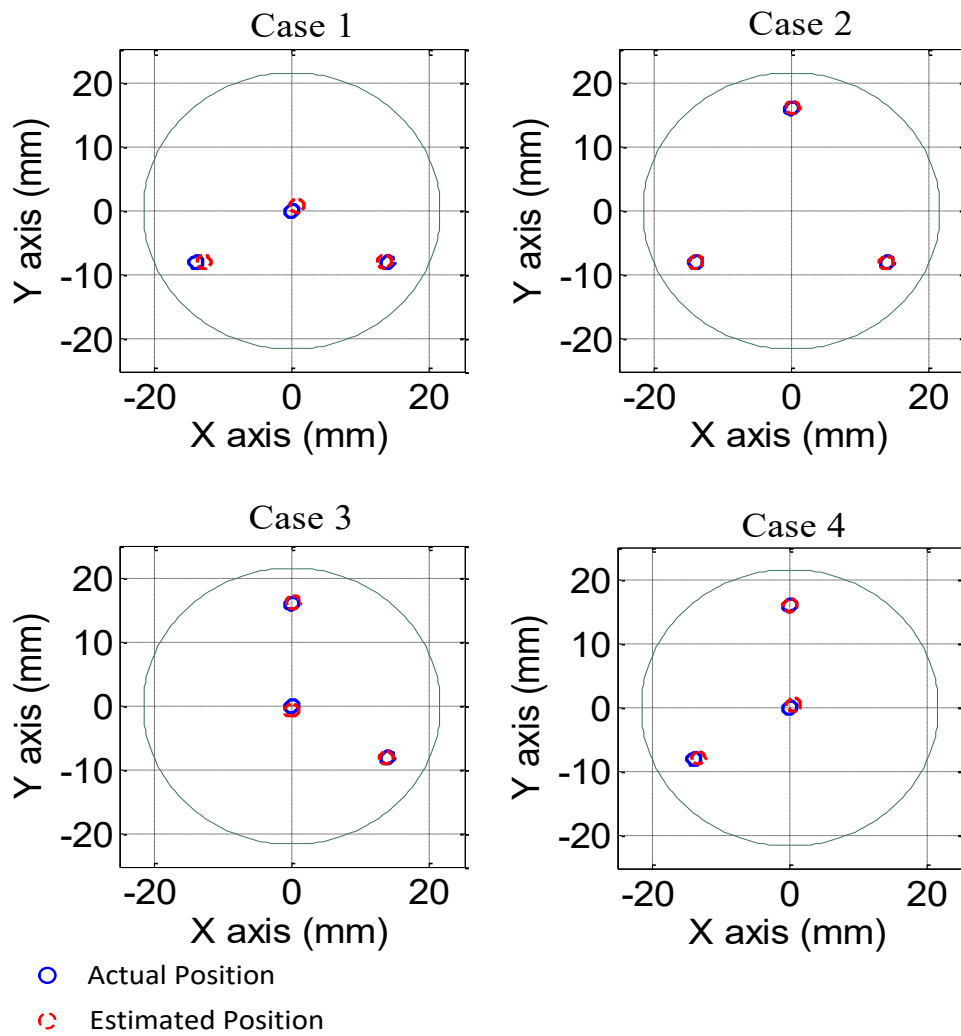


Figure 3.13: Experimental result for the conductor position computation.

3.4.4 Conductor Current Measurement Results

The estimated conductor positions are utilized to calculate the live currents. Figure 3.14 shows the experimental results comparing the calculated currents with the measured currents. The three conductors are laid out symmetrically in the cable (as the case 2 in the conductor position experiment) and the three-phase currents are balanced. The results indicate that the three-phase AC currents can be accurately calculated and effectively decoupled by the proposed currents measurement method.

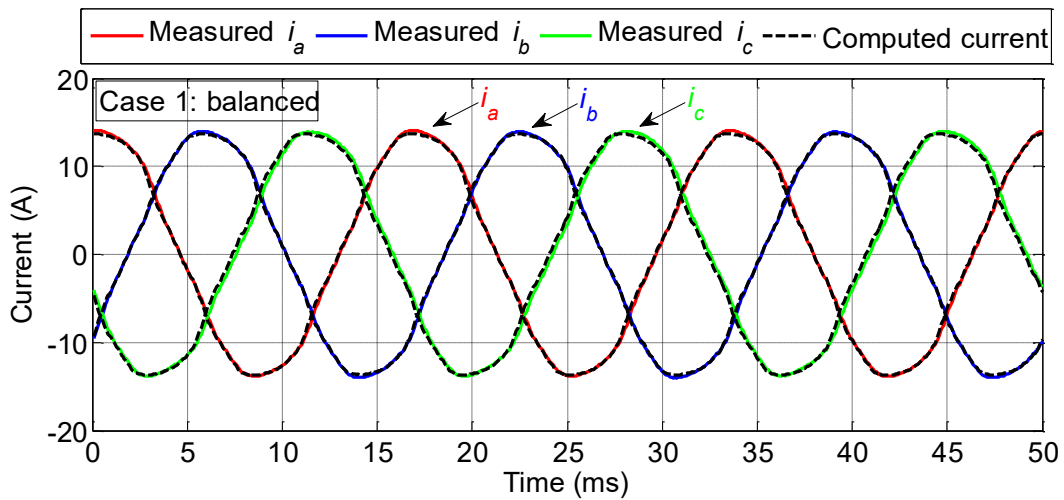


Figure 3.14: The measurement results for the three-phase balanced currents.

Additional tests are performed when the three-phase AC currents i_a , i_b , i_c are unbalanced which is common in practice. An imbalance ratio (IR) is defined in the following equation to represent different unbalanced levels in the experiments.

$$IR = \frac{|\vec{i}_0|}{|\vec{i}_p|} \times 100\% \quad (2.17)$$

where i_0 is the zero-sequence current, i_p is the positive sequence current where

$$\vec{i}_p = \frac{\vec{i}_b + e \vec{i}_c}{3} \quad (2.18)$$

Figure 3.15 shows the experimental results for the three-phase imbalance currents with

different unbalanced levels. The imbalance currents are realized by injecting single phase load into the test system. The experimental results reveal that the unbalance of the three-phase currents does not induce any additional errors.

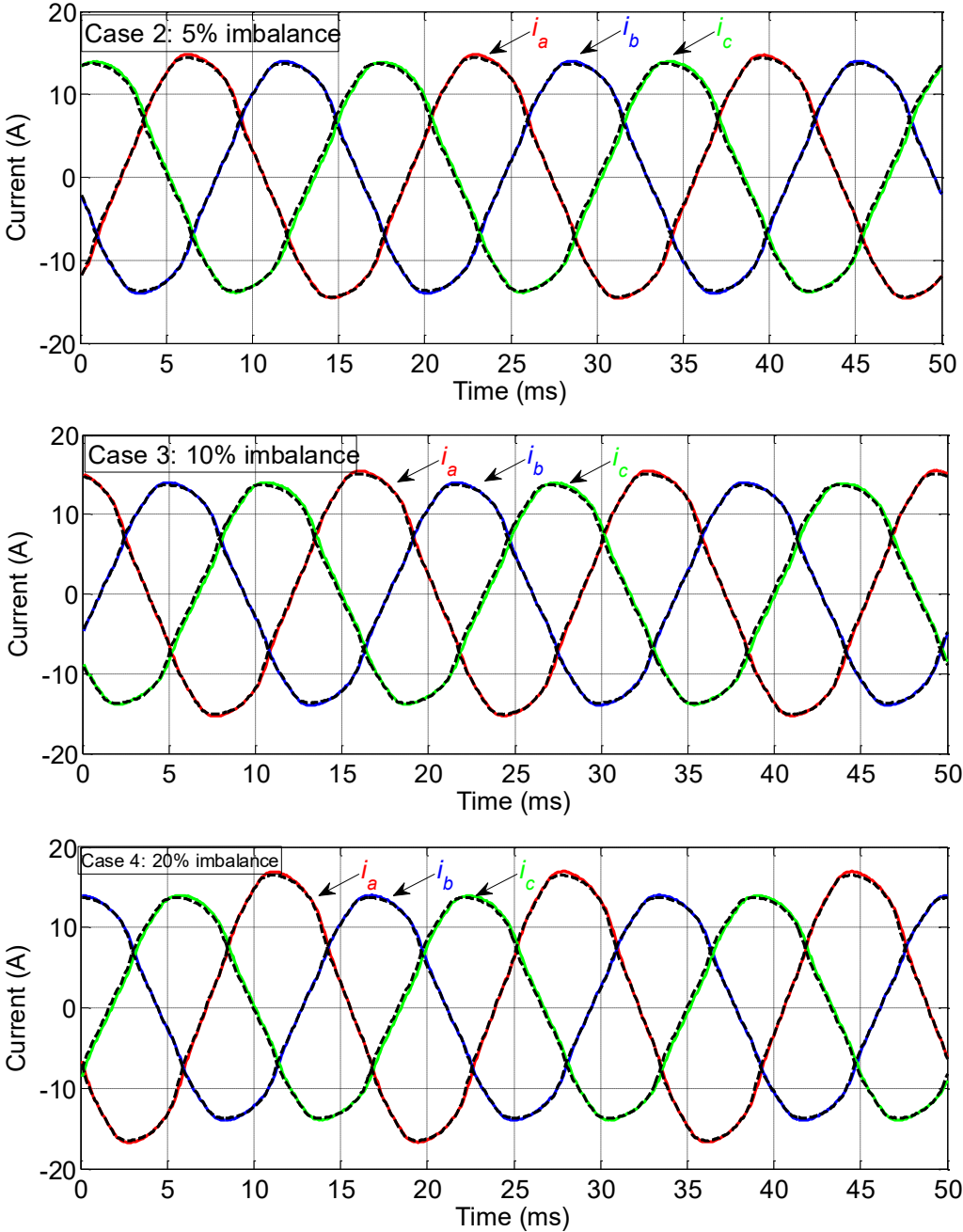


Figure 3.15: The measurement results for the three-phase unbalanced currents, Top: IR:5%, Middle: IR:10%, Bottom: IR:20%.

To further access the accuracy and robustness of the proposed currents measurement method, 180 seconds data are recorded as shown in Figure 3.16 in the case of a three-phase balanced system (hence only a phase current is plotted) for the error analysis.

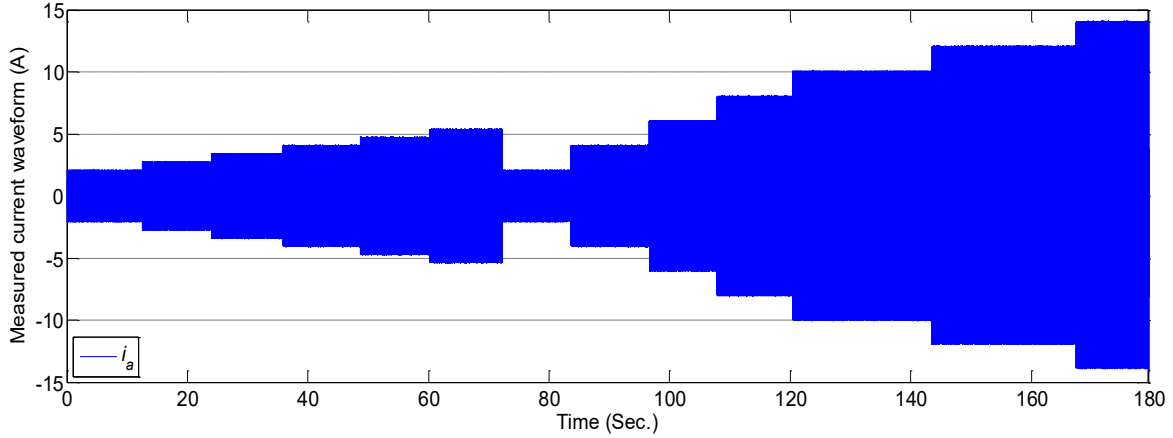


Figure 3.16: Varied current magnitude waveform.

By adjusting the loads, the current (RMS) of each phase is changed from 1.5A to 10A for examining the performance of the sensor array in different signal strengths. In the following, the error refers to the computed currents in comparison with the values from a group of commercial clamp-on current probes (the currents measured by the current probes are adopted as the reference actual currents). Both the computed and the measured current data are processed by the Fast Fourier Transform (FFT) to extract the 60 Hz components.

The current magnitude error Mag_{er} and phase angle error Ang_{er} are defined as

$$Mag_{er} = \frac{\left| \frac{\vec{i}_{cal,60} - \vec{i}_{act,60}}{\vec{i}_{act,60}} \right|}{\left| \vec{i}_{act,60} \right|} \times 100\% \quad (2.19)$$

$$Ang_{er} = \left| \theta_{cal,60} - \theta_{act,60} \right| \quad (2.20)$$

where $\vec{i}_{cal,60}$ and $\vec{i}_{act,60}$ are the calculated and actual currents at 60Hz, $\theta_{cal,60}$ and $\theta_{act,60}$ are the phase angles of the calculated and actual current at 60Hz, respectively.

To quantify the measurement error of the proposed current measurement system, Mag_{er} and Ang_{er} are characterized by the cumulative error possibility distribution, which is commonly known as the CDF (cumulative distribution function) analysis [74]. The error analysis for the current magnitude is illustrated in Figure 3.17. It is observed from Figure 3.17 (a) that the major error is contributed by the light loads, i.e., the current less than 2A. This is mainly due to the weak magnetic field generated by the small current which is more sensitive to the surrounding ambient magnetic fields. Nevertheless, it is very promising by observing Figure 3.17 (b) that the fundamental current (60 Hz) magnitude errors are always within 5%.

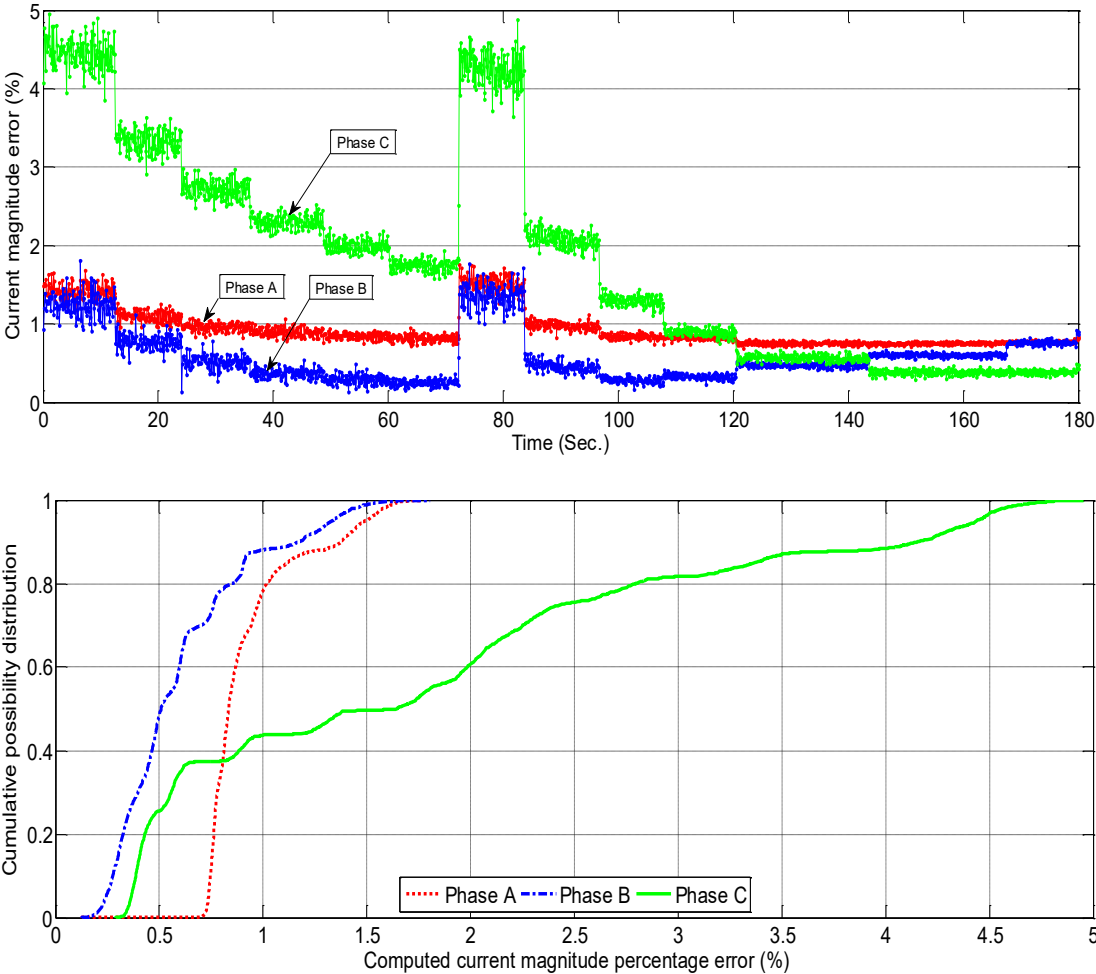


Figure 3.17: Error analysis for three phase current magnitudes: Top - current magnitude errors, Bottom - CDF analysis of three phase current magnitude.

Figure 3.18 demonstrates the analysis for the phase angle error Ang_{er} . Similarly, Ang_{er} dramatically decreases with the increasing of the current magnitude. The maximum phase angle error is 8° for phase C when the current is around 1.5A. However, this is considered acceptable as many expensive clamp-on current probes with high precision have a phase deviation of 5° when measuring small currents [75]. Such current probe is capable of measuring single conductor current only. By contrast, the method developed in this research can measure three phase currents simultaneously.

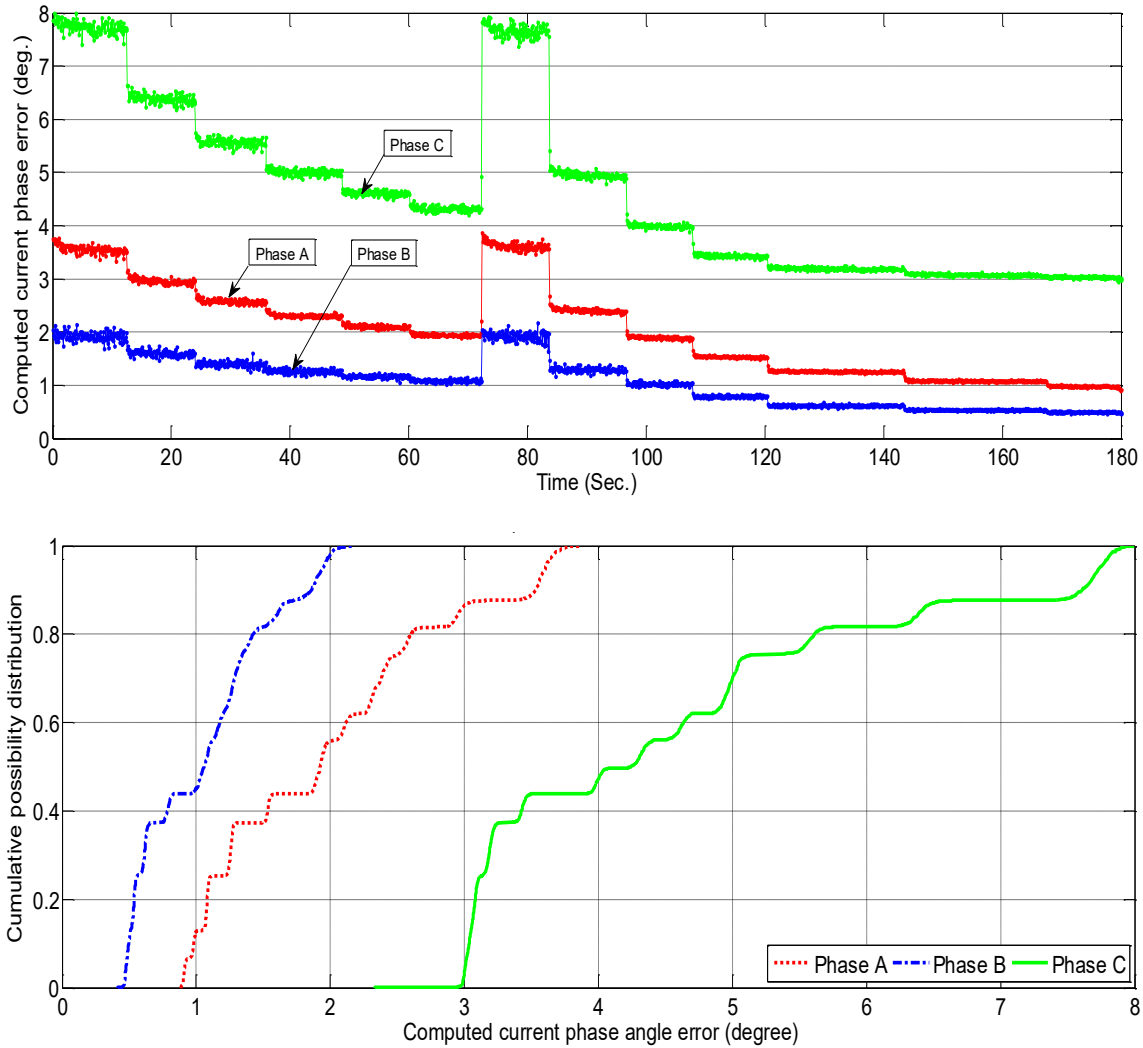


Figure 3.18: Error analysis for three phase current phase angles: Top - current phase angle errors, Bottom - CDF analysis of three phase current phase angles.

3.5 Summary

This chapter presents another novel technique for multi-conductor current measurement; it is an important supplement to the sensor array technique presented in Chapter 2. The main contributions of this research consist of three ideas.

The first idea is the proposition of an open-loop magnetic sensor array to sit on the cable under measurement. The un-hinged U-shape sensor array configuration does not need to wrap-up the cable in a closed form. It is a very user-friendly and easy-to-install design; release the stress in the practical installation from the space and cable constraints.

The main innovation of this research is to use an off-line calibration scheme to determine the sensor parameters including the sensor positions and orientations, sensor output gains and the phase shifts. These sensor parameters are treated as the knowns in later current computation. The sensor information parameters are independent to the measurement objects and scenarios. In other words, only one-time off-line sensor calibration is needed. The sensor array, after this calibration, is ready to measure different types of cables without additional calibration.

To process the sensor measurement, numerical computational algorithms are employed without knowing the conductor positions beforehand, which is the third idea of this research. After establishing the mathematical modeling of the measurement system, differential evolutionary algorithm is studied and implemented for exploring the conductors' positions. Subsequently, the lab experiments conducted by a prototype sensor array system are presented for validations. Throughout the experiments, the measurement errors were confirmed to be less than 5%. This accuracy can be potentially improved by utilizing a proper shielding scheme to eliminate the effects of outside cross-talk magnetic fields.

Chapter 4

Zero-Sequence Current Measurement for Overhead Power Lines

Knowledge of the zero-sequence current (ZSC) in an overhead power line is very important and is advantageous for many power quality studies such as troubleshooting the grounding-related power quality problems, assessing the induction issues due to the nearby power lines, and mitigating the power frequency noises and interference to the telecommunication infrastructure, etc. There is an urgent need in the power industry for a simple, portable and non-contacting sensing approach that can measurement the overhead line ZSC effectively.

The proposed research disclosed in this chapter presents a magnetic field sensor-array-based overhead line ZSC measurement technique. The main innovation of the proposed techniques is that zero knowledge regarding the overhead line geometries is required to enable the measurement, which is not achievable by most existing research works in this field. The proposed sensor array is non-contact, non-intrusive and disturbance free. It is adaptive to various field scenarios including the three-phase-three-wire overhead lines and the three-phase-four-wire overhead lines, with different electric pole/ conductor combinations, line heights, and wing spans.

4.1 Introduction

Unlike the residential service conductors or the power cables, the measurement for the overhead conductors is preferred to be carried out remotely on the ground level with a mobile setup due to safety. The medium-voltage and high-voltage line overhead power lines can be as tall as more ten meters from the ground. The power conductors have the trend to concentrate at their geometric center with respect to their ground footprints (refer to Figure 4.1). The superposed overall magnetic fields at the ground level are difficult to be distinguished by the sensor due to the insufficient geometric sensitivity.



Figure 4.1: Examples of the overhead power lines that the conductors are concentrated seeing at the ground level. (Left: three-wire without neutral, right: four-wire with neutral).

This characteristic makes it technically difficult to measure the individual overhead conductor current but at the mean time inspires our research to propose a sensor-array-based technique for the overhead power lines zero-sequence current measurement. A set of unbalanced currents flowing on the overhead lines contains the zero-sequence component in most cases [76]. Zero-sequence current (ZSC), normally denoted as \vec{I}_0 , is the vector sum of the three phase currents as below [77].

$$\vec{I}_0 = \frac{I}{3} \vec{I}_c \quad (3.1)$$

The ability to measure the power line zero sequence current in a timely and accurate manner would be very helpful for utility companies and industry in order to troubleshoot grounding-related problems [78], [79].

This chapter is organized as follows. The existing techniques attempt to address the overhead line ZSC measurement problems are reviewed in Section 4.2. The proposed scheme is formulated and explained in Section 4.3. Section 4.4 presents the simulation results for the theoretical verification of the proposed methods. The simulations are also the guideline for the design parameters to the real construction of the prototype magnetic sensor array. The actual implementation and the prototype measurement system are presented in Section 4.5, followed by the field test results for its validations.

4.2 Review of ZSC Measurement Techniques

Traditional means for the overhead line ZSC measurement are normally to install the zero-sequence current transformer (ZSCT) [80]. Reference [81] demonstrates a new measurement device based on the Faraday magneto-optical effect. This optical ZSC transducer is advantageous because of its small size, low weight, good frequency response, and high insulation level. However, these transducers require permanent installation on the electric pole/ tower or the bus bar, and therefore, are not suitable for use by the field patrol teams. Due to their high costs, the ZSC transducers can be used only at limited locations such as the substation main breaker side.

R. A. Fernandes et al. disclose a sensor module mounted on a transmission line based on the electromagnetic induction from the currents flowing through the transmission line [82]. The sensed quantities are transmitted to a ground receiver. This is a permanent installation that will restrict the measurement to limited locations. The material costs and installation

labor costs become significant when more measurement locations are needed.

An apparatus to remotely sense N parallel power conductors that carry N independent AC currents using N magnetic field sensors are proposed in reference [83]. Its particular application is the overhead line current measurement. It suggests that for the overhead lines with neutral, a regular current clamp can be hooked up on the neutral since the low voltage neutral can be accessed safely during normal operation. This will enhance the overall accuracy as the neutral current is relatively smaller.



Many known-geometry-based techniques such as the ones proposed in reference [31]-[32] use the similar approaches to measure the line currents. However, these techniques can achieve the stated performance and accuracy only for the permanent installations. In addition, they will involve difficult geometrical calibrations relying on precise knowledge of the relative positions and orientations of the sensors in relation to the conductors of interest. These methods are subject to inaccuracies when the sensors or conductors deviate from a specific, known position. Moreover, the measurement of ZSC and neutral current from the overhead lines are usually temporary for short time duration, such as the use of the field patrol team and power quality troubleshooting, these permanent sensor installations will be expensive for both capital investment and future maintenance.

The need for measuring the overhead distribution feeders is very common in the power quality research. Such measurement works are often restricted due to the insufficient data availability at the utility asset side. The capital and operation costs of the vast spreading distribution systems limit the power quality meter locations, the data capacity, and the data resolutions.

In many previous measurement works, the line currents are measured using the commercial power quality recorder such as the PQPro monitors [90] (as shown in the left side of Table 4.1). Although it is not possible to measure the high-voltage power conductor directly due

to the voltage tolerance, it can be installed at the control unit (metering or protection), where the feeder CTs are available. CTs are usually installed in the regulator, re-closer, or fault protection relays, etc. The secondary signal of the utility CTs are collected by data recording equipment to infer the scaled line currents with the combined attenuation ratio from the CTs and the equipment. However, such measurement points are very limited along the overhead lines.

Table 4.1: Data recording equipment and its connection

Data recording equipment [90]	Current probe connection
	

In other cases when the pre-installed utility CTs are not available, traditional approach to measure the overhead line currents in this time relies on the zero-sequence current transformer (ZSCT). However, the deployment of a ZSCT is a costly and time-consuming task. Power linemen are usually required to climb up the utility poles to install temporary ZSCTs for the measurement. This requirement is not only inconvenient but also unsafe for the electricians.

Instead of manipulating a hinged clamp-on CTs and the close-loop flex cable CTs, a U-shaped electronic open jaw current meter (shown in Figure 4.2) is welcome and popular for

the power line electricians. The current meter is attached on the contact end of the optical fiber telescope hot stick, which is a regular tool for the power line technician. The sensors enclosed in the open jaw sense the amperage present between its tines by the partial integral to approaching the completed loop using Ampere's Law [91].

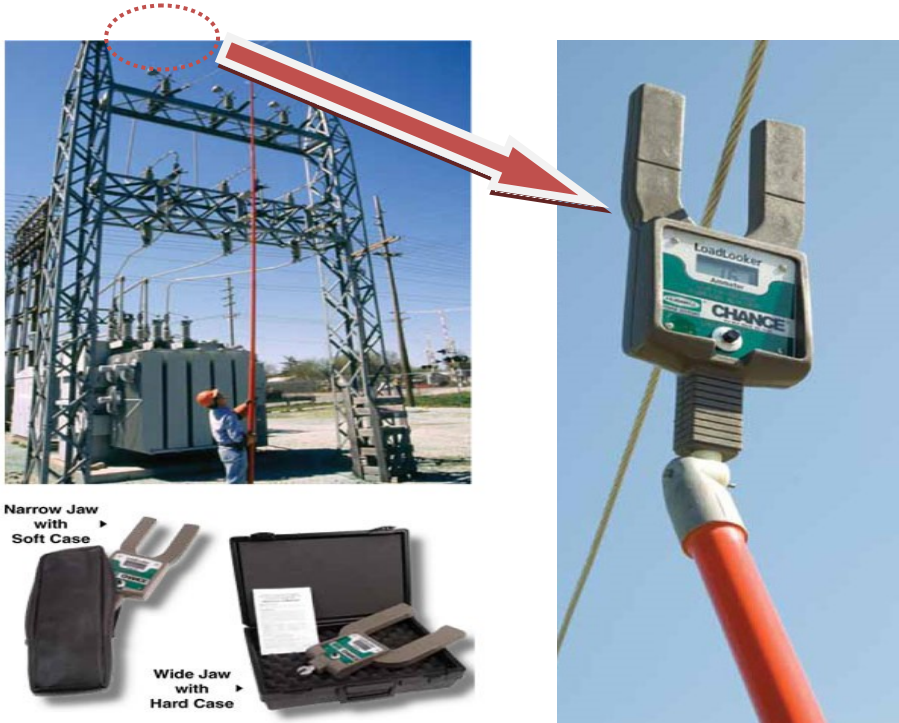


Figure 4.2: Current meter at the hot stick end for line current measurement [92].

Figure 4.3 is an improved development of the hot stick current meter that the wireless communication means are integrated to the current meter. The electrician will be able to read the measurements more conveniently without removing the contact to the hot wire in advance. Meanwhile, more parameters including the extended distance between the power conductor to the telescope hot stick end is also picked up, which is commonly used to know the conductor vertical height when the electrician stands exactly beneath the conductor.

Unfortunately, the hot stick current meter offers current RMS measurement only. It is not able to provide adequate ZSC from the overhead lines. The current waveform or the

frequency domain components are much beyond the capacity of this type of devices.



Figure 4.3: Improved wireless hot stick current meter [93].

It can be seen that the approaches introduced above are way from satisfactory in terms of the overhead line ZSC measurement. Thanks to the linearity between a magnetic field and current, the current can be reconstructed from the magnetic flux densities measured by the sensor array placed in the vicinity of the current-carrying conductors. According the ZSC computation theory derived in this chapter, a prototype ZSC sensor array has been developed. Extensive lab experiment and filed test in the actual distribution systems are conducted for the validation and evaluation purpose. The proposed sensor features simple deployment that the sensor array lays on the ground or mounts on an automobile, the later will be preferable for the line patrol personnel. It is a flexible and easy-to-use method for measuring the overhead line ZSC, and could benefit the power industry as a new tool to identify many other power quality issues in the future.

4.3 Problem Formulation

Typical overhead power lines in North America consist of several conductor bundles, separated from each other in a spatial configuration, supported by the wood or concrete

electrical pole/ tower. The conductors making up the overhead lines carry alternating current (AC) at specific frequencies, i.e., the 60 Hz fundamental current and the power frequency harmonics. Each conductor in this bundle carries one distinct AC current in a three-phase form, transmitting through the line. Normally, the three-phased currents in the three-wire or four-wire (when neutral exists) configurations are unbalanced. The neutral conductor is therefore used as the return path of the unbalance current back to the distribution step-down transformer. The neutral is multi-grounded with a grounding span of 150 meter or so [84]. However, neutral is not always needed due to the cost consideration. In fact, in the vast area with less population density (the most common cases for the overhead distribution line deployment), neutral is not included according to the survey of this research.

In this research, two magnetic field sensors for the three-wire configuration and four sensors for the four-wire systems are sufficient to compute the ZSC in real time with three implementation stages:

- 1) Installation: the sensor array is placed beneath the overhead lines vertically. The sensing point of each sensor is aligned to the center line of the middle power conductor.
- 2) Measurement: based on the existence of neutral, two or four sensors are utilized. The relative distance of every two sensors are pre-determined in the sensor array fabrication process and is used as a known factor to facilitate computation.
- 3) Computation: overhead line ZSC is computed using the sensor array measurements, in waveform, RMS, phasor, or/and harmonic spectrum forms in real-time through the proposed data processing algorithm.

The following section explains the formulation of the overhead line ZSC measurement problem. In general, a representing three-phase-four-wire distribution line layout is illustrated in Figure 4.4.

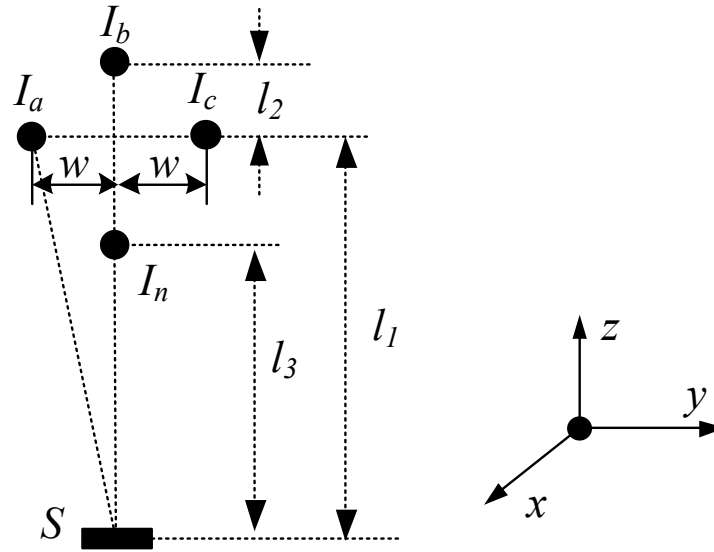


Figure 4.4: A typical three-phase-four-wire overhead power line configuration.

In Figure 4.4 three phase currents \vec{I}_a , \vec{I}_b , \vec{I}_c and \vec{I}_n flow through three overhead conductors a , b and c , and the neutral conductor n , respectively. The conductor b and c are mounted on horizontal beam of the pole with the height of l_1 , conductor a is the highest while the vertical distance from conductor a to the support beam is demoted as l_2 . Neutral is the lowest mounted on the pole with its height as l_3 . The wing span of conductor b or c to the pole is defined as w . The line parameters (l_1 , l_2 , l_3 , w) are dependent to the practical overhead system, one example obtained from a utility distribution line database (named as *N12Y40FT*) showing a practical three-phase-four-wire overhead line configuration is given in Table 4.2.

Table 4.2: The parameters of one typical three-phase-four-wire overhead system

Geometry Parameters	Dimension (m)
l_1	10.83
l_2	0.56
l_3	8.99
w	1.2

To formulate this problem mathematically, a right-handed Cartesian coordinate system is established with its origin located at a sensing point S . S is exactly beneath conductor b on the ground level, where the z -axis is toward the conductors. The currents flowing in the overhead lines (\vec{I}_a , \vec{I}_b , \vec{I}_c and \vec{I}_n) generate magnetic fields in their surroundings, where the net magnetic field at the point S is a superposition result of the individual magnetic field created by \vec{I}_a , \vec{I}_b , \vec{I}_c and \vec{I}_n associated with each conductor.

When placing a magnetic field sensor at the point S , according to the superposition theory, the magnetic field measured by this sensor is composed of two parts: the fields produced by the three phase currents \vec{I}_a , \vec{I}_b and \vec{I}_c , and the one generated by the neutral current \vec{I}_n . The phasor summation from these two parts is the actual measured flux density (as shown in Figure 4.5).

As we know, neutral current does not contribute to the ZSC but does contribute significantly to the sensor measurement because the neutral conductor is physically closer to the sensor; the ZSC measurement for the three-wire-four-wire overhead lines can be simplified to three stages as:

- 1) Find the magnetic field flux density representation in respect to the three phase currents. Completing task 1) will solve the problem for three-wire system.
- 2) Find the magnetic field flux density representation in respect to the neutral current.
- 3) Solve the ZSC from the measured magnetic field flux densities by the sensors by combining 1) and 2) with enough sensors, the neutral current is calculated at the same time.

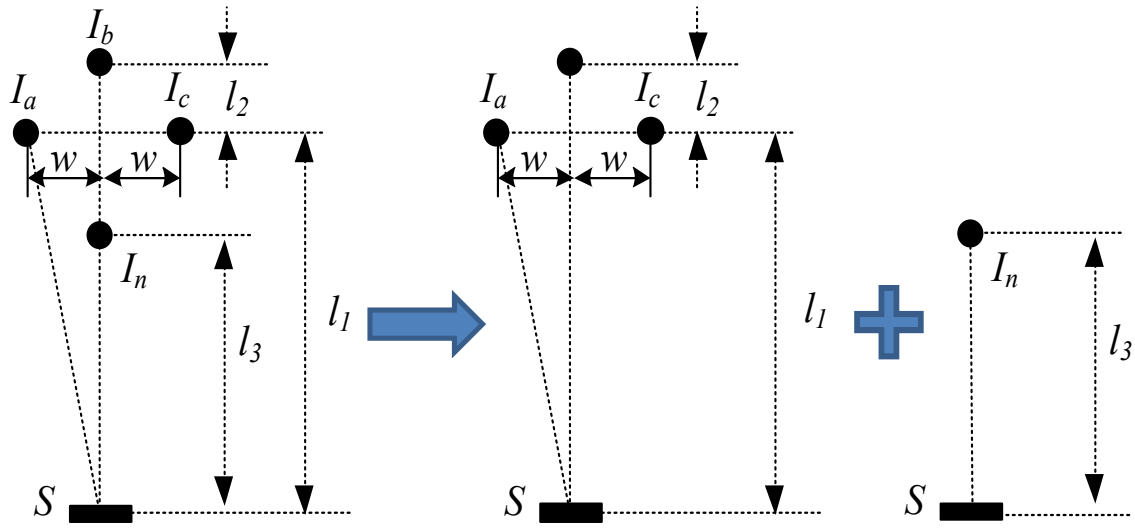


Figure 4.5: Problem formulation using superposition theory.

According to our survey, the three-wire configuration is mostly common in the distribution systems. The neutral is available only in rare locations, for instance, the industrial area and some city neighborhoods. However, the communication cables in these locations may also use the electrical poles and are under the neutral as they are with low voltages. Most of the time, power and telecom cables run in parallel together for long distances sharing the right-of-way, meaning electromagnetic coupling can be highly serious. Therefore, It is very difficult to measure ZSC due to the increased cable numbers and the shielding effect from the communication cables.

For the situations that the measurement zone is clear without the inference from the communication infrastructure, the current flow through the neutral conductor is also difficult to estimate. The neutral is grounded through the MGN topology [84]. This is generally adopted in most of the North America distribution systems, making the neutral current only easy to predict from normal power flow studies. Analysis using a multi-phase harmonic low flow (MHLF) computational tool is utilized for this type of studies [85].

4.3.1 Proposed Scheme for Three-Phase-Three-Wire System

Three-phase three-wire power lines are very common in distribution systems and are used primarily in industrial facilities to supply motor-type loads such as those from heaters, pumps and fans. The typical geometry of three-wire power lines in an overhead distribution system is shown in Figure 4.6 (a) where the three-phase currents are \vec{I}_a , \vec{I}_b and \vec{I}_c , respectively.

To measure the ZSC in this layout, two magnetic field sensors (S_1 , S_2) are deployed vertically on the ground level below the conductor that carries current \vec{I}_b . The sensor deployment is also depicted in Figure 4.6 (shown on the ground level). The sensor can be any form of magnetic sensor that is capable to infer the current based on a known relationship. This report exemplifies a preferred design applies the coil sensor that an induced voltage associated with the power line alternative currents are sensed.

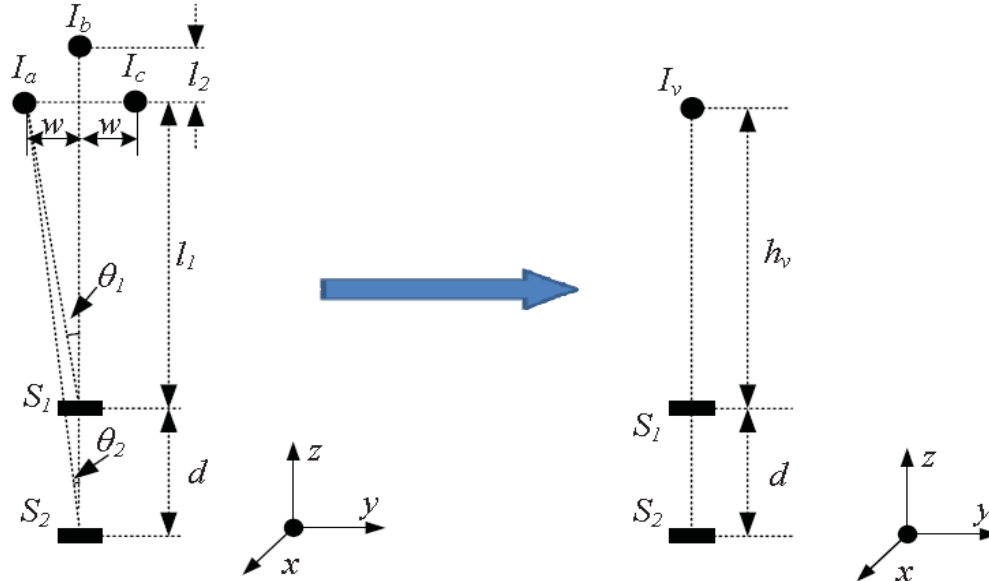


Figure 4.6: Geometry of the three-wire power lines with two magnetic sensors: Left - the actual three-phase conductors, Right - the equivalent conductor carrying virtual current.

By neglecting the displacement currents (in a low-frequency approximation) in the

Maxwell equations, it is demonstrated that the magnetic field in the free space nearby is linear with respect to the total currents flowing through the overhead lines. The magnetic flux densities (\vec{B}_1, \vec{B}_2) at the points where the sensors are located can be represented in the Cartesian coordinate system and expressed by Equation (4.2) and (4.3) according to Biot-Sawart's law.

Decomposing \vec{B}_1 and \vec{B}_2 into their three-axis components (x, y, z) will yield:

$$\begin{cases} \vec{B}_{1x} - \nu \\ \vec{B}_{1y} - \frac{1}{2\pi} \cdot \left(\frac{\vec{I}_a}{l_1} \cdot \cos^2 \theta_1 + \frac{\vec{I}_b}{l_1} + \frac{\vec{I}_c}{l_1} \cdot \cos^2 \theta_1 \right) \\ \vec{B}_{1z} - \frac{1}{2\pi} \cdot \left(\frac{\vec{I}_a}{l_1} \cdot \sin^2 \theta_1 \cdot \cos \theta_1 - \frac{\vec{I}_c}{l_1} \cdot \sin \theta_1 \cdot \cos \theta_1 \right) \end{cases} \quad (3.2)$$

$$\begin{cases} \vec{B}_{2x} - \nu \\ \vec{B}_{2y} - \frac{1}{2\pi} \cdot \left(\frac{\vec{I}_a}{l_1 + d} \cdot \cos^2 \theta_2 + \frac{\vec{I}_b}{l_1 + d} + \frac{\vec{I}_c}{l_1 + d} \cdot \cos^2 \theta_2 \right) \\ \vec{B}_{2z} - \frac{1}{2\pi} \cdot \left(\frac{\vec{I}_a}{l_1 + d} \cdot \sin \theta_2 \cdot \cos \theta_2 - \frac{\vec{I}_c}{l_1 + d} \cdot \sin \theta_2 \cdot \cos \theta_2 \right), \end{cases} \quad (3.3)$$

where μ_0 is the air permeability. The parameters w, d, l_1, l_2, θ_1 and θ_2 denote the system geometry information and are illustrated in Figure 4.6 (a).

The point-based magnetic field of the three power lines can be represented by an equivalent current (\vec{I}_v) above the sensors, considering the distances between the power lines and the sensors are much larger than the distances among the power lines ($l_1 \gg l_2$). The equivalent conductor carrying the virtual current is shown in Figure 4.6 (b) where the distance between I_v and S_1 is defined as h_v .

The use of this virtual conductor to simplify the three-wire system and compute the ZSC accordingly is the main innovation of this research. The x, y, z components of the magnetic

flux densities ($\vec{B}_{1v}, \vec{B}_{2v}$) of \vec{I}_v at the points where the sensors are located are expressed by Equation (4.4) and (4.5).

Equations (4.4) and (4.5) reveal that the magnetic flux densities produced by \vec{I}_v have only the y component. In the ZSC measurement, it is assumed that the virtual current produces the same y component of the magnetic flux density as that of \vec{I}_a , \vec{I}_b and \vec{I}_c at the locations of S_1 and S_2 , so that $\vec{B}_{1v} = \vec{B}_{1vy}$, and $\vec{B}_{2v} = \vec{B}_{2vy}$. As a result, we can substitute the y components of Equation (4.2) and (4.3) into those of Equation (4.4) and (4.5). Then the relationship between \vec{I}_v and the three phase currents \vec{I}_a , \vec{I}_b and \vec{I}_c is obtained as shown in the following Equation (4.6):

$$\begin{cases} \vec{B}_{1vx} = 0 \\ \vec{B}_{1vy} = \frac{\vec{I}_v}{\gamma \pi h_v} \\ \vec{B}_{1vz} = 0 \end{cases} \quad (3.4)$$

$$\begin{cases} \vec{B}_{2vx} = 0 \\ \vec{B}_{2vy} = \frac{d \cdot \vec{I}_v}{\gamma \pi (h_v + d)} \\ \vec{B}_{2vz} = 0 \end{cases} \quad (3.5)$$

$$\begin{cases} \vec{I}_v = \frac{d \cdot [l_1 \vec{I}_b \vec{I} \vec{I} \vec{I} \vec{I} \vec{I} \vec{I} \vec{I}]}{(l_1 + d)(l_1 + l_2 + d)[l_1 \vec{I}_b + (\iota_1 + \iota_2)(\vec{I}_a + \vec{I}_c)] - \iota_1(\iota_1 + \iota_2)(\iota_1 + \iota_2)(\vec{I}_b + (\vec{I}_a + \vec{I}_c)(\iota_1 + \iota_2 + \iota_2))} \\ \text{when } \cos \theta_{1,2} \approx 1 \\ \vec{I}_v = \frac{(\vec{I}_a \cos \sigma_i \vec{I} \vec{I} \vec{I} \vec{I} \vec{I} \vec{I} \vec{I} \vec{I} \vec{I} \vec{I})}{(l_1 + d)(l_1 + d \cos \theta_i)(\vec{I}_a \cos \sigma_i + \vec{I}_b + \vec{I}_c \cos \sigma_i) - \iota_1 [\cos \sigma_i (\vec{I}_a + \vec{I}_c)(\iota_1 + \iota_2) + \vec{I}_b(\iota_1 + \iota_2 \cos \sigma_i)]} \\ \text{when } l_1 \gg l_2, i=1,2 \end{cases} \quad (3.6)$$

To avoid the sophisticated expression of presents in Equation (4.6), several reasonable assumptions are made to simplify the formula of \vec{I}_v . One assumption, which has been

mentioned before, is: $l_1 \gg l_2$.

The line parameters from a practical overhead distribution system are already given in Table 4.2 and the geometry structure of the three-wire power lines are the same as practical overhead distribution lines. It can be seen obviously from Table 4.1 that the first assumption $l_1 \gg l_2$ is easily achieved.

In addition, Table 4.2 also indicates that the line height is much greater than the horizontal deviations of the left, right conductors to the central beam, i.e., $l_1 \gg w$ and of course then $l_1 + d \gg w$, we can further make use this second reasonable assumption to derive that $\cos\theta_1 \approx \cos\theta_2$. Thus, the virtual current \vec{I}_v can be finally simplified, as shown in the following Equation that

$$\vec{I}_v = J(\vec{I}_a, \vec{I}_b, \vec{I}_c) = \vec{I}_a + \vec{I}_b + \vec{I}_c \quad \text{with } \cos\theta_{1,2} \approx 1 \text{ and } l_1 \gg l_2 \quad (3.7)$$

Compare Equation (4.7) to the well-known Equation (4.1), it can be found that the zero-sequence current \vec{I}_0 in the three-phase-three-wire distribution system can be solved directly once the virtual current \vec{I}_v is solved using the two magnetic sensor measurements, with only negligible errors from the two assumptions.

Actually, \vec{I}_v is calculated based on Equation (4.4) and (4.5) where \vec{B}_{1vy} and \vec{B}_{2vy} are measured by sensor S_1 and S_2 , respectively. In (4.4) and (4.5), two known measurement \vec{B}_{1vy} and \vec{B}_{2vy} are sufficient to derive the two unknowns: the virtual current \vec{I}_v and the virtual conductor height h_v , combine these two equations will yield the expression of \vec{I}_v as the follows.

$$\vec{I}_v = \frac{\vec{B}_{1vy} - \vec{B}_{2vy}}{\mu_0} \quad (3.8)$$

$$h_v = \frac{\tau \cdot \vec{B}}{\|\vec{B}_{1vy} - \vec{B}_{2vy}\|} \quad (3.9)$$

Overall, the ZSC is computed by substituting Equation (4.9) into its general expression (4.1). In conclusion, the ZSC is calculated with the proposed sensor array measurements as

$$\vec{I}_0 = \frac{\vec{B} \quad \vec{B}}{3\mu_0 \vec{B}_{1vy} - \vec{B}_{2vy}} \quad \frac{\vec{B} \quad \vec{B}}{\vec{B}_{1vy} - \vec{B}_{2vy}} \quad (3.10)$$

where $\tau = \frac{2\pi d}{3\mu_0}$ is constant and the vertical separation parameter of two sensors d is determined at the sensor array design and fabrication stage, a proper selection of d will improve the measurement accuracy of the proposed sensor array. This will be further discussed in Section 4.4.

The derivation introduced above shows the overhead line ZSC can be ‘measured’ through simple and elegant computations with the help of two magnetic field sensors. It is also possible to integrate more sensors, still vertically aligned with the existing two sensors, beneath the middle conductor, to create an over-determined equation set. Many research works have proposed the algorithms for the sensor measurement quality identification and the data selection to improve the measurement accuracy [86], [87]. These algorithms (simply as the Least Square Averaging) can be studied in the ongoing research as one of the important extensions of the proposed technique supplements.

It is also worthy to mention that the ZSC can be ‘measured’ with the help of the proposed magnetic sensor array both in time domain and frequency domain, and in real-time once the sampling of the sensor measurements are also in real-time simultaneously. The frequency domain result of the ZSC is similar to the information usually provided by the common power quality meters including the fundamental components and the harmonic spectrum. The possibility to obtain the time domain result or the re-constructed ZSC waveform is very promising to benefit the latest distribution system power quality research [78], [79].

The frequency response of the proposed sensor array is almost unlimited to infer useful the high freq. harmonic information accurately, which is used to evaluate the impacts coming from the newer power electronic loads [88].

4.3.2 Proposed Scheme for Three-Phase-Four-Wire System

The previous section explains the problem formulation to complete task 1) mentioned at the beginning of Section 4.2. For the systems with neutral (as shown in Figure 4.7), the sensor measurement \vec{B}_i as shown in Equation (4.11), contains the portion caused by \vec{I}_a , \vec{I}_b and \vec{I}_c (denoted as $\vec{B}_{i,abc}$), and also the portion in respect to \vec{I}_n (denoted as $\vec{B}_{i,n}$), i is the sensor number, where $i=1, 2, \dots$

$$\vec{B}_i = \vec{B}_{i,abc} \mp \vec{B}_{i,n} \quad (3.11)$$

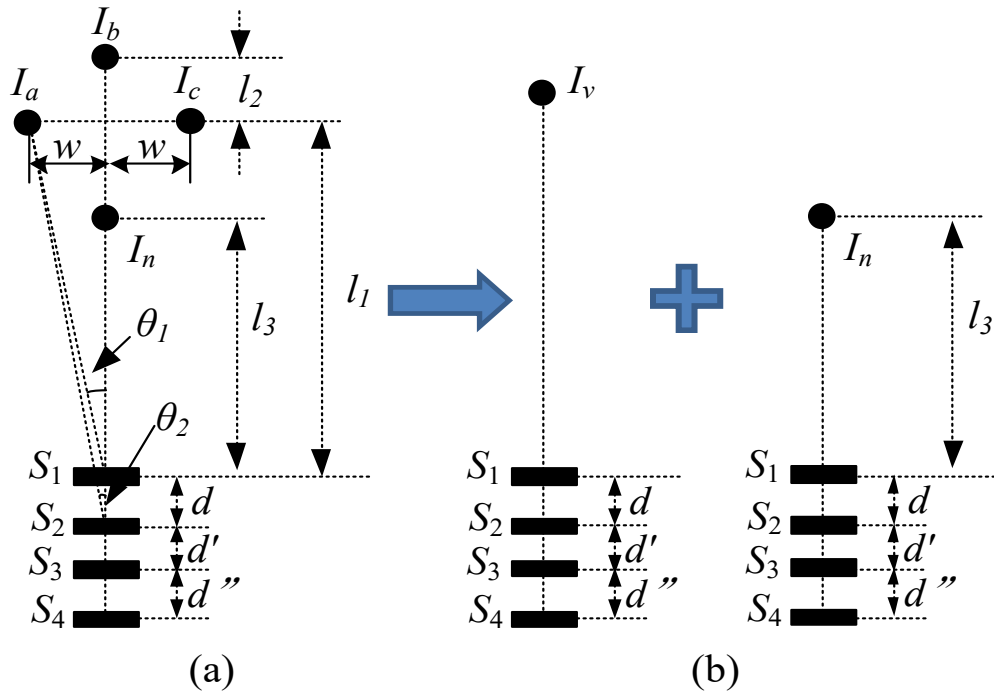


Figure 4.7: Geometry of the four-wire power lines with four magnetic sensors for ZSC measurement, (a) the actual four conductors, (b) the equivalent virtual conductor and the actual neutral conductor by superposition theory.

In Figure 4.7, the four-wire system can be decomposed as explained at the beginning of Section 4.2. From the sensor aspect, Figure 4.7 (a) is equivalent to a three-wire system, in addition to a single neutral system, as shown in Figure 4.7 (b). Therefore, we can formulate the problem for the three-phase-four-wire systems to two parts. The model of the first part is already well-established and can be used directly in the following analysis.

Similarly, as derived in Section 4.2.1, the magnetic flux densities (\vec{B}_1, \vec{B}_2) at the S_1 and S_2 points can again be expressed in the same Cartesian coordinate system by revising the Equation (4.2) and (4.3) to:

$$\vec{B}_1 = \vec{B}_{1,abc} + \vec{B}_{1,n} \quad (3.12)$$

$$\vec{B}_2 = \vec{B}_{2,abc} + \vec{B}_{2,n} \quad (3.13)$$

where the (x, y, z) decomposing components into their three-axis are

$$\vec{B}_{1,abc} \rightarrow \begin{cases} \vec{B}_{1x,abc} = 0 \\ \vec{B}_{1y,abc} = \frac{\mu_0}{2\pi} \cdot \left(\frac{\vec{I}_a}{l_1} \cdot \cos^2 \theta_1 + \frac{\vec{I}_b}{l_1} + \frac{\vec{I}_c}{l_1} \cdot \cos^2 \theta_1 \right) \\ \vec{B}_{1z,abc} = \frac{\mu_0}{2\pi} \cdot \left(\frac{\vec{I}_a}{l_1} \cdot \sin^2 \theta_1 \cdot \cos \theta_1 - \frac{\vec{I}_c}{l_1} \cdot \sin \theta_1 \cdot \cos \theta_1 \right) \end{cases}$$

$$\vec{B}_{1,n} \rightarrow \begin{cases} \vec{B}_{1x,n} = 0 \\ \vec{B}_{1y,n} = \frac{\mu_0}{2\pi} \cdot \frac{\vec{I}_n}{l_3} \\ \vec{B}_{1z,n} = 0 \end{cases}$$

$$\vec{B}_{2,abc} \rightarrow \begin{cases} \vec{B}_{2x,abc} = 0 \\ \vec{B}_{2y,abc} = \frac{\mu_0}{2\pi} \cdot \left(\frac{\vec{I}_a}{l_1 + d} \cdot \cos^2 \theta_2 + \frac{\vec{I}_b}{l_1 + d} + \frac{\vec{I}_c}{l_1 + d} \cdot \cos^2 \theta_2 \right) \\ \vec{B}_{2z,abc} = \frac{\mu_0}{2\pi} \cdot \left(\frac{\vec{I}_a}{l_1 + d} \cdot \sin \theta_2 \cdot \cos \theta_2 - \frac{\vec{I}_c}{l_1 + d} \cdot \sin \theta_2 \cdot \cos \theta_2 \right), \end{cases}$$

$$\vec{\mathbf{B}}_{2,n} = \begin{cases} \mathbf{B}_{2x,n} = 0 \\ \vec{\mathbf{B}}_{2y,n} = \frac{\mu_0}{2\pi} \cdot \frac{\vec{\mathbf{I}}_n}{l_3 + d} \\ \mathbf{B}_{2z,n} = 0 \end{cases}$$

μ_0 is the air permeability. The parameters w , d , l_1 , l_2 , θ_1 and θ_2 denote the system geometry information and are illustrated in Figure 4.7.

Again, consider only the y -axis components of $\vec{\mathbf{B}}_{1y}$ and $\vec{\mathbf{B}}_{2y}$, we have

$$\begin{cases} \vec{\mathbf{B}} & \vec{\mathbf{B}} & \vec{\mathbf{B}} \\ \vec{\mathbf{B}}_{2y} = \vec{\mathbf{B}}_{2y,abc} + \vec{\mathbf{B}}_{2y,n} \end{cases} \quad (3.14)$$

In Equation (4.15), the first portion $\vec{\mathbf{B}}_{1y,abc}$ and $\vec{\mathbf{B}}_{2y,abc}$ is expressed by introducing the concept of the virtual current $\vec{\mathbf{I}}_v$ to simplify the equation. According Figure 4.7, we can still adopt this concept to re-write Equation (4.12) to (4.14). Substituting Equation (4.4) and (4.5) to (4.14) yields

$$\begin{cases} \vec{\mathbf{B}}_{1y} = \frac{\mu_0}{2\pi} \cdot \left(\frac{\vec{\mathbf{I}}_v}{l_1} + \frac{\vec{\mathbf{I}}_n}{l} \right) \\ \vec{\mathbf{B}}_{2y} = \frac{\mu_0}{2\pi} \cdot \left(\frac{\vec{\mathbf{I}}_v}{h_v + d} + \frac{\vec{\mathbf{I}}_n}{l_3 + d} \right) \end{cases} \quad (3.15)$$

where $\vec{\mathbf{I}}_v = \vec{\mathbf{I}}_a + \vec{\mathbf{I}}_b + \vec{\mathbf{I}}_c = 0 \cdot \vec{\mathbf{I}}_0$ according to Equation (4.7) based on the assumptions that $\cos \theta_1 \approx 1, \cos \theta_2 \approx 1$ and $l_1 \gg l_2$. These assumptions still hold in the four-wire system in reference with Figure 4.7 and Table 4.2.

Observing Equation (4.15), there are four unknown variables $(\vec{\mathbf{I}}_v, \vec{\mathbf{I}}_n, h_v, l_3)$ and only two known sensor measurements $(\vec{\mathbf{B}}_{1y}, \vec{\mathbf{B}}_{2y})$. It is therefore not feasible to solve the unknowns with the limited sensor measurements, indicating more sensors are required to create

enough independent equations.

In this research, we use four magnetic sensors are utilized to compute the ZSC in four-wire systems. The vertical distance between S_1 and S_2 , S_2 and S_3 , S_3 and S_4 are d , d' , and d'' , respectively. d , d' , and d'' are all known parameters with high accuracy in the sensor array manufacturing phase. One can simply develop the following extended equation set from (4.15) for the four-sensor situation in Figure 4.7 (b). This equation set is utilized to solve the ZSC in the four-wire systems.

$$\left\{ \begin{array}{l} \vec{B}_{1y} = \frac{3\vec{I}_0}{2\pi} \cdot \left(\frac{1}{l_1} + \frac{1}{l_3} \right) \\ \vec{B}_{2y} = \frac{3\vec{I}_0}{2\pi} \cdot \left(\frac{1}{h_v + d} + \frac{1}{l_1 + d} \right) \\ \vec{B}_{3y} = \frac{3\vec{I}_0}{2\pi} \cdot \left(\frac{1}{h_v + d'} + \frac{1}{l_1 + d'} \right) \\ \vec{B}_{4y} = \frac{3\vec{I}_0}{2\pi} \cdot \left(\frac{1}{h_v + d''} + \frac{1}{l_3 + d''} \right) \end{array} \right. \quad (3.16)$$

It can be seen that (4.16) is a second order square equation set with four unknowns ($\vec{I}_0, \vec{I}_n, h_v, l_3$) and four knowns ($\vec{B}_{1y}, \vec{B}_{2y}, \vec{B}_{3y}, \vec{B}_{4y}$). It is therefore sufficiently to solve Equation (4.17) analytically if the four magnetic sensors are deployed at the preferred locations and the y -axis magnetic field flux densities ($\vec{B}_{1y}, \vec{B}_{2y}, \vec{B}_{3y}, \vec{B}_{4y}$) at these locations are measured. It is also optional to adopt various numerical computational methods to solve (4.16) considering its low order and few unknown variables. This is a good way for implementation to limit the computation burden at the MCU level. Moreover, further increase the sensor number, which will create an over-determined system, many data processing algorithms like the least-square treatment, can be performed to minimize the measurement errors and noises.

4.4 Simulation Verifications

In the previous section, the concept that a virtual current \vec{I}_v can be used to formulate the ZSC computation to avoid obtaining the specific current flow from the three-phase currents \vec{I}_a , \vec{I}_b and \vec{I}_c . The y components of the virtual current's magnetic flux densities are measured by using the proposed sensor array to calculate the ZSC. In this section, the simulation results are provided to verify the feasibility of the proposed measurement method, and will also suggest better sensor array design parameters. To avoid complicated expression, the three-wire system is used to explore the impact of the design parameters in the following analysis.

Based on Equation (4.2) to (4.5), the relationships between the root mean square (RMS) values of the y , z components of the magnetic flux densities and the distance l_1 are shown in Figure 4.8 and Figure 4.9. To simplify the analysis to provide more straightforward indications, the simulations results present in this section use the RMS values (I_a , I_b , I_c) for the currents, and the (B_{1y} , B_{2y}) for the magnetic field flux densities, etc.

The three-phase currents are balanced in Figure 4.8 ($I_a=I_b=I_c=200\text{A}$) and are unbalanced ($I_a=220\text{A}$, $I_b=200\text{A}$, $I_c=170\text{A}$) in Figure 4.9. The line geometry is identical as $w=1.5\text{m}$, $l_2=0.36\text{m}$, $d=1.0\text{m}$. The magnetic field around the overhead distribution lines is usually weak; i.e., the magnitude of the magnetic flux density is typically in the scale of milli-Gauss (mG) [89]. Figure 4.8 reveals that B_{1y} and B_{2y} are close to zero for l_1 higher than 8 meters when the three-phase currents are balanced. It can be seen that B_{1y} and B_{2y} shown good consistency that they equal to zero, resulting the virtual current I_v is also zero according to Equation (4.7). These results reflect the true situation since, in this case, the ZSC is eliminated due to $I_a + I_b + I_c = 0$.

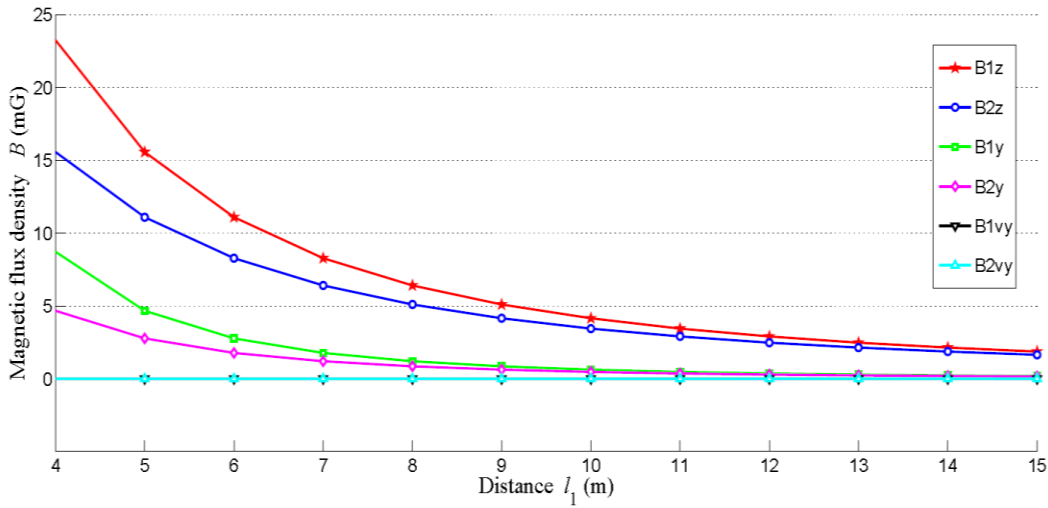


Figure 4.8: The relationship between B_z , B_y and l_1 for balanced three-phase current.

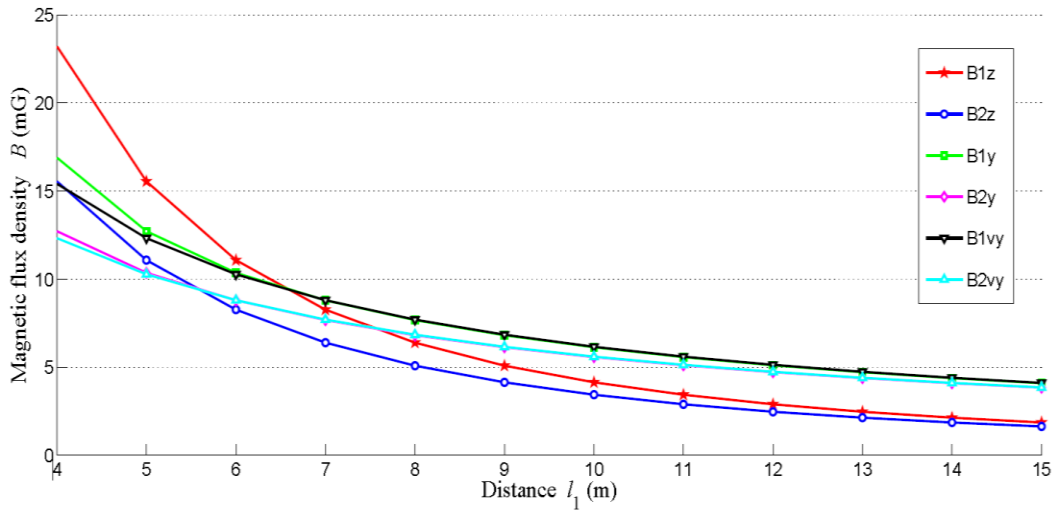


Figure 4.9: The relationship between B_y , B_z and l_1 for unbalanced three-phase current.

Figure 4.10 shows the comparison results between the estimated and the actual ZSC values when l_1 is changed from 4 to 15 meters under the same conditions of $w=1.5\text{m}$, $d=1.0\text{m}$, and $I_a=220\text{A}$, $I_b=200\text{A}$ and $I_c=190\text{A}$. It is observed that the estimated and actual ZSC values match well if l_1 is higher than 10m. The difference between the two current curves does not change much from the scenario of $l_1=10\text{m}$ to the scenario of $l_1=20\text{m}$. This result indicates that the distance of $l_1=10\text{m}$ is enough to estimate the ZSC.

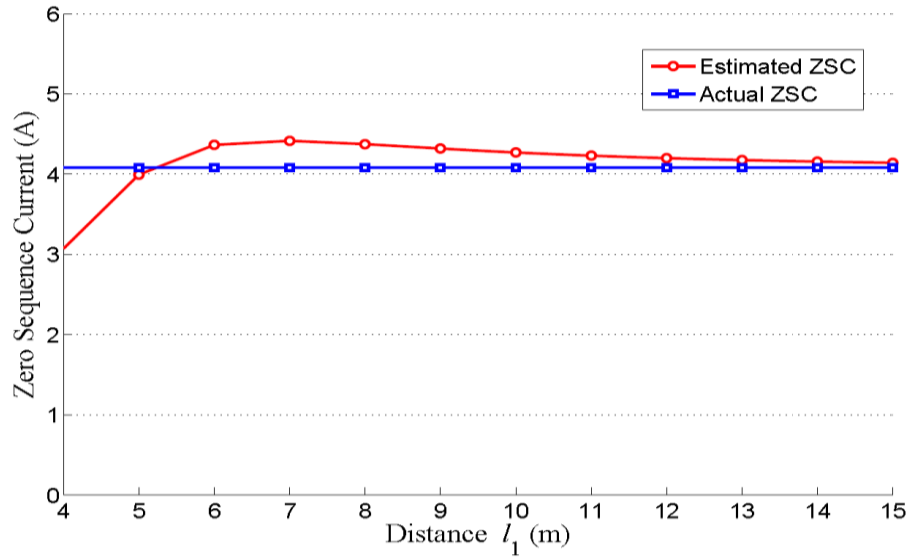


Figure 4.10: Comparison result between the estimated and actual ZSC under different l_1 .

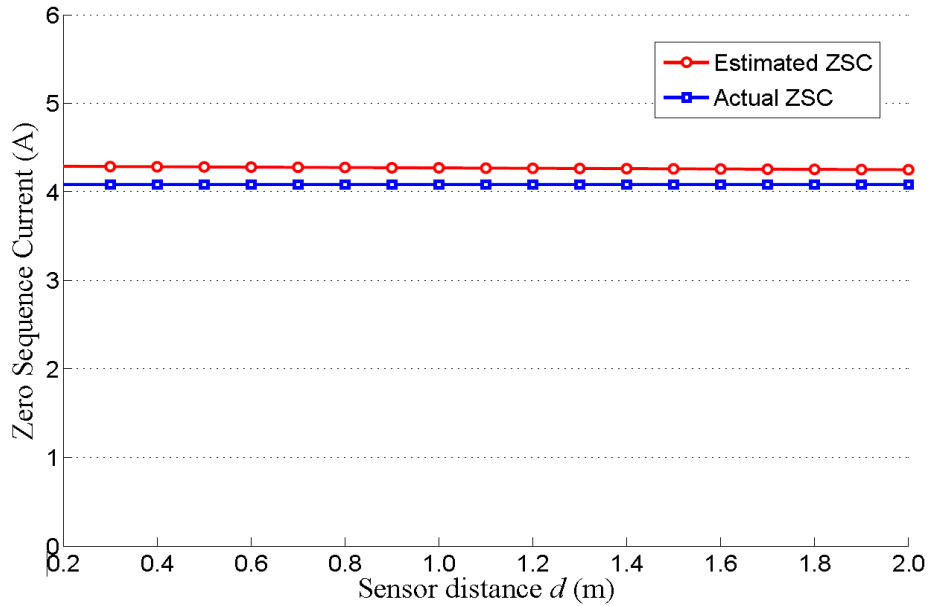


Figure 4.11: Comparison result between the estimated and actual ZSC under different d .

Figure 4.11 shows the estimated and actual ZSC curves by choosing different sensor deviations d ($w=1.5\text{m}$, $l_1=9\text{m}$, $I_a=240\text{A}$, $I_b=220\text{A}$ and $I_c=190\text{A}$). It reveals that the distance d has a very small impact on the estimation error of the ZSC. It can be seen that the change

on the estimation error is not sensitive in respect to the increasing of d . This is a promising result since we do not expect the large sensor vertical separation distance that will dramatically increase the size of the sensor array device. For practical implementation, a small distance $d = d' = d'' = 0.2$ meter is recommended to achieve satisfactory estimation with a compact device design.

The comparison results of the estimated and actual ZSC values of 50 cases (Horizontal axis is the case number) where the three-phase currents (I_a , I_b and I_c) are randomly generated between 180A and 260A are presented in Figure 4.12. The results indicate that the estimated ZSC values of the three-wire system are very close to the actual ZSC values under the conditions of $w=1.5\text{m}$, $l_1=10.0\text{m}$, $l_2=0.36\text{m}$ and $d=1.0\text{m}$. The absolute error between the estimated and actual ZSC is between ± 1 A when the ZSC varies in a wide range from 2 to 16 A.

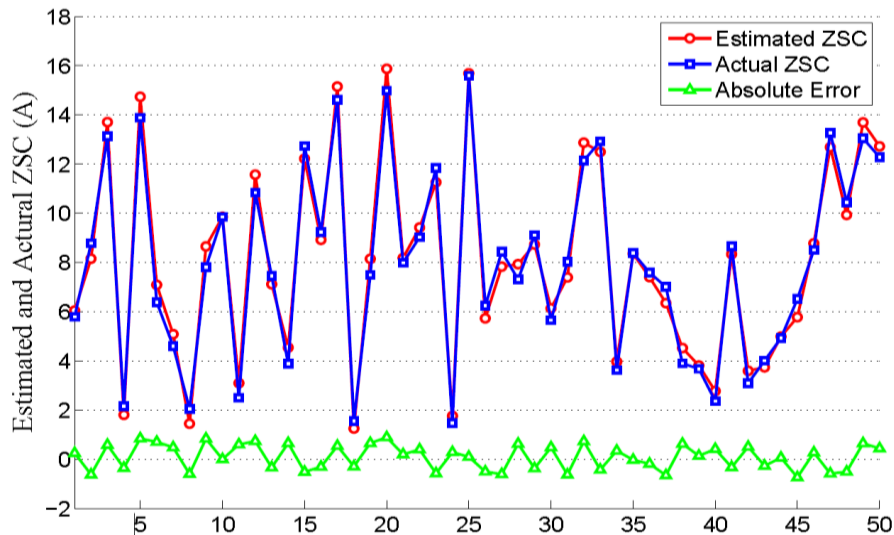


Figure 4.12: Computation errors for the three-wire system for 50 random simulation cases.

4.5 Challenges of Implementation and the Prototype Device

The ZSC is computed by the proposed sensor array by solving Equation (4.10) and (4.16). It is noticeable that these two equations rely on the knowledge of the y -axis quantities from

the magnetic field flux density decompositions, requiring the sensors to be placed exactly under the middle power conductor with their measurement plane perpendicular to the power lines. When the sensors deviate from these original ideal locations, the computation errors may appear. This section analyzes these practical implementation challenges and demonstrates in detail the solutions to address such problems.

4.5.1 Practical Challenges of Implementation

It can be seen that a proper sensor array installation at the desire positions holds the key for measuring the ZSC accurately. In other words, every sensor needs to distinguish the y -axis magnetic field flux densities in the established coordinate system. However, this is usually not possible in reality as the ground can be uneven and it is difficult to ensure the sensor's positions. The deployment uncertainties would bring unexpected estimation errors to the results and jeopardize the accuracy of the system in the practical application.

Overall, the errors can be caused by the following sensor array deployment uncertainties:

- 1) Sensors deviate horizontally, i.e., sensors are not exactly beneath the middle overhead conductor, as shown Figure 4.13 (a).
- 2) Sensors rotate vs. x -axis as shown in Figure 4.13 (b).
- 3) Sensors rotate vs. y -axis as shown in Figure 4.13 (c).
- 4) Sensors rotate vs. z -axis as shown in Figure 4.13 (d).

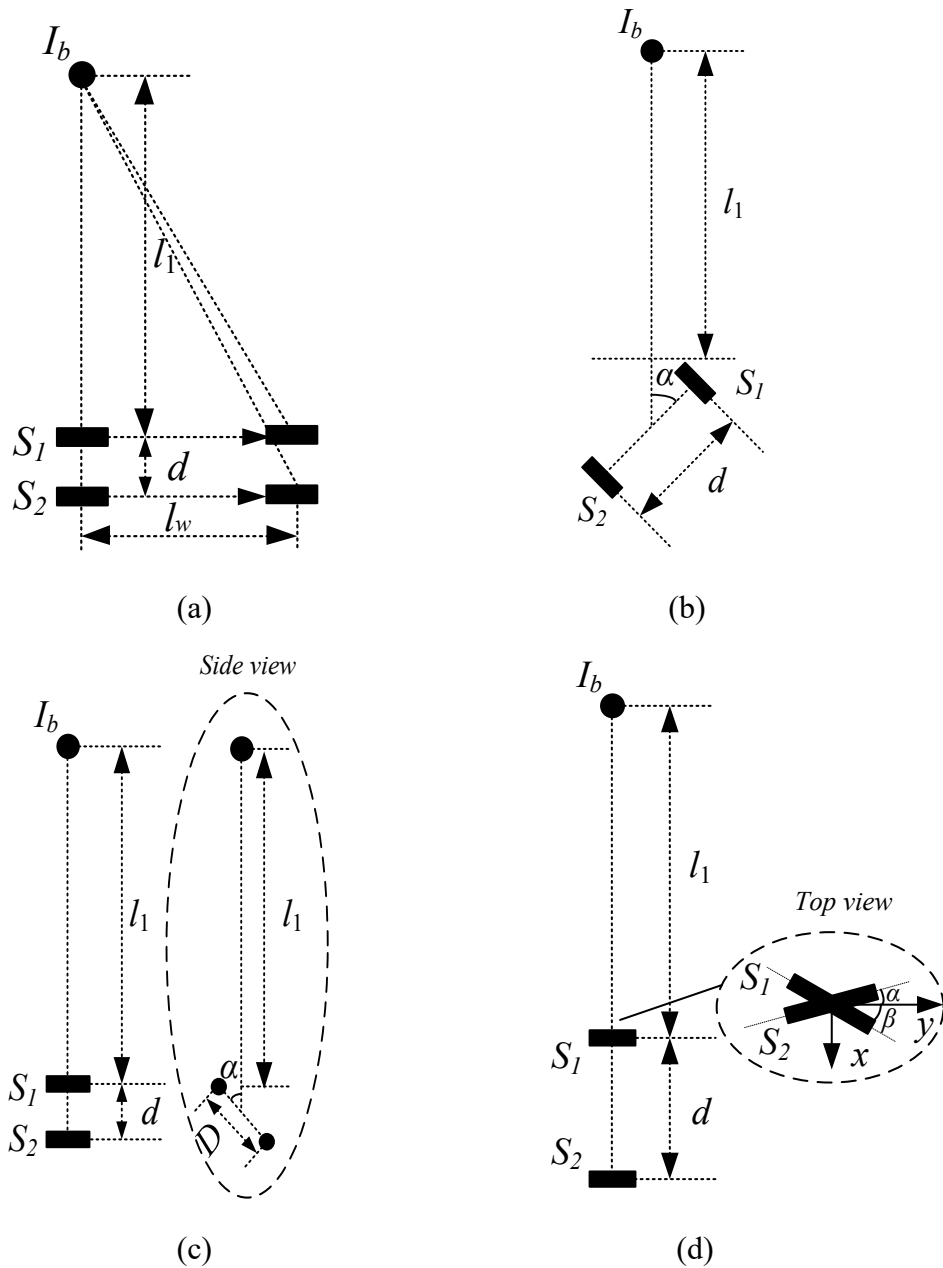


Figure 4.13: Sensor deviations from the ideal positions, (a) horizontally deviation, (b) sensor rotation by x -axis, (c) sensor rotation by y -axis, (d) sensor rotation by z -axis.

These sensor deployment uncertainties as shown in Figure 4.13 can cause unavoidable ZSC measurement errors. For example, for the three-wire systems measurement scheme using two sensors, the two sensors are usually built in one sensor array device. Once the

uncertainty 1) exists due to unsatisfactory sensor array deployment (in this case the deviations are same for both sensors), the measurement error caused by such horizontal deviation l_w from the ideal positions is presented in Figure 4.14. The horizontal deviation contributes negatively and affect the final ZSC computation accuracy. The relative error is 5% when l_w is about 2.2 meters. This effect is less severe for higher pole/ tower as the changes of l_w is not significant comparing to the conductor heights.

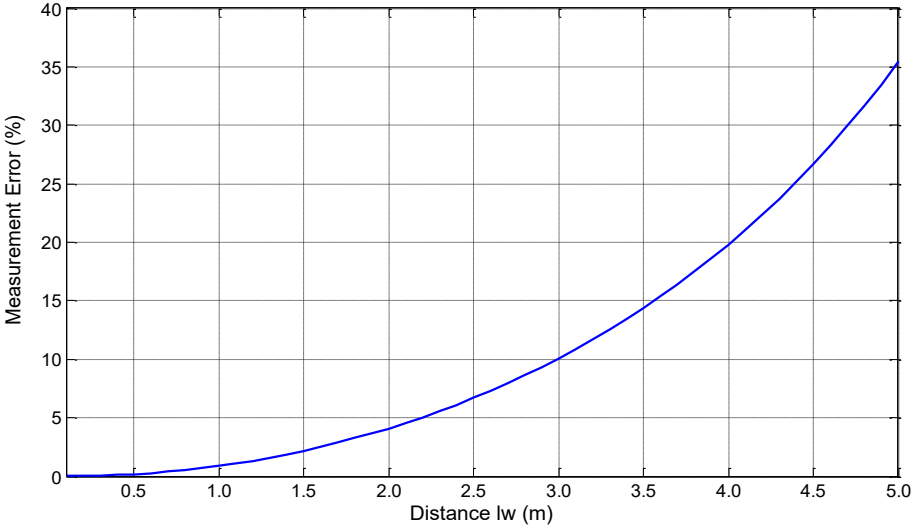


Figure 4.14: Measurement error caused by sensor deviation uncertainty.

4.5.2 Prototype Measurement System

The proposed ZSC sensor array will not achieve its best performance when the uncertainties in Section 4.5.1 occur. Therefore, we further propose a series of sensor array deployment assist schemes to overcome these challenges. The preferred sensor array prototype is a multi-layer structure to allocate multiple magnetic sensors, distance between two layers are made accurate through the facrication process and will be used for the ZSC computation. In this specific 4 layer sensor array,the distance betwwen every two layers are as same as 20 cm, i.e., $d = d' = d'' = 0.2$ meter.

The analog signal conditioning circuit for processing the sensor measurement on each layer

is fabricated on that layer, too. The final circuit outputs are recorded using a data-acquisition system consisting of an NI-DAQ instrument and a laptop. The DAQ instrument integrates a 16-bit synchronized multi-channel analog-to-digital converter (ADC). The sampling rate of the ADC is 256 points per 60 Hz cycle (15.36 kHz), which is sufficient to compute the ZSC information.

The construction of the proposed sensor array prototype involving the use of a gradiometer, a sensor mounting structure with a targeting slot, multiple magnetic field sensors, together on a tripod stand with 360 degree adjustable mounting joint. The structure of this prototype is presented in Figure 4.15.

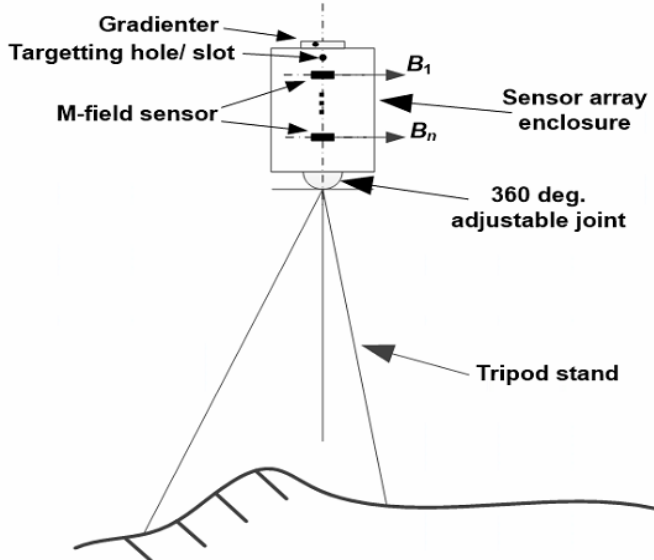


Figure 4.15: A possible design of the preferred sensor array.

To tackle the practical sensor array deployment uncertainties, a series of sensor array deployment assist schemes are included to enhance the prototype device as the follows.

1) The scheme to overcome uncertainties 1

The sensors are expected to align with the center line of overhead lines. To achieve this, a targeting structure is included in the sensor array. This structure is a slot or a long hole on the sensor array that allow human eyesight to go through this structure to observe the

electric poles from both sides. It is illustrated in Figure 4.16. The line of sight is confined in the slot. If the sensor array is not placed exactly beneath the overhead lines aligned on the center line, it is impossible to see the electric poles on both sides of the slot (Looking left and right in Figure 4.16). This structure is able to eliminate the introduced deployment uncertainties 1 as shown in Figure 4.13 (a).

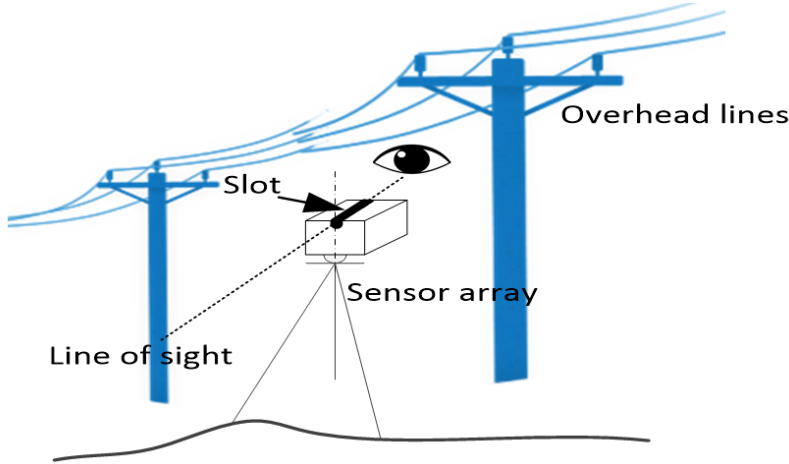


Figure 4.16: A targeting structure to overcome the uncertainty 1.

2) The scheme to overcome uncertainties 2 and 3

The sensor measurement planes can be tuned to be aligned in parallel with x - y plane using the gradienter (as can be seen in Figure 4.17). It is preferred to use three-dimensional two-dimensional gradienter to adjust the sensor array. This structure is able to eliminate the position uncertainties 2 and 3 as shown in Figure 4.13 (b) and Figure 4.13 (c).

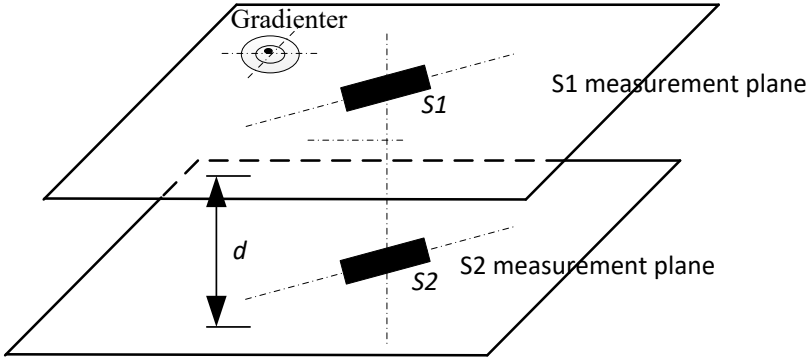


Figure 4.17: The sensor array aided by the gradienter to mitigate uncertainty 2 and 3.

3) The scheme to overcome uncertainties 4

One way to measure the y-axis magnetic field completely is to use two-axis sensors as the sensing element in the preferred embodiment. Since we know the x-axis magnetic fields produced by the overhead line currents are always zero, the only possible magnetic fields sensed by the sensors are the y-axis components. Considering the uncertainty shown in Figure 4.13 (d), the y-axis magnetic fields produced by the overhead line currents are projected to the two axes of sensors in an arbitrary strength per the sensor orientations. However, once we know the alignment angle of the two axes (for some electronic sensors in the market, the two measurement axes are perpendicular, allowing this angle α equals 90 degree), by a vector summation, it is easy to reconstruct \vec{B}_{1y} , \vec{B}_{2y} , etc.

In general, it is assumed here that the angle α between the two-axis is in the range of $[0, 90]$ degree. It can be seen in Figure 4.18, case 1 illustrates the situation that $\alpha=90^\circ$ and case 2 shows the situation that $\alpha<90^\circ$. No matter how much the sensor S rotates vs. z -axis on the x - y plane, the M-field component projected on the x - y plane can always be decoupled with the information of B_{S_axis1} , B_{S_axis2} and α as the follows.

$$|\vec{B}_S| = \begin{cases} \sqrt{|\vec{B}_{S_axis1}|^2 + |\vec{B}_{S_axis2}|^2}, & \alpha = 90^\circ \\ \sqrt{|\vec{B}_{S_axis1}|^2 + |\vec{B}_{S_axis2}|^2 - 2|\vec{B}_{S_axis1}||\vec{B}_{S_axis2}|\cos\alpha}, & \alpha \neq 90^\circ \end{cases} \quad (3.17)$$

In the actual implementation, two single axis pick-up coil (also named as the search coil) sensor are used to mimic one two-axis sensor since most of the commercial two-axis magnetic field sensors have insufficient sensitivity to fit this application according to our survey. The changing magnetic field produced by the power line currents induces a voltage in the coil sensor [14]. The two sensors are overlapped with each other to share the same position. The angle between the measurement axes are treated as unknown and is calibrated utilizing the off-line sensor array calibration scheme explained in Section 3.3.1. The selected coil sensor has an inductance of 150mH, and the diameter of the sensor is 8 millimeters [16]. Compared with the distances between the conductors to the sensors, the size of the coil sensor is negligible.

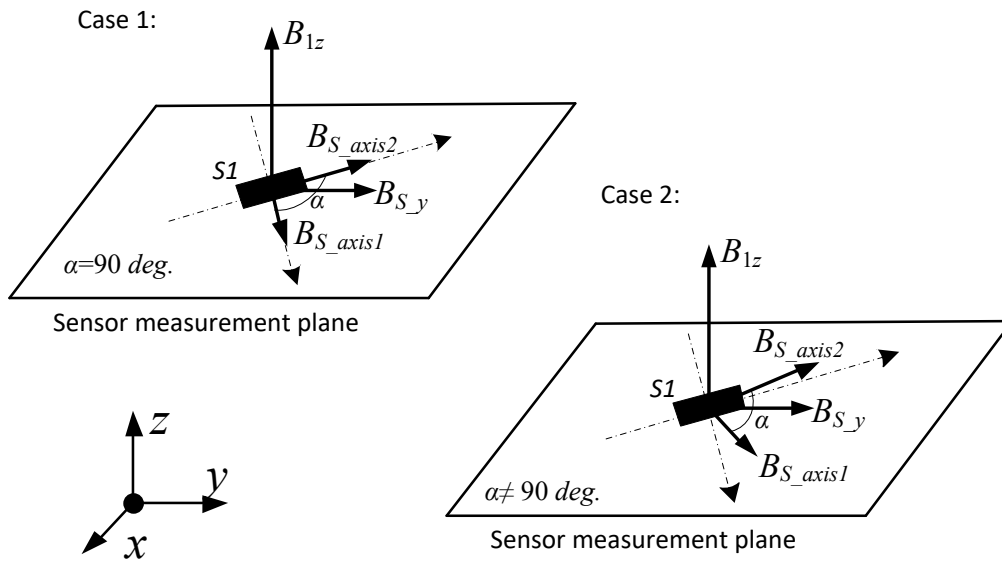


Figure 4.18: The use of two-axis magnetic field sensor.

A picture of the proposed sensor array prototype is shown in Figure 4.19. 4 layers sensing planes consisting of 8 single-axis coil sensors are included (2 sensor for one channel measurement to infer the y -axis magnetic field). All the sensors are aligned vertically to the targeting slot. Proper adjustment to ensure the correct sensor array deployment is required to initialize the measurement. It usually takes 10-15 mins to complete the setup. All of the sensors measurements are recorded by the NI-DAQ simultaneously for the future analysis.

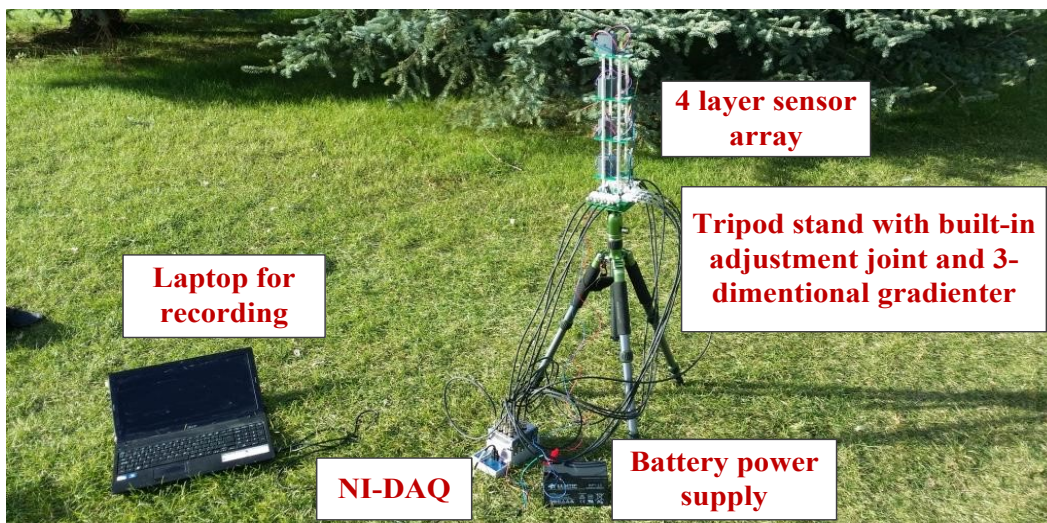


Figure 4.19: Photograph of the proposed sensor array prototype.

4.6 Lab and Field Test Validations

The proposed ZSC sensor array is firstly tested in laboratory and then verified through field experiments in two Alberta distribution systems with the support from one utility company.

4.6.1 Lab Experiment Setup and Results

The schematic diagram of the test system is shown in Figure 4.20. Figure 4.21 presents a photograph of the experimental set-up. It is noticed in Figure 4.21 that, in order to eliminate the edge effect of the finite conductors, the magnetic sensors are placed vertically beneath the middle conductor (the top conductor). Proper sensor deployment has been conducted to ensure the uncertainties caused by the sensor installation are eliminated or minimized. Thus, the two sensor outputs represent the \vec{B}_{1vy} and \vec{B}_{2vy} in Equation (4.4) and (4.5).

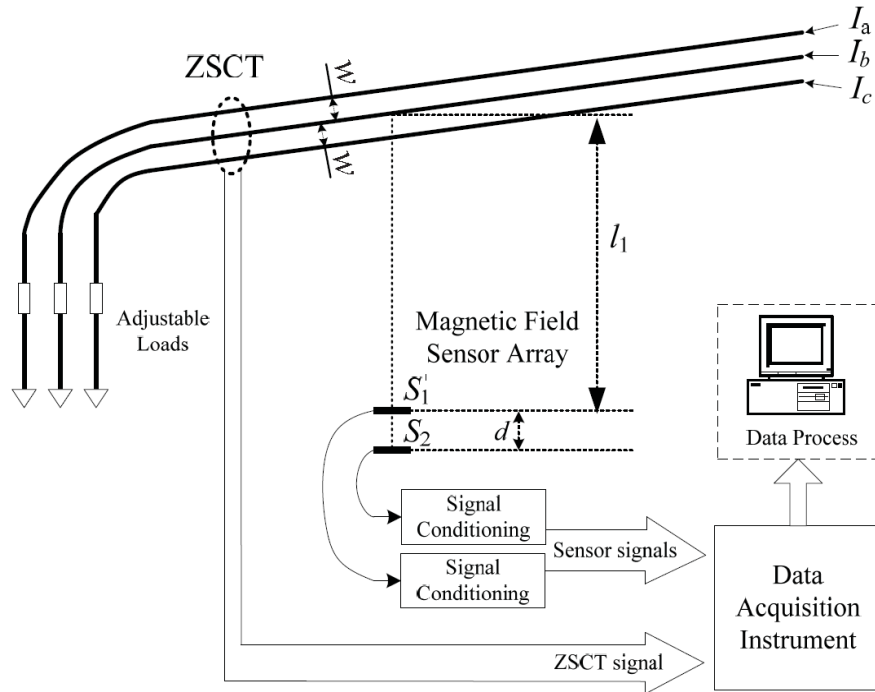


Figure 4.20: Schematic diagram and dimensions of the experiment set-up in lab.

The test system is made up of a three-phase voltage source, two magnetic sensors, three

parallel conductors, a reference zero sequence current probe (acting as a ZSCT in reality) and adjustable aggregated loads at the remote ends. Due to the lab's space limitations, the test bed is not able to be built to the real geometry as the actual distribution lines. The setup shown in Figure 4.20 and Figure 4.21 is proportionally scaled down from the geometry of actual three-wire overhead distribution lines (actual $w=0.032\text{m}$, $l_1=0.4\text{m}$, $l_2=0.01\text{m}$, $d=0.065\text{m}$). The test system has a 60Hz power frequency and the loads are tuned to create variable currents. Multiple combinations of the three-phase currents are produced to evaluate the proposed measurement system performance under different ZSC amplitudes.

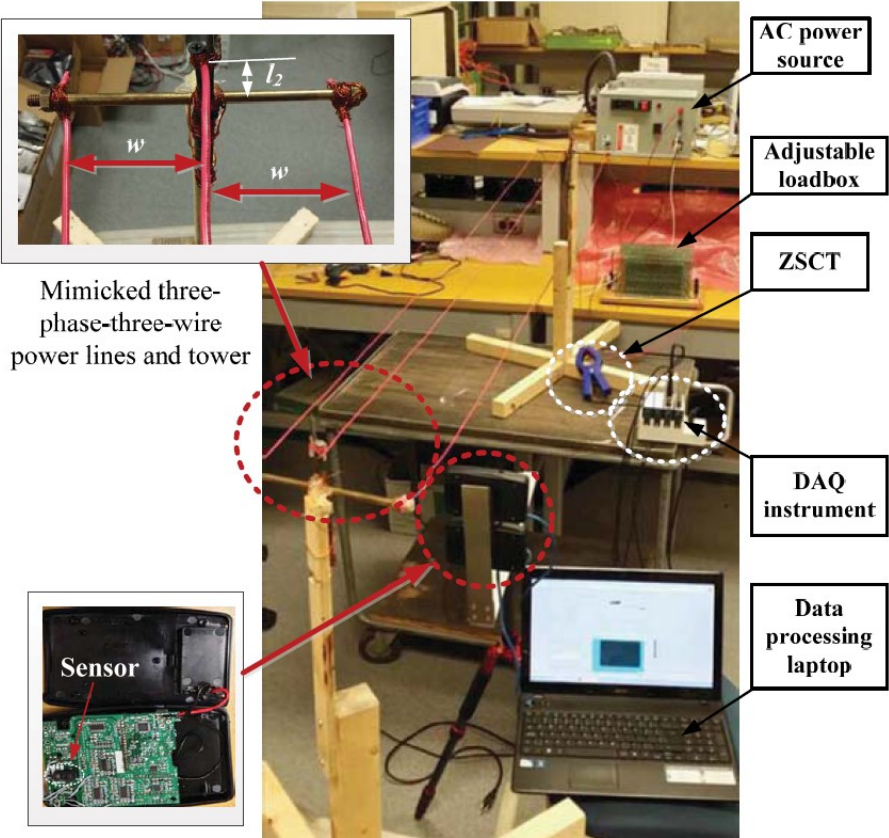


Figure 4.21: Photograph of the test bed.

The experiment data contain two channels of sensor signals and one channel of the ZSCT signal. These signals are collected by a data-acquisition system consisting of an NI-DAQ instrument and a laptop. The DAQ instrument integrates a 16-bit synchronized multi-channel analog-to-digital converter (ADC). The sampling rate of the ADC is 256 points per

60 Hz cycle (15.36 kHz), which is sufficient to compute the ZSC information.

The direct output of each coil sensor is processed by the signal conditioning circuit, which consists of a front-end analog chain to amplify the sensor output. Before conducting the experiment, the sensor circuits were calibrated in a laboratory. Its sensitivity of the output voltage to the magnetic field flux density is used to interpret the sensor circuit output back to the magnetic field strength in the data-processing program for ZSC computation.

The real-time waveforms of the three-channel signals are sampled simultaneously by the DAQ-based acquisition system continuously and are recorded in the laptop. The recorded measurement data are processed by the Fast Fourier Transform (FFT). The FFT windows capture the waveforms in a snapshot mode with the resolution of 6 cycles per second. This window is used identically at each data channel. In this way, the magnitudes of the 60 Hz components are extracted from the sensor circuit outputs (representing the real-time fields) and the ZSCT output (representing the real-time ZSC) under the resolution of 1 point per second. The FFT computation results are used to calculate the ZSC according to Equation (4.10). The detailed flow chart of the signal processing and computation procedures is presented in Figure 4.22.

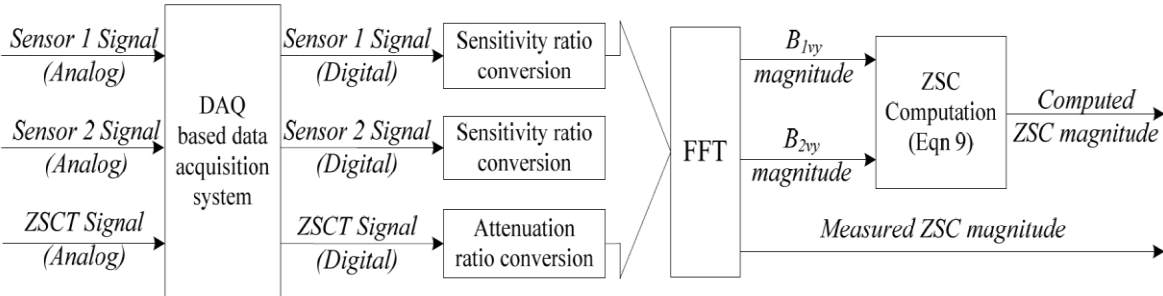


Figure 4.22: The signal flow chart of the proposed ZSC measurement system.

By adjusting the loads, the ZSC magnitudes of the experiment conductors are varied to test the sensor array performance. As can be seen in Figure 4.23, the sensor array prototype

successfully detects a ZSC as small as 0.5A with satisfactory signal performance. This result is sufficient for the field ZSC monitoring. The sensor circuit output becomes noisy when the ZSC is too weak (under 0.3 A) because the electronic noises from the power source and chips. Our proposed measurement system should be able to detect substantially smaller currents with optimized hardware for low electronic noise.

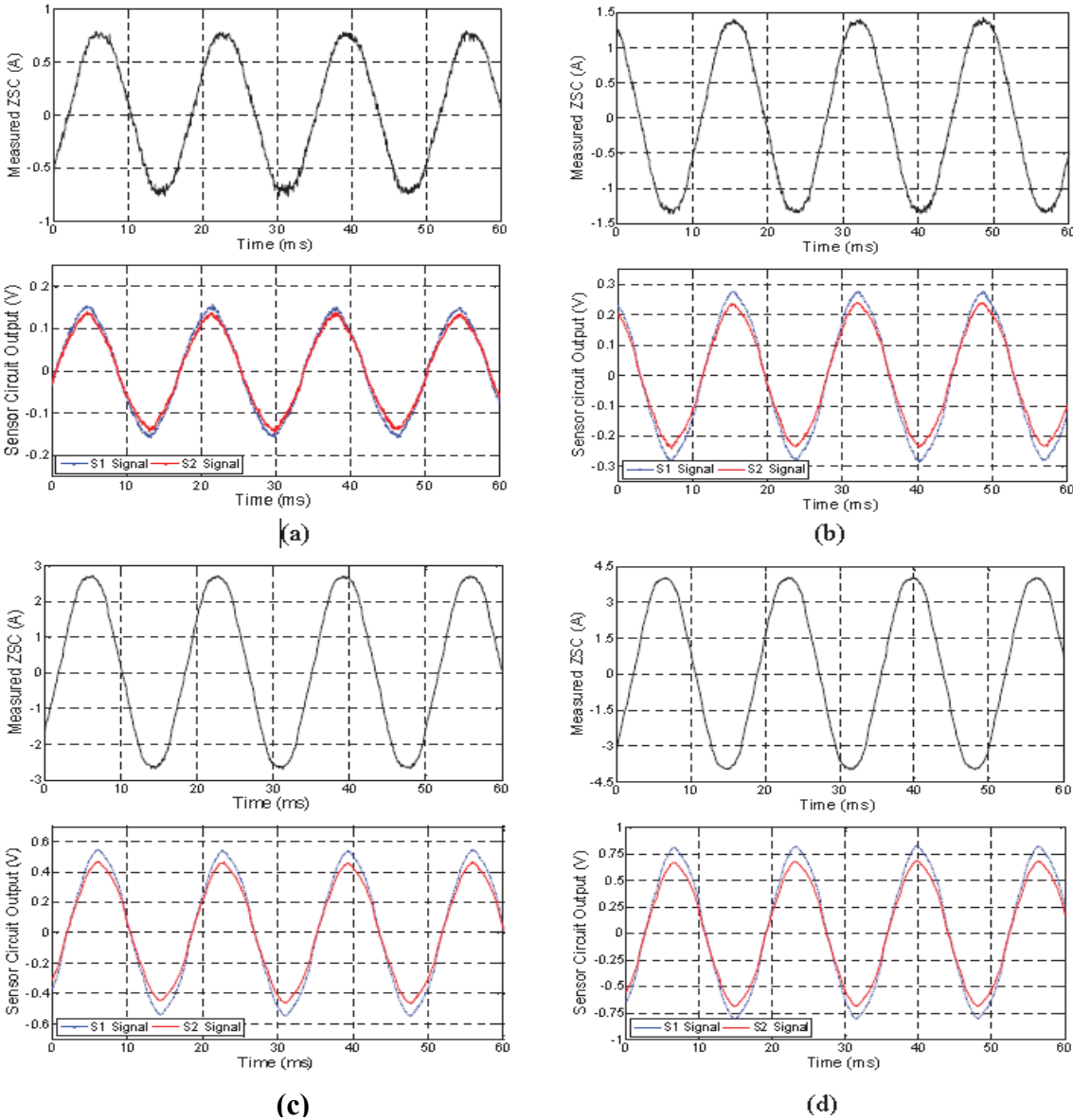


Figure 4.23: Waveforms of the measured ZSC and the sensor signals. (a): waveforms for weak ZSC, (b) and (c): waveforms for intermediate ZSC, (d): waveforms for strong ZSC.

Figure 4.24 presents the comparison results between the computations based on the proposed method and the zero sequence current probe measurements. The ZSC amplitude in the tests is varied from 0 to 6 A by adjusting the loads. The magnitudes (RMS values) of the ZSC are shown. In Figure 4.24, the relative error is less than 5% in the entire ZSC range. The experimental results reveal that the proposed measurement method can estimate the ZSC accurately for a three-phase three-wire power line system.

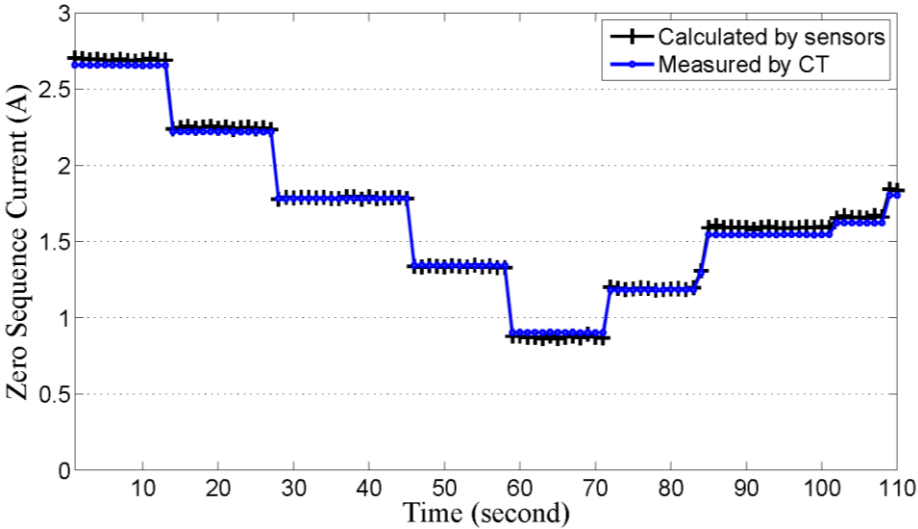


Figure 4.24: ZSC results comparison between the computation and ZSCT measurement.

The results demonstrated above are all from the single-axis sensors placed at the ideal positions, and with ideal sensing orientations. This can be achieved in the lab setting but is usually difficult in the real world measurement environment. In an actual implementation, one possible difficulty caused by the uncertainty could result from the incorrect placement or orientation of the sensor. The sensor placement deviations therefore will cause measurement errors which are already explained in Section 4.5.1.

Additional means proposed in Section 4.5.2 are integrated in the prototype sensor array device to ensure the sensors are placed properly. The filed test results from this prototype sensor array, aided by the sensor array deployment assist schemes, are further presented in the next section.

4.6.2 Field Test Description and Results

The ZSC measurement results from the lab experiments are promising and indicate the great feasibility of the proposed ZSC sensor array. The drawback of the lab experiments is that the test bed is a ideal scaled-down platform that will not reflect the true magnetic field strength in the field environment. It is preferred to test the prototype ZSC sensor array in the actual distribution systems and compare its computed results to the utility meters for validations more convincingly and effectively.

The main objective of such field measurement exercise is to examine the prototype ZSC sensor array for the following items:

- Evaluate the sensor sensitivity in the real field environment.
- Evaluate the proposed device in terms of feasibility, convenience and reliability.
- Verify the proposed ZSC computation scheme by comparing to the utility CT recordings.

With the support of one Alberta utility company, two distribution lines are measured using both the proposed sensor array (to infer their ZSC), and the Candura PQ-Pro power quality analyzer (to record the utility CT signals and then calculate the actual ZSC for reference). Each distribution system is measured at the same time by two set of devices:

- The Candura PQPro power quality analyzer [90] is used to measure and record the actual feeder line currents by collecting the utility metering CT signals. Continuous recording with 256 points/cycle (15.36k Samples/second) sampling resolution is set for all the measurement period. Such recordings are processed after test to calculate the actual ZSC (treated as the reference values).

- The proposed ZSC sensor array as shown in Figure 4.19 is deployed vertically beneath the overhead lines. A proper sensor array position adjustment with the help of the deployment assist schemes is carried out each time before the measurement start. All the sensor array outputs are recorded with the same sampling resolution 256 points/cycle (15.36k Samples/second) by the NI-DAQ data acquisition equipment and are processed after the test to calculate the estimated ZSC (treated as the computed values).

The first measured distribution system is a three-phase-three-wire 25 kV feeder supplying a gas plant (shown in Figure 4.25). The loads are mainly drive and motor type, meaning the current unbalance condition is not serious.

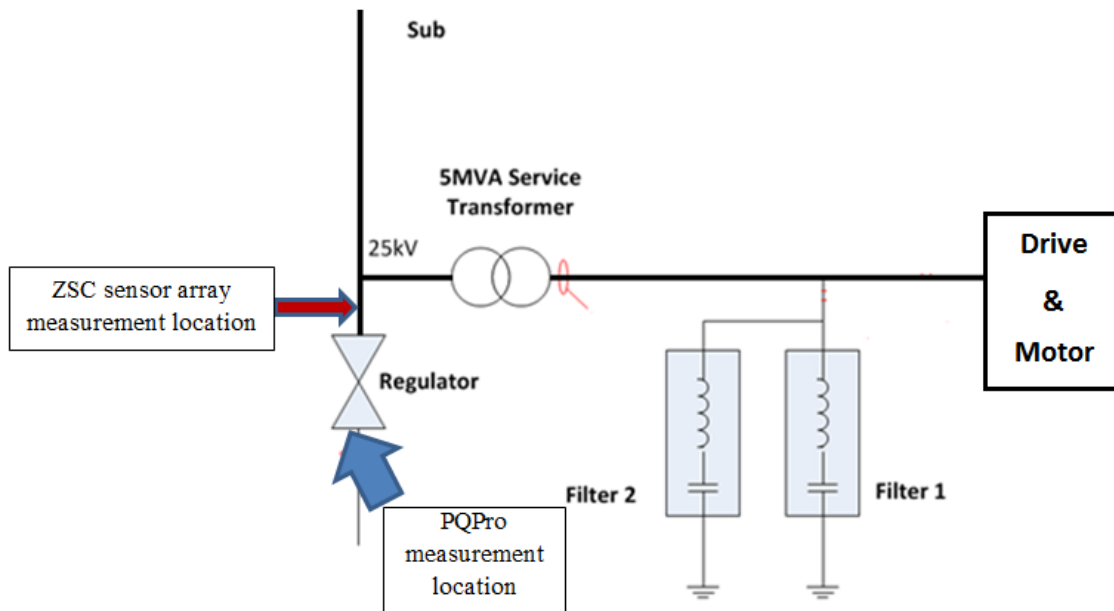


Figure 4.25: First distribution system measurement set-up.

The feeders current are obtained by measuring the secondary of the utility CT at the line regulator as shown in Figure 4.26 (a). Three utility CTs are accessed as shown in Figure 4.26 (b). The total attenuation ratio of the measurement data is the multiply results from the utility CTs and the PQPro CTs. This ratio is recorded to process to reconstruct the actual

feeder currents. The sensor array prototype is deployed under this distribution feeder meantime (shown in). Dedicated attention is taken to ensure the line currents measured by the PQPro is also the ones measured by the sensor array.

Similarly, the second distribution system, a three-phase-four-wire system, is measured by the same setup. However, there is no utility CT to measure the neutral current, so the results demonstrated in the next section will not show the comparison results between the measured and the computed ZSC. It is not difficult to understand that the neutral current computation is at the same time acceptable once the computed ZSC is accurate considering the significant magnetic coupling from the neutral current to the sensor measurements. The actual ZSC is still measured from the three-phase line currents at a regulator location while the sensor array prototype is deployed under this distribution feeder (beneath the neutral as shown in Figure 4.27 and Figure 4.28).



(a)



(b)

Figure 4.26: PQPro measurement for the first distribution line at the line regulator location.

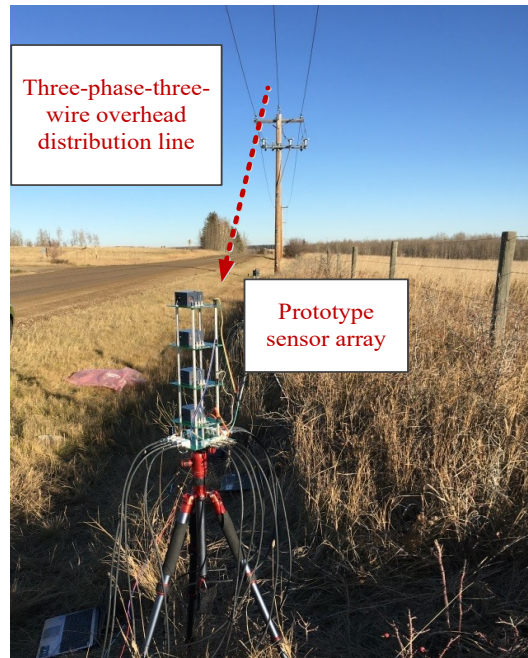


Figure 4.27: First overhead line ZSC measurement by the propose sensor array.

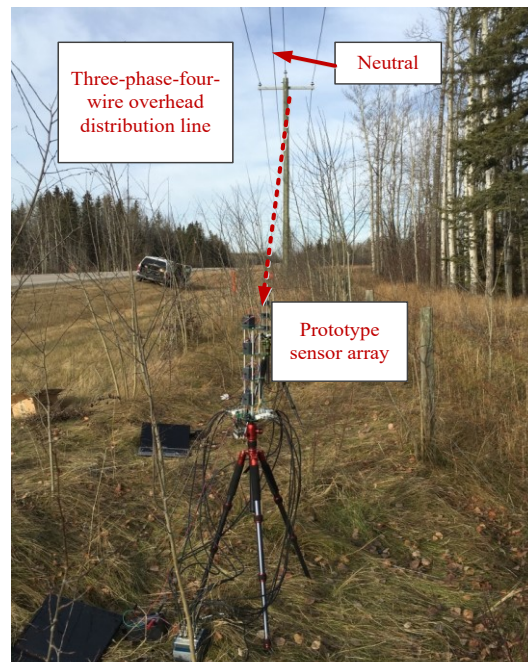


Figure 4.28: Second overhead line ZSC measurement by propose sensor array.

Some preliminary field test results are presented in Figure 4.29 and Figure 4.30. It is

observed that although the feeder current at the first location is much larger than the second location, their ZSC values are close. This is due to the different loading type, the aggregated three-phased loads such as drives and motors that are usually balanced loads are supplied by the feeder at the first location. Oppositely, the distributed load combinations including the residential loads and industrial plants are connected downstream to the feeder at the second location, making its unbalancing level more serious.

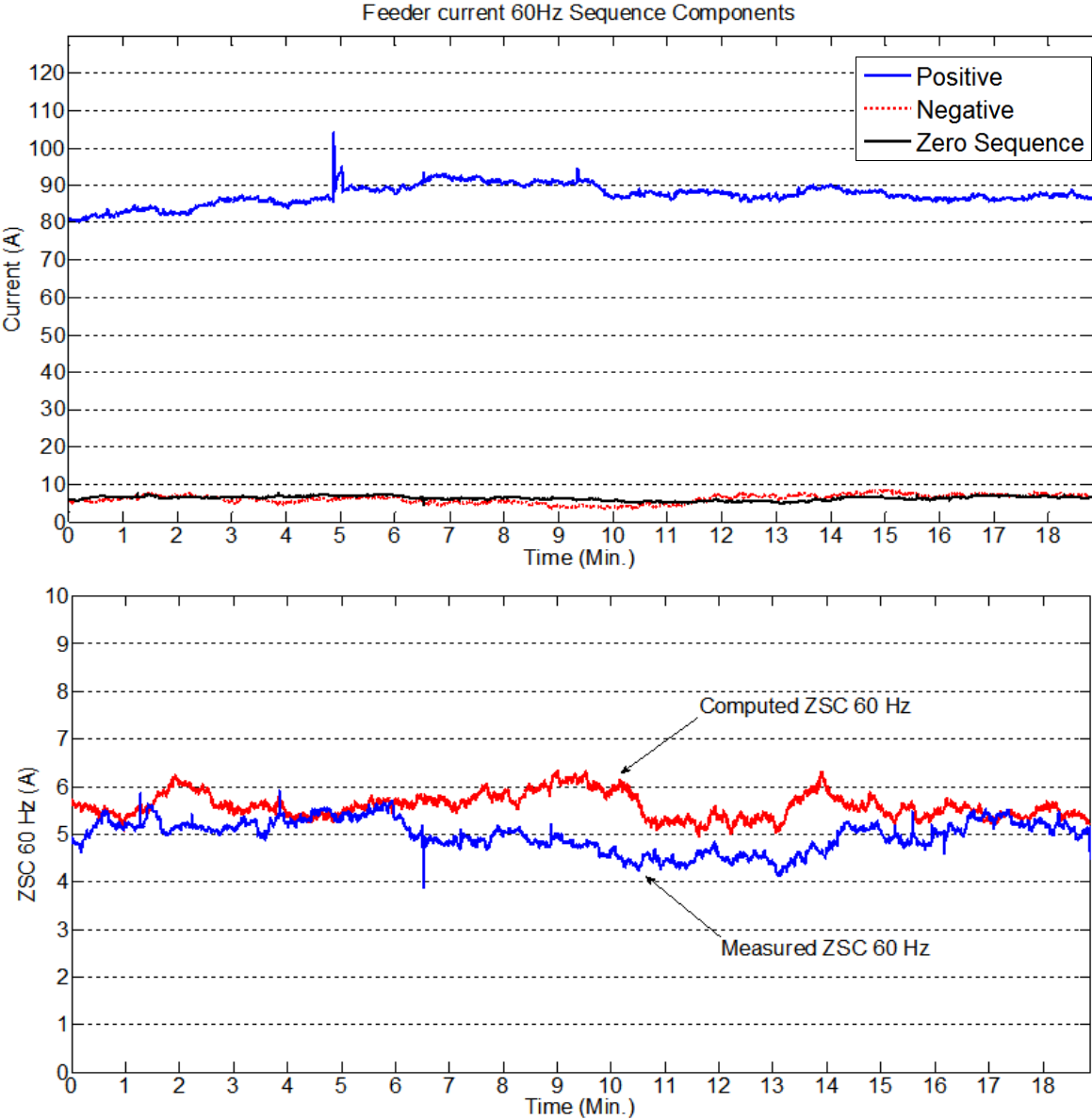
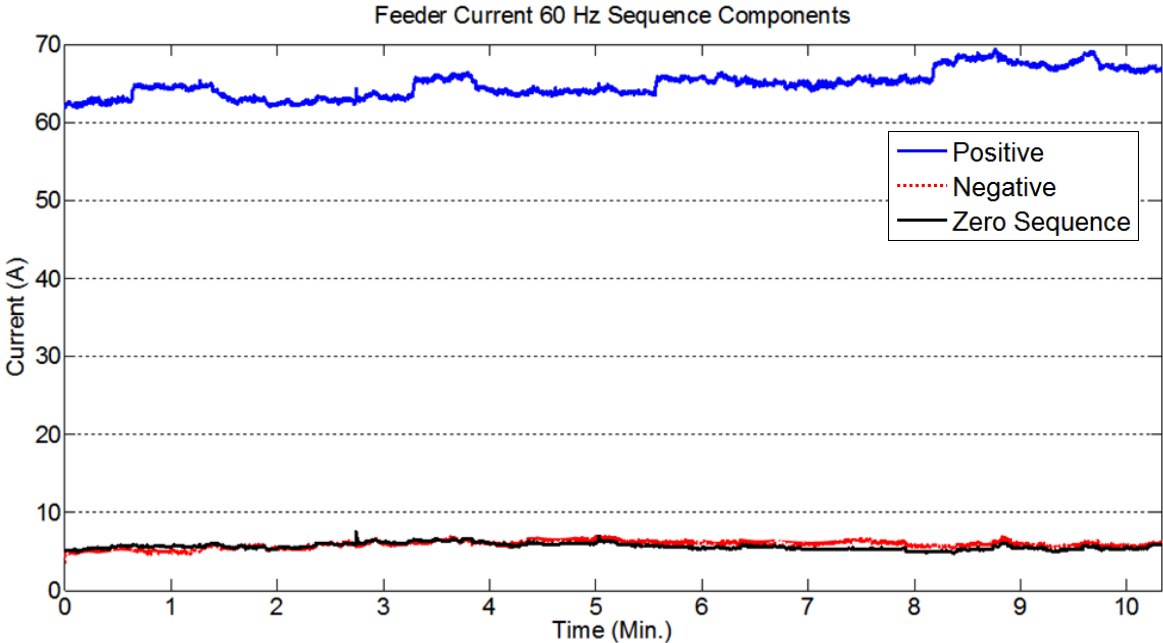


Figure 4.29: Feeder current and ZSC computation results at the first location.

For both feeders, the 60 Hz sequence components calculated from the PQPro measurements are plotted to demonstrate relative ZSC strength. Also, the 60 Hz ZSC based on the sensor array measurements are compared to compare to the actual ZSC values.

Figure 4.29 presents the results for the first location. The ZSC values of the three-phase-three-wire overhead lines are computed by Equation (4.11). The ZSC magnitude in the tests is varied from 4 to slightly over 6 Amp. Refer to the bottom computation comparison figure in Figure 4.29, the ZSC error is usually within 1 Amp. The error in the field test is larger than the results obtained from the lab tests. This is possibly caused by the external magnetic field interference as the test location is close by the regulator. Other possible reason can be the unknown underground cable, or other magnetic field conductive metal objects nearby.

Figure 4.30 shows the improved ZSC measurement accuracy at the second location. It is computed by solving the Equation (4.17) numerically. Some oscillations at the beginning and around the 7th minutes can be seen in the bottom computation comparison figure shown in Figure 4.30. This problem is potentially addressed by using more sensors, to achieve an averaged solution.



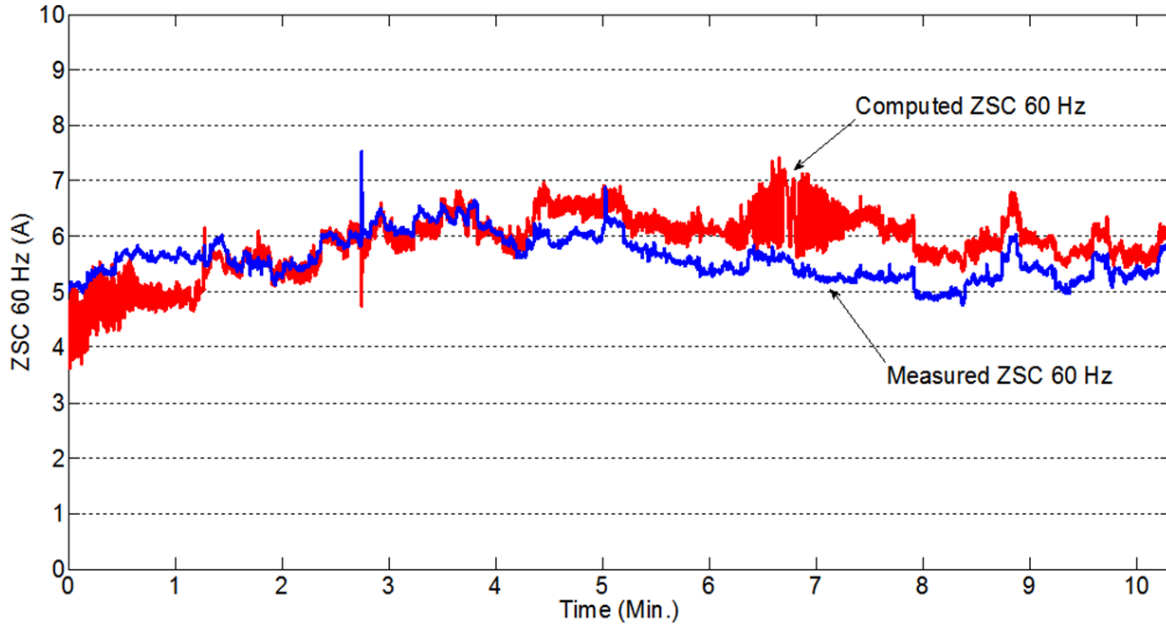


Figure 4.30: Feeder current and ZSC computation results at the second location.

The main sources of the measurement uncertainty are considered the electronic noises in the sensor-amplifier-ADC chain, and the thermal drift during the measurement. Other nature nuisances such as any nearby magnetic field interference, foreign conductive object that can cause induction (e.g. fence, pipelines) will also affect the measurement accuracy. The later uncertainty is not discussed here and might be avoided by selecting clear measurement spot.

According the statistic theory, the measurement errors are estimated and described following the Gaussian-distribution, i.e. if the electronic noises in the analog circuitry are superimposed on the signal samples with a variance σ^2 , the variances of the two variables B_{1vy} and B_{2vy} are $2\sigma^2/N_s$ (N_s is the sampling rate, in this proposed sensor array device $N_s=15.36\text{kHz}$). It is easy to understand that when the actual ZSC amplitude increase, the signal-to-noise ratio (abbreviated SNR) increases dramatically, which will reduce the measurement uncertainty. For the thermal effect in the long-time testing, since the sensor sensitivity is calibrated in lab environment at 60Hz, 25°C, the variance of the sensor sensitivity at field is mainly due to the temperature dependence.

4.7 Summary

This chapter relates to the design of a mobile sensor array and the associated deployment/computation methods with such apparatus for sensing the zero-sequence current in a set of overhead power lines. The overhead line configurations and the existence of neutral conductor will not impact the feasibility of the proposed. The deployment of the proposed apparatus is simple and immune to the installation uncertainties. The proposed sensor array measures the magnetic fields generated by these overhead line currents remotely where no direct access to the power conductors is required. These magnetic field measurements are then used to compute the zero-sequence current in real-time automatically, the results are available in either re-constructed current waveform form or the fundamental and harmonic current phasor indices.

The research proposed in this chapter has broader applications and may be advantageously employed in many other situations where access to the overhead power lines is difficult. The formulation and the implementation schemes obtained in this research are also applicable to measure another popular and important distribution system called single-wire-earth-return system.

Single wire earth return (SWER) systems are widely used worldwide in New Zealand, Australia, Brazil, India and North America for distributing electricity to rural areas. In these areas, the end customers are scattered sparsely with low population density and light load requirements [94], [95]. Typical SWER network creates a single-phase circuit by utilizing just one current carrying conductor and the earth as the current return path. This topology leads a significant cost saving compared to the commonly used three-phase and two-phase distribution systems, whatsoever the line hardware (conductor, poles, insulators, etc.) or the protection devices (fuses, re-closer, etc.) [96]. As a result, SWER systems are very attractive to utility companies in the rural distribution markets.

In spite of the economic advantages of SWER system, as the length of the single-phase conductor could extent to hundreds of kilometers in the rural area, these distribution lines are usually not effectively monitored. Sufficient information regarding the current flow on the SWER systems is hardly available [97]. In addition, the utility company's patrol team lacks effective measurement equipment to collect the necessary current information of the SWER systems. Troubleshooting a power quality issue or a high impedance fault will take long work time since it is always difficult and time-consuming to locate the problematic spot along the lines among the vast rural area [98]. Our findings have shown that the proposed technique is an elegant and effective approach to measure currents in the SWER systems. This application can be further investigated in the future research.

Chapter 5

Conclusions and Future Works

5.1 Thesis Conclusions

With the rapid development of the smart grid infrastructure, the modern power system, after more than 100 years of development, has become more advanced than ever. The increasing significance of current measurement in the modern power systems has led to the development of many innovative current-sensing approaches in the recent years. However, the existing current-sensing techniques are still far from perfect for solving the multiple conductor current measurement problems.

Measuring the currents in a group of bundled, enclosed or inaccessible conductors has been an on-going problem, but has many practical and attractive uses. Traditional current-sensing techniques are not able to measure the conductor currents without accessing every individual conductor, so their use for the multi-conductor current measurement problems is often limited in actual practice. Such constraints are commonly seen in power systems: current problems with the enclosed conductors, inaccessible conductors, and overhead power lines are well-known examples that are difficult to solve by using the traditional current-sensing techniques. The objective of this thesis was to propose solutions that would be easy to implement and adaptive to different conductor configurations.

The main conclusions and contributions of this thesis are summarized as below:

- 1) A magnetic sensor array technique with an active sensor calibration scheme for measuring currents in a group of enclosed conductors was proposed. It was designed specifically current monitoring in North American residences.

- 2) A magnetic sensor array technique for measuring the multi-conductor cable current was proposed. The currents are computed by employing a set of magnetic sensors with known positions in an open-loop sensor array configuration. The main idea for enabling such a measurement is to calibrate the sensor parameters by using an off-line sensor parameter calibration scheme. This scheme dramatically reduces the computation work load and makes deriving the currents mathematically from the measurement system model feasible.
- 3) A magnetic sensor array technique to measure the zero-sequence current in the three-phase-three-wire or three-phase-four-wire overhead power lines was proposed. It has the potential to act as a portable ZSC meter in the field to solve many power quality problems in distribution power systems.

The proposed techniques and results only begin the exploration to the multiple conductor current measurement problems. The achievements of this research are encouraging. It can be stated after years of research on this topic that the results presented in this thesis reveal only a small portion of the iceberg. More applications and their solutions for the multiple conductor current measurement challenges, utilizing the sensor array techniques, are still under investigation. The use of enhanced sensing hardware and data-processing algorithms could improve this type of research, generating more powerful tools that would benefit the electrical power industry.

5.2 Recommendations for Future Work

Future researchers could extend this thesis by carrying out the following recommendations.

- Improve the existing methods.

The accuracy and reliability of the proposed current sensor array techniques can be

potentially improved by utilizing a proper shielding structure or certain filtering schemes, either an additional hardware design or the digital data manipulations during the data-processing stage, to eliminate the effects of the outside cross-talk magnetic field.

- Improve the prototype devices.

Prototype devices to evaluate the three problems described in this thesis were built. The results from the field tests using these devices were presented in Chapter 2-4. The preliminary results demonstrated the validity of the proposed methods. Due to the complexity of the actual measurement environment, revisions to fine-tuning the device's performance may benefit the future research. Examples are the use of other types of sensors due to their measurement range and the sensitivity consideration, and the re-design of the analog signal-processing circuit due to the amplify ratio or noise elimination requirement. Additional technical specifications of the proposed devices, such as the temperature endurance with the seasonal impact and the long-term stability, need to be confirmed.

- Identify more scenarios for other conductor configurations.

In general, the conductor configurations presented in this thesis represent only a portion of the common forms of the practical multiple conductor systems. More power-transferring cables such as SWER distribution lines, the Romex cables, power distribution cables with the concentric neutral (multiple neutral strands circulating the core conductor), cables with armors, and cables with shields can be estimated in future research. The electrical power industry needs a method for measuring the cables currents non-intrusively without isolating the conductors.

There are always much interests to measure the overhead power line currents remotely. As discussed in Chapter 4, the main difficulty to apply the sensor array technique in this task is the geometric sensitivity constrain, that the sensor array is mobile and deployed on the ground level, far away from the conductors of interests. One possible solution might be using an unmanned aerial vehicle, typically a drone, equipped with the sensor array device.

It flies near the conductors and keeps still in air to allow the sensor array to compute the conductor currents in real-time. With the fast-growing modern consuming electronic technologies, more intelligent and versatile drones have emerged recently and have been proved useful in many areas [99], [100]. Many commercial drones are able to float steady at certain height and position, and can remain its horizontality long time. This is a very attractive feature for measuring the overhead line currents, safely and conveniently. It converts this current measurement problem as a special case as described in Chapter 3. We may potentially adopt similar formulation and computation scheme, with the help of the roughly known conductor and sensor positions, considering the height of the drone is known by itself and the conductor positions are estimated from the utility line models.

The measurement utilizing the sensor array technique can be difficult due to the complexity of the cable structure. We have studied only the cases where the conductors can be treated as ideal; i.e., the conductors are long and straight without EMF shielding. Successful formulations of the problems for other commonly used industrial cables will dramatically enrich the practical value of the proposed sensor array technique.

- Identify more applications for more power system parameter measurements.

This thesis focused mainly on addressing the unsolved power system current measurement problems; nevertheless, the proposed sensor array technique can be further extended for various power system parameters measurement. The power quality indices evaluation such as the IHD and the THD percentage [101], [102] or the HV transmission line harmonic measurement based on the electric field sensor array are all direct and important applications utilizing the sensor array technique. [103]-[105] present other relevant topics for possible future research.

Bibliography

- [1] S. Ziegler, R. C. Woodward, H. H. C. Iu, and L. J. Borle, “Current sensing technologies: a review,” *IEEE Sensors J.*, vol. 9, No. 4, pp. 354-376, Apr. 2009.
- [2] Q. He, C. Wei and R. S. Blum, “Effects of unsuccessful transmissions of measurements on uncertainty in power flow calculations,” *Proc. 2012 IEEE 7th Sensor array and Multichannel Signal Processing Workshop (SAM)*, pp.461-499, June 2012.
- [3] H. Kirkham, “Current measurement methods for the smart grid,” *Proc. 2009 IEEE Power & Energy Society General Meeting*, Calgary, Canada, July 26–30, 2009.
- [4] P. Zhang, F. Li and N. Bhatt, “Next-Generation Monitoring, Analysis, and Control for the Future Smart Control Center,” *IEEE Trans. Smart Grid*, vol. 1, no. 2, pp. 186-192, Sept. 2010.
- [5] F. Li, W. Qiao, H. Sun, H. Wan, J. Wang, Y. Xia, Z. Xu, and P. Zhang, “Smart transmission grid: vision and framework,” *IEEE Trans. Smart Grid*, vol. 1, no. 2, pp. 168–177, Sept. 2010.
- [6] United State Department of Energy, “The smart grid: An introduction,” August 2009. [Online]. Available: <https://energy.gov/oe/downloads/smart-grid-introduction-0>.
- [7] C. M. Johnson and P. R. Palmer. “Current measurement using compensated coaxial shunts,” *Proc. IEE Sci., Meas. Tech.*, vol. 141, no. 6, pp. 471-480, Nov 1994.
- [8] R. A. Pfuntner, “Current transformers near high-current busses,” *Electr. Eng.*, vol. 70, no. 12, pp. 1077-1077, Dec. 1951.
- [9] C. Baudart, “Device for measuring an electrical current in a conductor using a Rogowski coil,” U.S. Patent 5,442,280, Aug.15, 1995.
- [10] L. D. Radosevich and D. G. Kannenberg, “Hall effect current sensor package for sensing electrical current in an electrical conductor,” U.S. Patent 6,545,456, Apr. 8, 2003.
- [11] P. Ripka, “Review of fluxgate sensors,” *Sens. Actuators A: Physical*, 1, Vol. 33, pp.

129–141, 1992

- [12] Z. Zhang, O. Syuji, A. Osamu and K. Hideto, “Development of the Highly Precise Magnetic Current Sensor Module of ± 300 A Utilizing AMR Element With Bias-Magnet,” *IEEE Trans. Magn.*, vol. 51, no. 1, pp. 1-5, Jan. 2015.
- [13] I. Jedlicska, R. Weiss and R. Weigel, “Increasing the measurement accuracy of GMR current sensors through hysteresis modeling,” *IEEE International Symposium on Industrial Electronics*. pp. 884 – 889, June 2008-July 2008.
- [14] S. Tumanski, “Induction coil sensors-a review,” *Meas. Sci. and Technol.*, vol. 18, pp: 31–46, Jan. 2007.
- [15] L. Dalessandro, N. Karrer and J. W. Kolar, “High-Performance Planar Isolated Current Sensor for Power Electronics Applications,” *IEEE Trans on Power Elec.*, vol.22, no.5, pp.1682-1692, Sept. 2007.
- [16] Würth Elektronik eiSos GmbH & Co., “Datasheet of coil inductor 7447452154,” [Online]. Available: <http://katalog.we-online.de/pbs/datasheet/7447452154.pdf>
- [17] R. Weiss, R. Makuch, A. Itzke and R. Weigel, “Crosstalk in Circular Arrays of Magnetic Sensors for Current Measurement,” *IEEE Trans. Ind. Electron.*, vol. 64, no. 6, pp. 4903-4909, June 2017.
- [18] R. Bazzocchi and L. Di Rienzo, “Interference rejection algorithm for current measurement using magnetic sensor arrays,” *Sens. and Actuators: A. Physical*, vol. 85(1-3), pp. 38-41. 2000.
- [19] L. Di Rienzo, R. Bazzocchi and A. Manara, “Circular arrays of magnetic sensors for current measurement,” *IEEE Trans. Instrum. Meas.*, vol.50, no.5, pp.1093-1096, Oct. 2001.
- [20] K. L. Chen and N. M. Chen, “A new method for power current measurement using a coreless Hall Effect current transformer,” *IEEE Trans. Instrum. Meas.*, vol. 60, no. 1, pp. 158-169, Jan. 2011.
- [21] E. S. Leland, “A MEMS Sensor for AC Electric Current,” Ph.D. Dissertation, Univ. of California, Berkeley, California, USA, 2009.
- [22] B. Culshaw, “Optical fibre transducers,” *Radio and Electronic Engineer*, vol. 52, no.

- 6, pp. 283-290, June 1982.
- [23] K. Bohnert, P. Gabus, J. Nehring, H. Brandle and M. G. Brunzel, "Fiber-Optic Current Sensor for Electrowinning of Metals," *J. Lightw. Technol.*, vol. 25, no. 11, pp. 3602-3609, Nov. 2007.
- [24] H. Krim and M. Viberg, "Two decades of array signal processing research: the parametric approach," *IEEE Signal Processing Mag.*, vol. 13, no. 4, pp. 67-94, Jul 1996.
- [25] S. U. Pillai, *Array Signal Processing*, New York: Springer, 1989.
- [26] P. Stoica and R. Moses, *Introduction to Spectral Analysis*, Englewood Cliffs: Prentice-Hall USA, 1997.
- [27] W. Wong, T. N. Ng, S. Sambandan and M. Chabinyk, "Materials, Processing, and Testing of Flexible Image Sensor Arrays," *IEEE Design & Test of Computers*, vol. 28, no. 6, pp. 16-23, Nov.-Dec. 2011.
- [28] M. Tayyab, M. S. Sharawi and A. Al-Sarkhi, "A Radio Frequency Sensor Array for Dielectric Constant Estimation of Multiphase Oil Flow in Pipelines," *IEEE Sensors J.*, vol. 17, no. 18, pp. 5900-5907, Sept.15, 15 2017.
- [29] U. Marschner and W. J. Fischer, "Indirect Measurement of a Bar Magnet Position Using a Hall Sensor Array," *IEEE Trans. Magn.*, vol. 43, no. 6, pp. 2728-2730, June 2007.
- [30] A. la Cour-Harbo, "Geometrical modeling of a two-dimensional sensor array for determining spatial position of a passive object," *IEEE Sensors J.*, vol. 4, no. 5, pp. 627-642, Oct. 2004.
- [31] J. T. Scoville and P. I. Petersen, "A low-cost multiple Hall probe current transducer," *Review of Sci. Instrum.*, vol.62, no.3, pp.755-760, Mar 1991
- [32] E. R. Olson and R. D. Lorenz, "Effective Use of Miniature Multipoint Field-Based Current Sensors Without Magnetic Cores," *IEEE Trans. Ind. Appl.*, vol.46, no.2, pp.901-909, Mar./Apr. 2010.
- [33] El-Essawy et al., "Multi-conductor cable current and voltage sensors," U.S. Patent 2012/0 319 676 A1, Dec. 20, 2012.

- [34] X. Li, J. You, X. Shu and R. Kang, “Electric current measurement using AMR sensor array,” *Proc. International Conference on Mechatronics and Automation*, pp.4085-4089, Aug. 2009.
- [35] T. Bratland and M. J. Caruso, “A New Perspective on Magnetic Field Sensing,” *Sensors*, Dec. 1, 1998.
- [36] X. Sun, Q. Huang, Y. Hou, L. Jiang and P. W. T. Pong, “Noncontact operation-state monitoring technology based on magnetic-field sensing for overhead high-voltage transmission lines,” *IEEE Trans. Power Del.*, vol. 28, no. 4, pp. 2145–2153, Oct 2013.
- [37] Q. Huang, W. Zhen and P. W. T. Pong, “A Novel Approach for Fault Location of Overhead Transmission Line With Noncontact Magnetic-Field Measurement,” *IEEE Trans. Power Del.*, vol.27, no.3, pp.1186-1195, July 2012
- [38] X. Sun, K. S. Lui, K. K. Y. Wong, W. K. Lee, Y. Hou, Q. Huang and P.W.T. Pong, “Novel Application of Magneto-resistive Sensors for High-Voltage Transmission-Line Monitoring,” *IEEE Trans. Magn.*, vol.47, no.10, pp.2608-2611, Oct. 2011
- [39] B. Han, T. Zhang, K. Zhang, B. Yao, X. Yue, D. Huang, H. Ren and X. Tang, “Giant Magneto-impedance Current Sensor With Array-Structure Double Probes,” *IEEE Trans. Magn.*, vol.44, no.5, pp.605-608, May 2008
- [40] T. Sorensen, “Shielded current sensor,” U.S. Patent 2009/ 0 115 399, May 7, 2009.
- [41] T. Sorenson, “Current measurement device,” U.S. Patent 6 717 397 B2, Apr. 6, 2004
- [42] IEEE Standard Power Cable Ampacity Tables, *IEEE Std 835-1994* , pp.1-3151, Dec. 1994
- [43] J. M. Libove, “Apparatus for measuring voltages and currents using non-contacting sensors,” U.S. Patent 5 473 244 A, Dec. 5, 1995.
- [44] G. D'Antona, L. D. Rienzo, R. Ottoboni and A. Manara, “Processing magnetic sensor array data for AC current measurement in multi-conductor systems,” *IEEE Trans. Instrum. Meas.*, vol.50, no.5, pp.1289-1295, Oct 2001.
- [45] Z. Zhang and L. Di Rienzo, “Optimization of magnetic sensor arrays for current measurement based on swarm intelligence and D-optimality”, *COMPEL: The*

International Journal for Computation and Mathematics in Electrical and Electronic Engineering, Vol. 28 Iss: 5, pp.1179 – 1190, 2009.

- [46] A. P. Grilo, P. Gao, W. Xu and M. C. de Almeida, “Load Monitoring Using Distributed Voltage Sensors and Current Estimation Algorithms,” *IEEE Trans. Smart Grid*, vol. 5, no. 4, pp. 1920-1928, July 2014.
- [47] S. T. Mak and D. L. Reed, “TWACS, a new viable two-way automatic communication system for distribution networks Part I: Outbound communication,” *IEEE Power Eng. Review*, vol. PER-2, no. 8, pp. 65-65, Aug. 1982.
- [48] S. T. Mak and T. G. Moore, “TWACS, a new viable two-way automatic communication system for distribution networks. Part II: Inbound communication,” *IEEE Trans. Power App. Syst.*, vol. PAS-103, pp. 2141–2147, Aug. 1984.
- [49] T. Lui, W. Stirling, and H. Marcy, “Get smart,” *IEEE Power Energy Mag.*, vol. 8, no. 3, pp. 66 –78, May./Jun. 2010.
- [50] P. Wallich, “Parsing power,” *IEEE Spectrum*, vol.50, no.3, pp.23-24, Mar. 2013.
- [51] K. Basu, V. Debusschere, S. Bacha, U. Maulik and S. Bondyopadhyay, “Nonintrusive Load Monitoring: A Temporal Multilabel Classification Approach,” *IEEE Trans. Ind.l Informat.*, vol. 11, no. 1, pp. 262-270, Feb. 2015..
- [52] Z. Wang and G. Zheng, “Residential appliances identification and monitoring by a nonintrusive method,” *IEEE Trans. Smart Grid*, vol. 3, no. 1, pp. 80–92, Mar. 2012.
- [53] J. N. Sharood, “Appliance retrofit monitoring device with a memory storing an electronic signature,” U.S. Patent 6 934 862, Aug. 23, 2005.
- [54] D. Liu, “Electric adapter with display unit,” U.S. Patent 6 095 850 A, Aug. 1, 2000.
- [55] C. Laughman, K. Lee, R. Cox, S. Shaw, S. Leeb, L. Norford and P. Armstrong, “Power signature analysis,” *IEEE Power Energy Mag.*, vol.1, no.2, pp.56-63, Mar./Apr. 2003.
- [56] G. W. Hart, “Nonintrusive appliance load monitoring,” *Proc. IEEE*, vol.80, no.12, pp.1870-1891, Dec. 1992.
- [57] M. Zeifman, K. Roth, “Nonintrusive appliance load monitoring: Review and outlook,” *IEEE Trans. Consum. Electron.*, vol.57, no.1, pp.76-84, Feb. 2011.

- [58] S. Gagnon, "System and method for reading power meters," U.S. Patent 7 174 260 B2, Feb. 6, 2007.
- [59] Blue Line Innovations, "OPTICAL SENSOR," July 2014. [Online]. Available: <https://www.bluelineinnovations.com/features>.
- [60] F. Sultanem, "Using appliance signatures for monitoring residential loads at meter panel level," *IEEE Trans. Power Del.*, vol.6, no.4, pp.1380-1385, Oct. 1991.
- [61] SEQUENTRIC Smart Grid Technologies, "Smart grid gateway," July 2014 [Online]. Available: <http://sequentric.com/products/index.html>.
- [62] E. A. Rodenberg, "Programmable electricity consumption monitoring system and method," U.S. Patent 7 043 380 B2, May 9, 2006.
- [63] BrulTech, "ECM-1240 Installation Guide," July 2014 [Online]. Available: <http://www.brultech.com/software/files/getsoft/1/2#man>.
- [64] W. Xu, J. R. Acharya, R. Torquato and J. Yong, "A Method to Determine Stray Voltage Sources-Part I: Concept and Theory," *IEEE Trans Power Del.*, vol. 30, no. 2, pp. 713-719, April 2015.
- [65] R. Torquato, J. R. Acharya and W. Xu, "A Method to Determine Stray Voltage Sources—Part II: Verifications and Applications," *IEEE Trans. Power Del.*, vol. 30, no. 2, pp. 720-727, April 2015.
- [66] M. Hollander and D. A. Wolfe, *Nonparametric Statistical Method, 2nd edition*. New York: Wiley, 1999.
- [67] M. Bourkeb, C. Joubert, R. Scorretti, O. Ondel, H. Yahoui, L. Morel, L. Duvillaret, C. Kern, and G. Schmitt, "Device for measuring currents in the conductors of a sheathed cable of a polyphase network," WO Patent 2013068360 A1, May 16, 2013.
- [68] M. Bourkeb, O. Ondel, R. Scorretti, C. Joubert, L. Morel and H. Yaoui, "Improved AC current measurement approach in multiphase cable using proper orthogonal decomposition," *Eur. Phys. J. Appl.Phys.*, 64: 24509, Nov. 2013.
- [69] A. Björck, *Numerical Methods for Least Squares Problems*, SIAM, Philadelphia, USA, 1996.
- [70] P. E. Gill, W. Murray and M. H. Wright, *Practical Optimization*, Academic Press,

- London, UK, 1981.
- [71] J. Nocedal and S. J. Wright, *Numerical Optimization*, Springer, New York, USA, 1999.
- [72] B. Y. Qu, P. N. Suganthan, and J. J. Liang, "Differential evolution with neighborhood mutation for multimodal optimization," *IEEE Trans. Evol. Comp.*, vol. 16, no. 5, pp. 601-614, Oct. 2012.
- [73] L. Meng, P. Gao, M. M. Haji and W. Xu, "Magnetic Sensor Arrays-based AC Current Measurement for Multi-Conductor Cables using Evolutionary Computation Method", *IEEE Trans. Instrum. Meas.*, vol.64, no. 10, pp. 2747-2758, Oct. 2015
- [74] J. E. Gentle, *Computational Statistics*. New York: Springer, 2009.
- [75] Fluke i1000s AC Current Probe Calibration Manual. [Online]. Available: http://media.fluke.com/documents/i1000s_cmeng0000.pdf
- [76] C. L. Fortescue, "Method of Symmetrical Coordinates Applied to the Solution of Polyphase Networks," *AIEE Trans.*, vol. 37, part II, pp. 1027-1140, July 1918.
- [77] J. D. Glover, M. S. Sarma and T. J. Overbye, *Power System Analysis and Design 5th Edition*, Thomson-Engineering, Jan. 2011, pp. 471-511.
- [78] Hänninen, S. and Lehtonen, M, "Method for detection and location of very high resistive earth faults," *Euro. Trans. Electr. Power*, Vol. 9, pp. 285–291, 1999.
- [79] G. Johnson, M. Schroeder and G. Dalke, "A Review of System Grounding Methods and Zero Sequence Current Sources," *Protective Relay Engineers 61st Annual Conference*, pp. 35-71, April, 2008.
- [80] C. Christopoulos and A. Wright, *Electrical power system protection; 2nd Edition*, Kluwer Academic Publishers, Netherland, 1999, pp. 592-594.
- [81] E. Aikawa, A. Ueda, M. Watanabe, H. Takahashi and M. Imataki, "Development of new concept optical zero-sequence current/voltage transducers for distribution network," *IEEE Trans. Power Del.*, vol.6, no.1, pp. 414-420, Jan. 1991.
- [82] R. A. Fernandes and R. L. Sieron, "Transmission line sensor apparatus operable with near zero current line conditions," U.S. Patent 4 886 980 A, Dec. 12, 1989.
- [83] N. P. Tobin, "Apparatus and method for remote current sensing," U.S. Patent 6 727

- 682 B1, April. 27, 2004.
- [84] A J. Nelson, "Grounding power systems above 600V," *IEEE Ind. Applicat. Mag.*, vol. 12, no. 1, pp. 50-58, Jan.-Feb. 2006.
- [85] W. Xu, J. Marti, H. W. Dommel, "Multiphase Harmonic Load Flow Solution Technique", *IEEE Transactions Power Syst.*, Vol. 6, No. 1, 1991, p. 174-182.
- [86] Ali Abur, Antonio Gómez Expósito, *Power System State Estimation: Theory and Implementation*. CRC Press, New York, 2004
- [87] S. Chen, C. F. N. Cowan and P. M. Grant, "Orthogonal least squares learning algorithm for radial basis function networks," *IEEE Trans. Neural Networks*, vol. 2, no. 2, pp. 302-309, Mar 1991.
- [88] R. Torquato, W. Xu, W. Freitas, J. Lepka and R. Pascal, "Propagation characteristics of high-frequency harmonics in distribution systems," *Proc. IEEE Power and Energy Society General Meeting*, Boston, MA, pp. 1-5, 2016.
- [89] T. Vinh, T. L. Jones and C. H. Shih, Magnetic fields near overhead distribution lines- measurements and estimating technique, *IEEE Trans. Power Del.*, vol. 6, no. 2, pp: 912-921, Apr. 1991.
- [90] Candura instruments, "User's guide for PQPro™ Power Quality Analyzer," March 2016 [Online]. Available: http://www.candura.com/files/PQPro_Users_Guide.pdf
- [91] J. E. Lenz, "A Review of Magnetic Sensors". *Proc. of IEEE*, Vol. 78, No. 6, pp. 973-989, June 1990.
- [92] Hubbell Power Systems, "LoadLocker Ammeters," May 2015 [Online]. Available:<http://hubbellpowersystems.com/resources/ads/pdfs/LoadLocker07-001.pdf>
- [93] Entec Electric and Electronic Co., Ltd., "Wireless Current Meter," May 2015 [Online]. Available: http://entecene.en.ec21.com/Wireless_Current_Meter--2622034_349743.html
- [94] P. J. Wolfs, "Capacity improvements for rural single wire earth return systems," *Proc. the 7th international Power Engineering Conference*, pp. 1–8, Dec. 2005.
- [95] F. de La Rosa and S. T. Mak, "A look into steady state and transient performance of power lines integrating single line wire earth return circuits," *Proc. 2007 Power Eng.*

- Society General Meeting*, pp. 1-6, 2007.
- [96] A. R. Inversin, “Reducing the cost of grid extension for rural electrification,” *NRECA International Ltd. and World Bank Energy Sector Management Assistance Program*, Feb. 2000.
- [97] A. C. Westrom, A. P. S. Meliopoulos, G. J. Cokkinides and A. H. Ayoub, “Open conductor detector system,” *IEEE Trans. Power Del.*, vol.7, no.3, pp.1643-1651, Jul. 1992.
- [98] Parsons Brinckerhoff Australia Pty Ltd., “Indicative costs for replacing SWER lines,” Department of Primary Industries of Australia, August 2009 [Online]. Available: <http://www.dpi.vic.gov.au/energy/safety-and-emergencies/powerline-bushfire-safety-program/indicative-costs-replacing-swer-lines>
- [99] K. J. Wu, T. S. Gregory, J. Moore, B. Hooper, D. Lewis and Z. T. H. Tse, “Development of an indoor guidance system for unmanned aerial vehicles with power industry applications,” *IET Radar, Sonar & Navigation*, vol. 11, no. 1, pp. 212-218, 2017.
- [100] M. G. Fernández, Y. Á. López, A. Arboleya B. G. Valdés Y. R. Vaqueiro, M. E. Gómez, F. Andrés, “Antenna Diagnostics and Characterization Using Unmanned Aerial Vehicles,” *IEEE Access*, vol. 5, pp. 23563-23575, 2017.
- [101] IEEE, “IEEE Recommended Practice and Requirements for Harmonic Control in Electric Power Systems,” *IEEE Std 519-2014 (Revision of IEEE Std 519-1992)*, pp.1-29, June 2014.
- [102] D. D. Sabin, D. L. Brooks, and A. Sundaram, “Indices for assessing harmonic distortion from power quality measurements: definitions and benchmark data,” *IEEE Trans. Power Del.*, vol. 14, no. 2, pp. 489-496, Apr. 1999.
- [103] P. E. Issouribehere, D. A. Esteban, F. Issouribehere, G. A. Barbera and H. Mayer, “Perturbation measurements on HV overhead lines using Electric Field Sensors,” *IEEE Power & Energy Society General Meeting*, Vancouver, BC, 2013, pp. 1-5, 2013.
- [104] P. E. Issouribehere, D. A. Esteban, F. Issouribehere and G. A. Barbera, “Measurements of disturbances produced by power electronic devices on EHV

- overhead lines using Electric Field Sensors,” *CIGRE 2012*, Paris, France, 2012.
- [105] F. Li and P. J. Moore, “Non-contact determination of the phase sequence and voltage level of overhead conductors in air insulated substations,” *Int. J. Emerging Electr. Power Syst.*, vol. 5, no. 1, 2006.

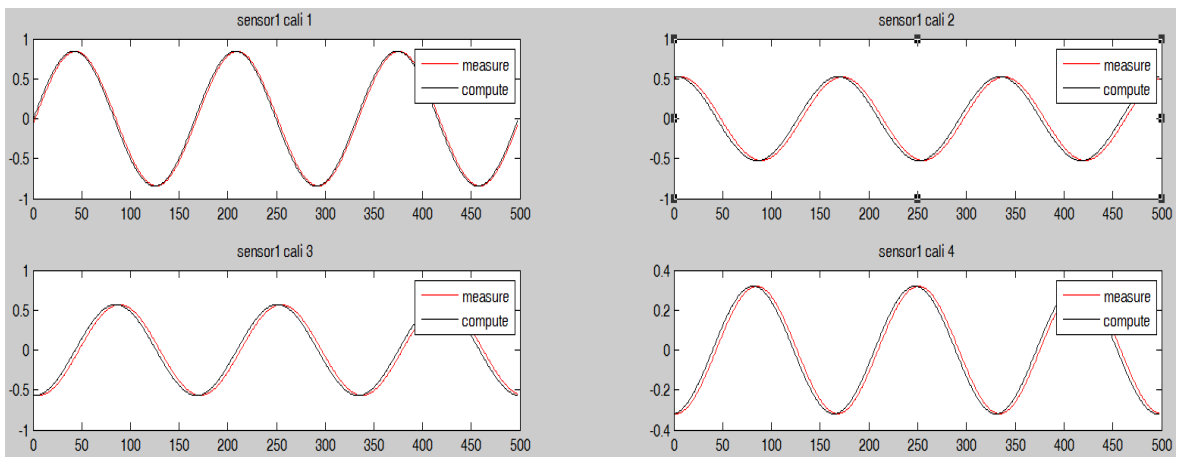
Appendix

Sensor Array Calibration Verifications

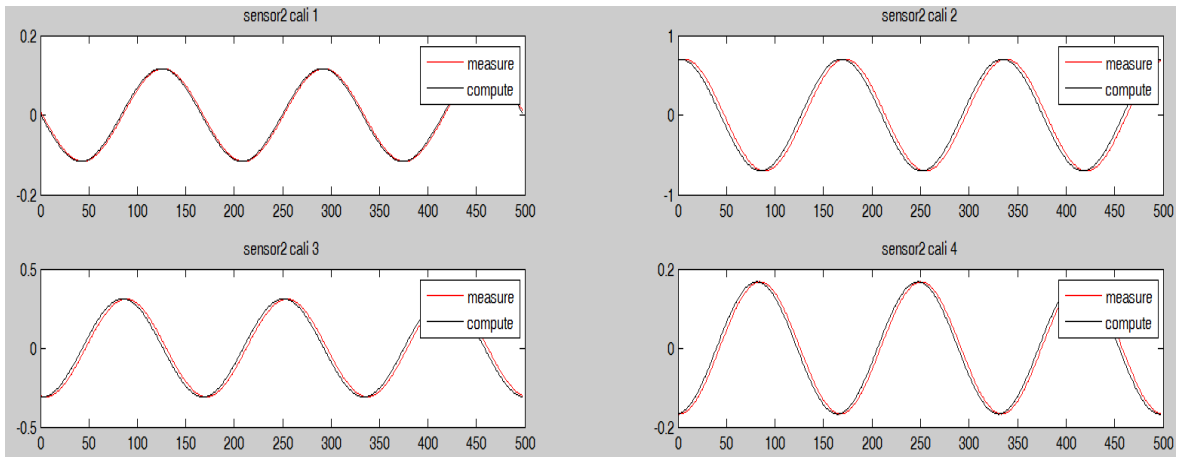
The calibration results consist of three cycles of the sensor outputs waveforms and the generated waveforms using the computed sensor information and the calibration currents. Four calibration events are plotted and the two sets of waveforms are compared to see the accuracy of the proposed sensor array calibration scheme.

The detailed results are given in Figure A.2. It can be seen that the waveform differences between the “measurement” and the “computation” are very small, meaning the converged results with good accuracy have been achieved by the proposed scheme. The sensor information is successfully found.

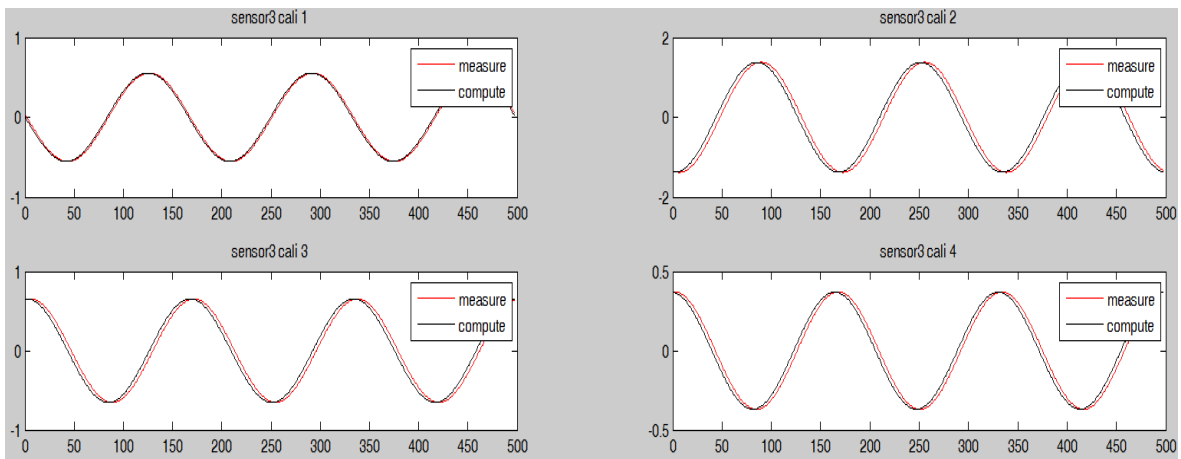
Sensor S_1 results:



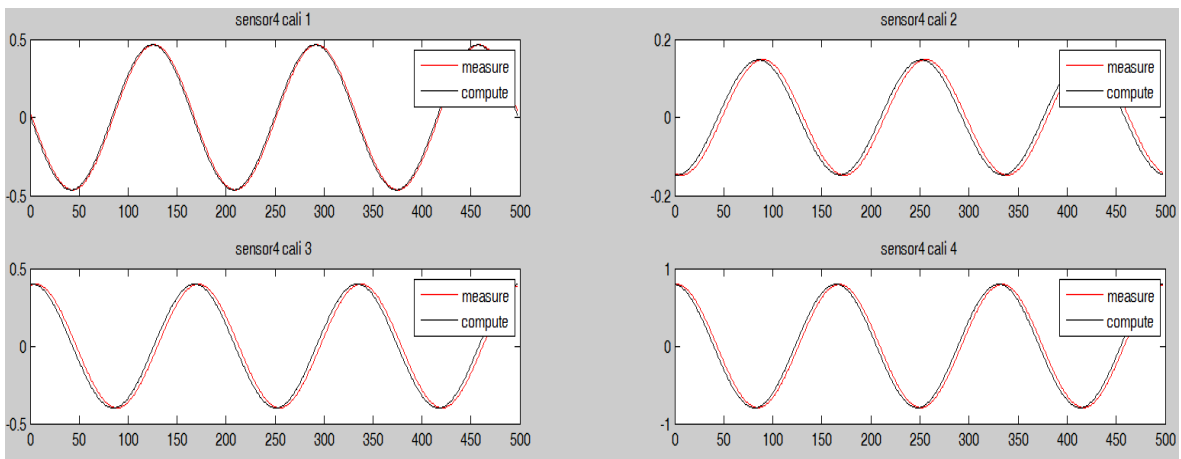
Sensor S_2 results:



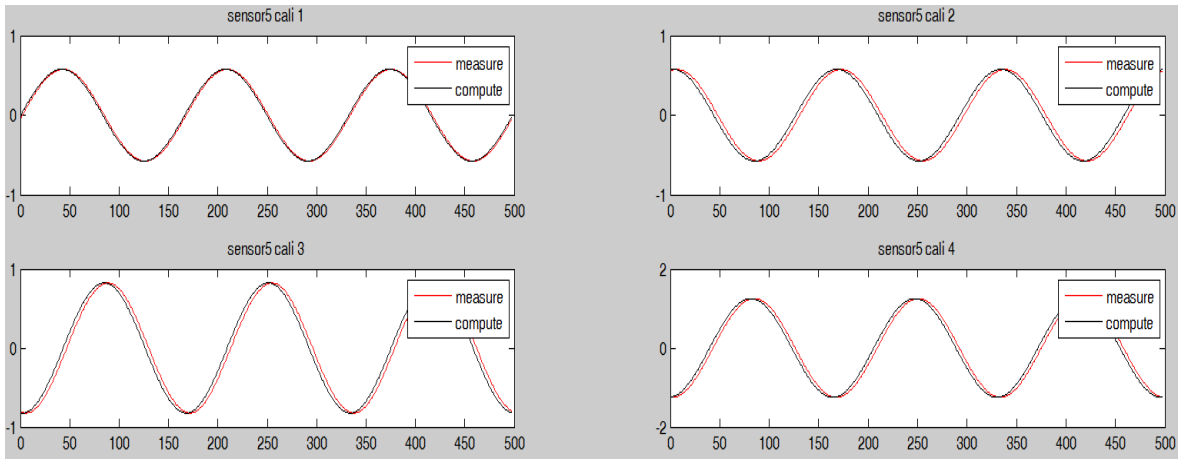
Sensor S_3 results:



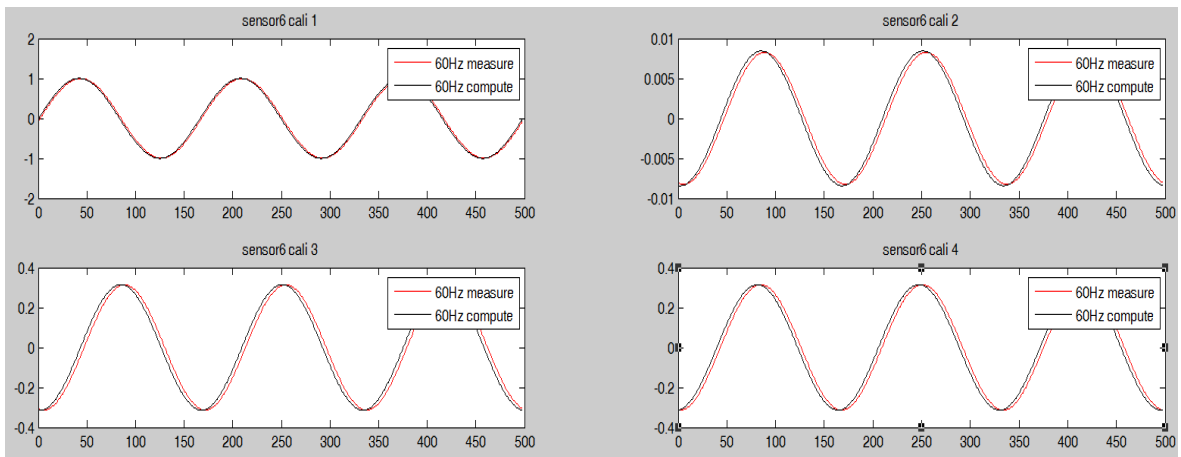
Sensor S_4 results:



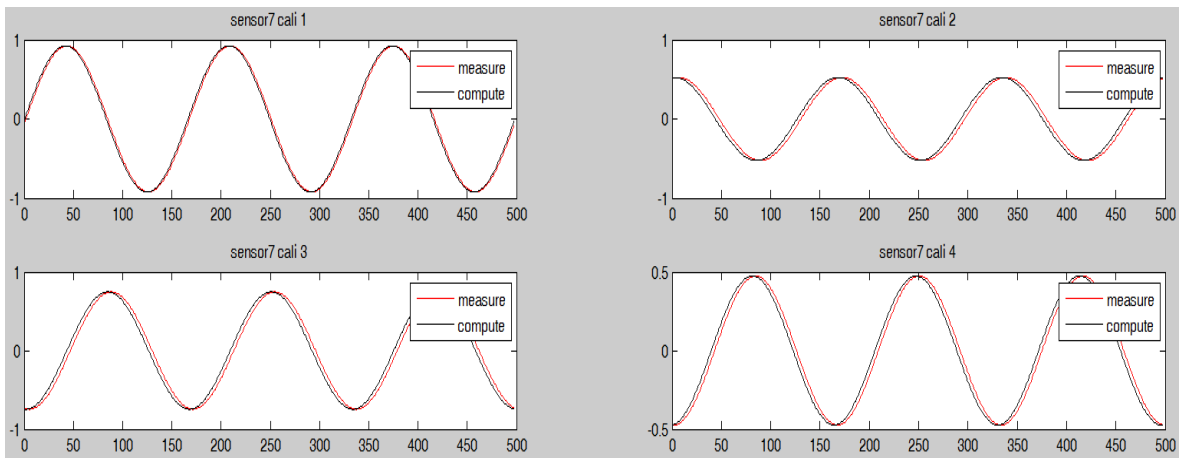
Sensor S_5 results:



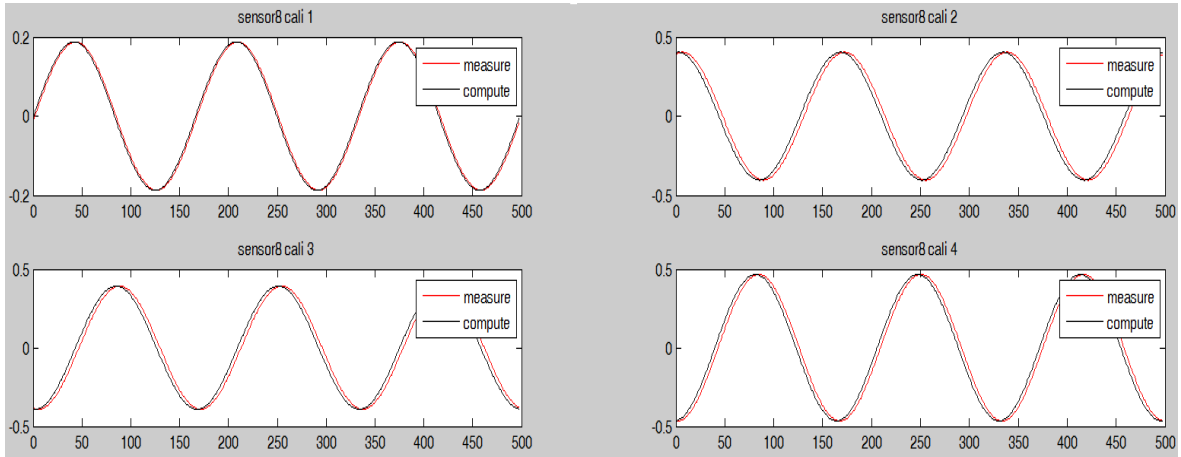
Sensor S_6 results:



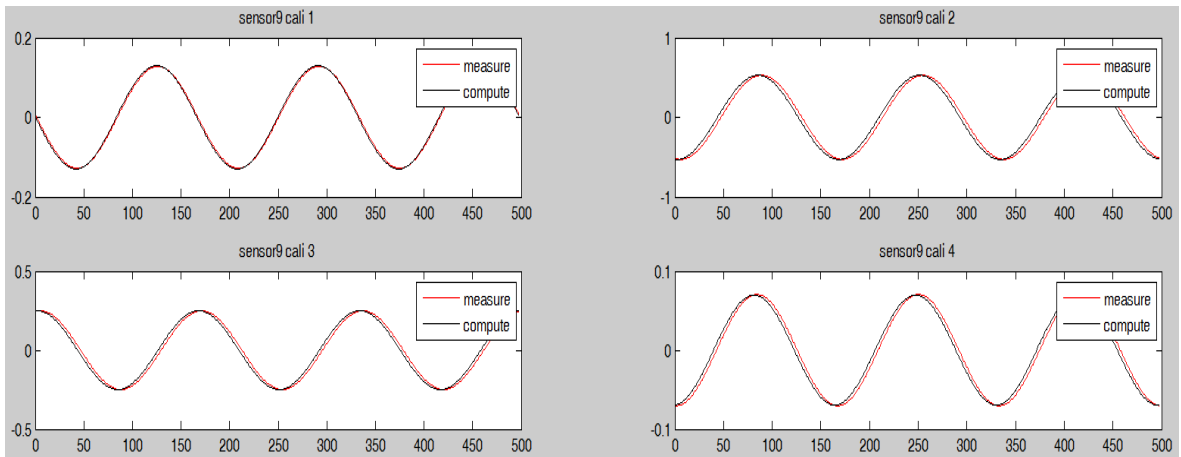
Sensor S_7 results



Sensor S_8 results:



Sensor S_9 results:



Sensor S_{10} results:

